INFORMATION TO USERS

This manuscript has been reproduced from the microfilm master. UMI films the text directly from the original or copy submitted. Thus, some thesis and dissertation copies are in typewriter face, while others may be from any type of computer printer.

The quality of this reproduction is dependent upon the quality of the copy submitted. Broken or indistinct print, colored or poor quality illustrations and photographs, print bleedthrough, substandard margins, and improper alignment can adversely affect reproduction.

In the unlikely event that the author did not send UMI a complete manuscript and there are missing pages, these will be noted. Also, if unauthorized copyright material had to be removed, a note will indicate the deletion.

Oversize materials (e.g., maps, drawings, charts) are reproduced by sectioning the original, beginning at the upper left-hand corner and continuing from left to right in equal sections with small overlaps. Each original is also photographed in one exposure and is included in reduced form at the back of the book.

Photographs included in the original manuscript have been reproduced xerographically in this copy. Higher quality 6" x 9" black and white photographic prints are available for any photographs or illustrations appearing in this copy for an additional charge. Contact UMI directly to order.

UMI

A Bell & Howell Information Company
300 North Zeeb Road, Ann Arbor MI 48106-1346 USA
313/761-4700 800/521-0600

Reproduced with permission of the copyright owner. Further reproduction prohibited without permission.

Reproduced with permission of the copyright owner. Further reproduction prohibited without permission.

A

Part I: Design and construction the step-scan Fourier transform vibrational circular dichroism

Part II: The conformation of small peptides in aqueous solution.

By

ALI KOCAK

A dissertation submitted to the Graduate Faculty in Chemistry in partial fulfillment of the requirements for the degree of Doctor of Philosophy, The City University of New York.

1998

Reproduced with permission of the copyright owner. Further reproduction prohibited without permission.

UMI Number: 9820548

Copyright 1998 by
Kocak, Ali

All rights reserved.

UMI Microform 9820548
Copyright 1998, by UMI Company. All rights reserved.

This microform edition is protected against unauthorized
copying under Title 17, United States Code.

UMI
300 North Zeeb Road
Ann Arbor, MI 48103

Reproduced with permission of the copyright owner. Further reproduction prohibited without permission.

© 1998

Ali Kocak

All Rights Reserved

Reproduced with permission of the copyright owner. Further reproduction prohibited without permission.

This manuscript has been read and accepted for the Graduate Faculty in Chemistry in satisfaction of the dissertation requirement for the degree of Doctor of Philosophy.

Dec 16, 1997
Date

Chair of Examining Committee

Jan. 13, 1998
Date

Executive Officer

Supervisory Committee

The City University of New York

Reproduced with permission of the copyright owner. Further reproduction prohibited without permission.

Abstract

Part I: The Design and Construction of the step-scan Fourier transform vibrational circular dichroism
Part II: the conformation of small peptides in aqueous solution

By
Ali Kocak

Adviser: Professor Max Diem

This dissertation consists of two parts: First part reports the design and construction of state -of-the-art interferometric instrument, "Fourier transform step-scan vibrational circular dichroism" for the observation of infrared (vibrational) circular dichroism (VCD), its optimization, as well as its performance. A discussion and compression of results between the fast -scan and step-scan interferometers describe the advantages of the step-scan

Reproduced with permission of the copyright owner. Further reproduction prohibited without permission.

interferometers in dynamic spectroscopy, where the lock-in amplifier need to subtract a very small signals.

The second part of this dissertation is the application of the vibrational circular dichroism to study the structure of small peptides in aqueous solution. The studies of the effect of the temperature and the ionic strength on the structure of small peptides using VCD, demonstrate application of VCD in attacking the difficult yet important problems in the structure of small biological molecules in aqueous solution. This sensitivity towards the conformational changes in a very short time scale (vibrational time scale), makes the VCD if not the most important, a complementary technique to other techniques available to study the conformation of biological molecules.

Reproduced with permission of the copyright owner. Further reproduction prohibited without permission.

Preface

Vibrational optical activity (VOA) is a collective term applied to two new spectroscopic techniques discovered during the early 1970's. The two techniques that had been forecast much earlier, are extensions of electronic optical activity into the spectral region of vibrational transition. Conceptually, the more straightforward of the two experiments in VOA is that the infrared circular dichroism, or vibrational circular dichroism (VCD) as it was referred to by early investigators in the area. In VCD, the differential absorption of left and right circularly polarized infrared radiation by vibrational transition of a chiral molecule is observed. The apparatus for this measurement, therefore, is similar to ultraviolet/visible circular dichrographs.

The extension of the measurements of circular dichroism into the infrared region has been a long sought goal for many scientists. It

Reproduced with permission of the copyright owner. Further reproduction prohibited without permission.

would utilize the combination of the sensitivity of CD and the specificity of infrared spectroscopy to solve a variety of problems in molecular spectroscopy, especially for biological molecules. Yet, technical obstacles made the goal impractical until the early Nineteen Seventies. Since then, many dispersive vibrational circular dichroism instruments constructed in the laboratories.

Researchers in the field have tried to take the advantages of the Fourier transform spectroscopy and build FTVCD instruments. The early attempt was to use a rapid - scan interferometry, this in effect created some technical problems, which prevented them to obtain results as good as dispersive once.

Recently, the promising results from the step- scan interferometers in the dynamic spectroscopy made the spectroscopists in the field of VCD to build their FTVCD instrument based on the step-scan interferometers.

The aim of the research project in this dissertation has evolved from the design and instrumentation of step-scan FT VCD to study stereochemical systems, specifically, conformation of biologically significant molecules. The detection and analysis in biomolecular spectroscopy have been challenging due to some inherent difficulties,

Reproduced with permission of the copyright owner. Further reproduction prohibited without permission.

such as small quantity (thus, low concentration) available. Also, its capability of determining the structure of small biological molecules in aqueous solutions, which has been the major problem in other spectroscopic techniques, such as NMR, made the VCD technique one of the fascinating probes to study the conformation of small peptides in aqueous solutions.

The major task of the research project includes two assignments: first, design and building the state - of - the - art FT-VCD instrument; second studying the structure of small peptides, namely $(Ala)_n$ where n=3,4,5,6, and the effect of the ionic strength and the temperature on the structure of these peptides using VCD instrument.

The scope of this thesis incorporates four chapters. Chapter one briefly reviews theoretical foundations of the Fourier transform spectroscopy and the differences between different types of interferometers and the modulation techniques used to modulate the infrared light. In chapter two, the focus is on the theory of the fast Fourier transform, the evolving steps from the Fourier integral discrete Fourier transform matrices and the detail description of the fast Fourier transform as well as the apodization functions and phase

Reproduced with permission of the copyright owner. Further reproduction prohibited without permission.

correction. Chapter three deals exclusively with the design of the step-scan FT-VCD unit. The extensive discussion covers optical design, the problems of noise and the ways to approach them in order to reduce their effect, electronic layout as well as its optimization. Chapter four presents data on the VCD spectra of tri, tetera, penta, hexa alanine in aqueous solution, and the determination of the conformation of these molecules. Also the effect of the ionic strength and the temperature on these peptides is presented in this chapter.

Reproduced with permission of the copyright owner. Further reproduction prohibited without permission.

To my father and mother,

my brothers and sisters

Reproduced with permission of the copyright owner. Further reproduction prohibited without permission.

Acknowledgment

I would like to thank my mentor, Dr. Max Diem who introduced me to the world of vibrational spectroscopy and the world of FTIR instrumentation. I also would like to thank my colleagues, Mr. Waldemar Cieniewicz, who has been of tremendous help; Dr. Ismailu Agbaje, Shari Syokett, Susie Boydston-White and the numerous other people, who have helped me, to many to list.

I wish to express my deepest gratitude to Dr. Rasih Demirci, the former Dean of the faculty of Science and Arts of Gazi University in Turkey, who was the guide for me to continue my studies in United States. Also, would like to express my deepest respect to Dr. Guler Somer, my former mentor in Turkey.

Finally, I would like to thank Turkish government and Chemistry department of Hunter College for the financial support during my studies.

Reproduced with permission of the copyright owner. Further reproduction prohibited without permission.

Table of Contents

Reproduced with permission of the copyright owner. Further reproduction prohibited without permission.

Reproduced with permission of the copyright owner. Further reproduction prohibited without permission.

Reproduced with permission of the copyright owner. Further reproduction prohibited without permission.

Reproduced with permission of the copyright owner. Further reproduction prohibited without permission.

Reproduced with permission of the copyright owner. Further reproduction prohibited without permission.

List of Tables

Reproduced with permission of the copyright owner. Further reproduction prohibited without permission.

Reproduced with permission of the copyright owner. Further reproduction prohibited without permission.

List of Figures

Reproduced with permission of the copyright owner. Further reproduction prohibited without permission.

Reproduced with permission of the copyright owner. Further reproduction prohibited without permission.

Reproduced with permission of the copyright owner. Further reproduction prohibited without permission.

Reproduced with permission of the copyright owner. Further reproduction prohibited without permission.

Chapter one

Introduction to Fourier transform spectroscopy

1.1 - Fourier transform spectrometry:

In Fourier transform spectrometry, the desired spectrum, the power distribution of the detected radiation as a function of frequency (or wavenumber), is obtained by Fourier transformation of the variable part of the record of power versus phase delay. We call the total record the interference function and the variable part of it the interferogram. The spectrum is, therefore, the Fourier transform of the interferogram. That there is an explicit dependence of the interferogram on the spectrum may be seen from the following discussion. From the schematic interferometer shown in Figure 1-1, the partial beam that has traversed the path XP_1Y to the detector has traveled a distance that is greater than that traveled by the other beam along XP_2Y

Reproduced with permission of the copyright owner. Further reproduction prohibited without permission.

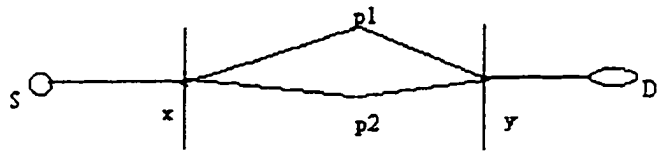

Figure 1-1: *The difference in light path*

by an amount x ($0 \leq x < \infty$) which we call the path difference or retardation, (δ). By assuming the interferometer to be otherwise symmetrical, the optical and geometrical path differences are identical (see below). Because of the path difference δ, the two beams arrive at the detector with a phase delay $2\pi\nu\delta$ for any component with frequency ν and show interference which is governed by this delay. The power at the detector is [1,2],

$$I(\delta) = B(\nu)\, d\nu + B(\nu) \cos 2\pi\nu\delta\, d\nu \qquad (1\text{-}1)$$

Reproduced with permission of the copyright owner. Further reproduction prohibited without permission.

for each spectral component of power $B(\nu)\, d\nu$ in the interval ν to $\nu + d\nu$. We assume the contribution from each path SP_1D and SP_2D to be the same, $1/2\, B(\nu)\, d\nu$ [1].

When the source is strictly monochromatic and of wavenumber ν_o, the power from each partial beam is ρ_o :

$$I(\delta) = \rho_o \ (1+\cos 2\pi\nu_o\delta)$$

$$= 2\, \rho_o \cos^2 \pi\nu_o\delta \qquad (1\text{-}2)$$

which is the interference function. It has the form of cosine fringes which extended to infinite values of retardation δ without change in amplitude, Figure 1-2. If a monochromatic source with a finite, but small, width $\Delta\nu$ is incident on the interferometer, the fringes are still basically cosinusoidal of period ν_o^{-1}; the interference between components from either side of the feature is now constructive at $\delta=0$, but becomes increasingly destructive as δ increases. This has the effect of modulating the fringes whose I_{max} falls to zero at about $\delta=\Delta\nu^{-1}$ [1,2].

When the source has a broad band width, such as is required for most spectroscopic measurements, all components are in phase at $\delta=0$ which is the zero path difference or the centerburst, but the

Reproduced with permission of the copyright owner. Further reproduction prohibited without permission.

detected intensity fluctuates rapidly to zero as δ is increased [1]. The detected power is given by adding all the components represented by equation 1-1:

$$I(\delta) = \int_0^\infty B(\nu)\, d\nu + \int_0^\infty B(\nu) \cos 2\pi\delta\nu \, d\nu \qquad (1\text{-}3)$$

Because

$$I(0) = 2 \int_0^\infty B(\nu)\, d\nu$$

at δ=0, we may write

$$I(\delta) = 1/2\ I(0) + \int_0^\infty B(\nu) \cos 2\pi\nu\delta d\nu \qquad (1\text{-}4)$$

for the interference function, noting that it consists of a D.C. component and a variable part I(δ) - I =F(δ), which is an A.C. component. We call this variable part the interferogram and rewrite equation 1-4 as

$$F(\delta) = \frac{1}{\sqrt{2\pi}} \int_0^\infty B(\nu) \cos 2\pi\nu\delta d\nu \qquad (1\text{-}5)$$

which shows that the interferogram depends on the spectrum according to a cosine Fourier integral. Using the inversion

Reproduced with permission of the copyright owner. Further reproduction prohibited without permission.

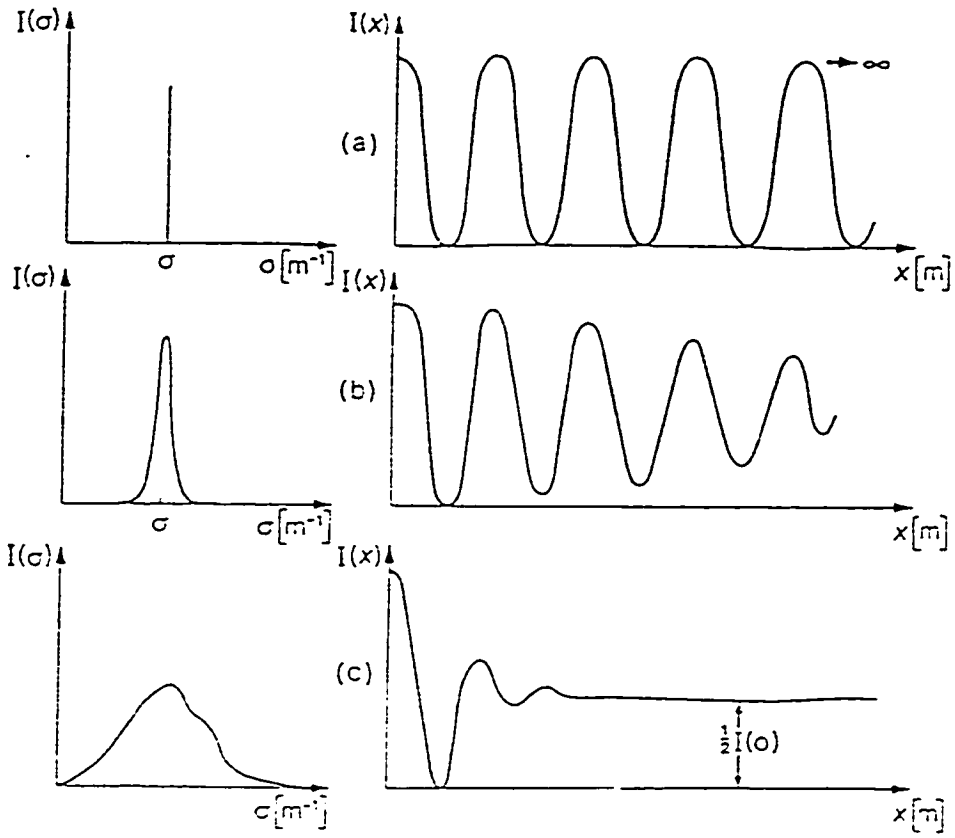

Figure 1-2 *: Relation between the detected spectrum I(σ) and the interference signal I(δ) produced by (a) monochromatic spectrum; (b) quasi-monochromatic spectrum; (c) broad - band spectrum. X[m] denotes a path differences; σ[m⁻¹]a spectral distribution. Adapted from ref. [2].*

Reproduced with permission of the copyright owner. Further reproduction prohibited without permission.

theorem [3,4] applicable to such integrals, this relation may be written as

$$B(\nu) = 4 \int_0^\infty F(\delta) \cos 2\pi\nu\delta \, d\nu \qquad (1\text{-}6)$$

Equation 1-6 shows how the spectrum may be calculated by the operation of Fourier transformation from the measured interferogram $F(\delta)$. This relation is the basis of Fourier transform spectroscopy [chapter 2].

The first interferometer to be applied to any form of spectral analysis was the two - beam instrument that Michelson invented in 1882 and which now bears his name [1,2,5]. The phase delay between the two beams, shown in Figure 1-1, is achieved in practice by dividing the incident radiation beam, as shown in Figure 1-3, with a beamsplitter and then reflecting the two component partial beams from the plane mirrors M and F back to the beamsplitter where they recombine and proceed to the detector. The angle of incidence at the beam splitter of the rays from the source is usually 45^0 and the mirrors M and F are mutually perpendicular as shown.

Reproduced with permission of the copyright owner. Further reproduction prohibited without permission.

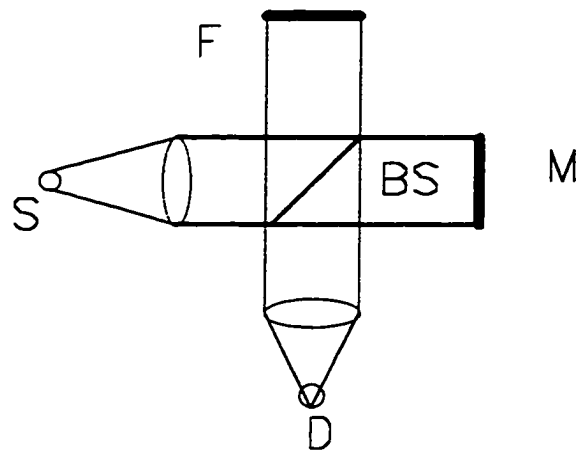

Figure 1-3: *Michelson interferometer.*

S*: The source,* ***D****: the detector,* ***BS****: beamsplitter,* ***F****: fixed mirror,* ***M****: moving mirror.*

Reproduced with permission of the copyright owner. Further reproduction prohibited without permission.

The optical path difference between the beams traveling to the fixed and movable mirrors is 2(BM - BF), see Figure 1-3. This optical path difference is the retardation, δ. When the fixed and movable mirrors are equidistant from the beamsplitter (zero retardation), the two beams are perfectly in phase on recombination at the beamsplitter, Figure 1-4. At this point, the beams interfere constructively, and the intensity of the beam passing to the detector is the sum of the intensities of the beams passing to the fixed and movable mirrors. Therefore, half of the light from the source reaches the detector at this point and the other half returns to the source.

Michelson interferometers may be used in various arrangements differing in the way the moveable mirror is moved. These arrangements are referred to as slow - scanning, rapid - scanning and step - scanning interferometers [1,2,6,7].

In slow and rapid - scanning interferometers the moving mirror moves continuously, to create a modulating frequency f (Fourier frequency) given by:

$$f = 2 \upsilon \tilde{\nu} \qquad (1\text{-}7)$$

Reproduced with permission of the copyright owner. Further reproduction prohibited without permission.

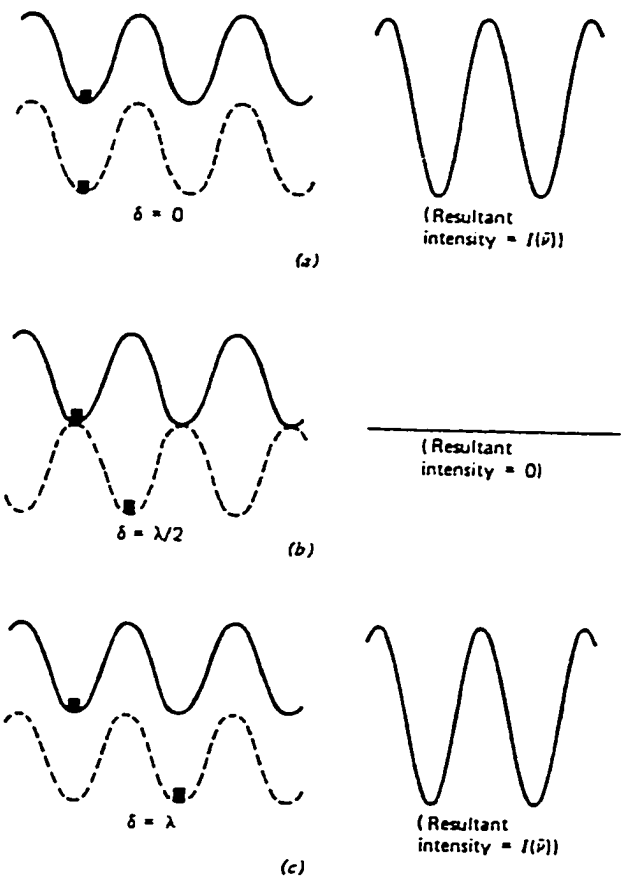

Figure 1-4: *Schematic representation of the electromagnetic waves from the fixed mirror (solid line) and movable mirror (broken line) at different values of the optical retardation.*

Reproduced with permission of the copyright owner. Further reproduction prohibited without permission.

This frequency depends on the velocity of the moving mirror υ and the wavenumber, $\bar{\nu}$, of the radiation. In slow scanning interferometers, the mirror is moved at velocities of fraction of millimeter per second creating Fourier frequency of about 1 Hz. In rapid scanning interferometers υ is in the order of a few centimeters per second, creating Fourier frequency in the range of audio frequencies (3-5kHz).

In all modern interferometers, a He-Ne laser is used as a reference to control the velocity of the mirror and data acquisition as described below. The He-Ne laser beam, passing through the optics of the interferometer is detected by a photodiode. The output voltage of this photodiode is a single frequency sinusoidal interferogram as the optical path difference varies, Figure 1-5.

$$V = \frac{V_0[1+\cos\{2\pi\delta\bar{\nu}_l\}}{2} \qquad (1\text{-}8)$$

where $\bar{\nu}_l$ is the laser wavenumber (15,803 cm^{-1}) [6]. If this signal V is AC coupled, The D.C. term ($V_0/2$) disappears. Thus, the condition V=0 may be used to trigger data acquisition in slow and rapid scan interferometers. The condition V=0 occurs when

Reproduced with permission of the copyright owner. Further reproduction prohibited without permission.

the cosine term is zero, that is, at $\delta = n/\tilde{\nu}_l$ or $n/2\tilde{\nu}_l$ that is, at every half wavelength of the He-Ne laser interferogram.

In step scanning interferometers the mirror moves incrementally in steps, and is held stationary during data collection at $\delta = n/\tilde{\nu}_l$ or $n/2\tilde{\nu}_l$. Thus, in step-scanning interferometers the He-Ne laser will be used to control the position of the mirror instead of its velocity as in case of rapid and slow scan modes. The data collected at the detector will not be at a Fourier frequency, but will be a DC signal. Since accurate D.C. measurements are much harder to carry out than A.C. measurements (due to the signal offsets and drifts), it is advantageous to introduce a modulation in order to convert the D.C. signal to an A.C. signal [8]. Different modulation techniques are used for this purpose: These techniques will be described in detail in the following section.

Reproduced with permission of the copyright owner. Further reproduction prohibited without permission.

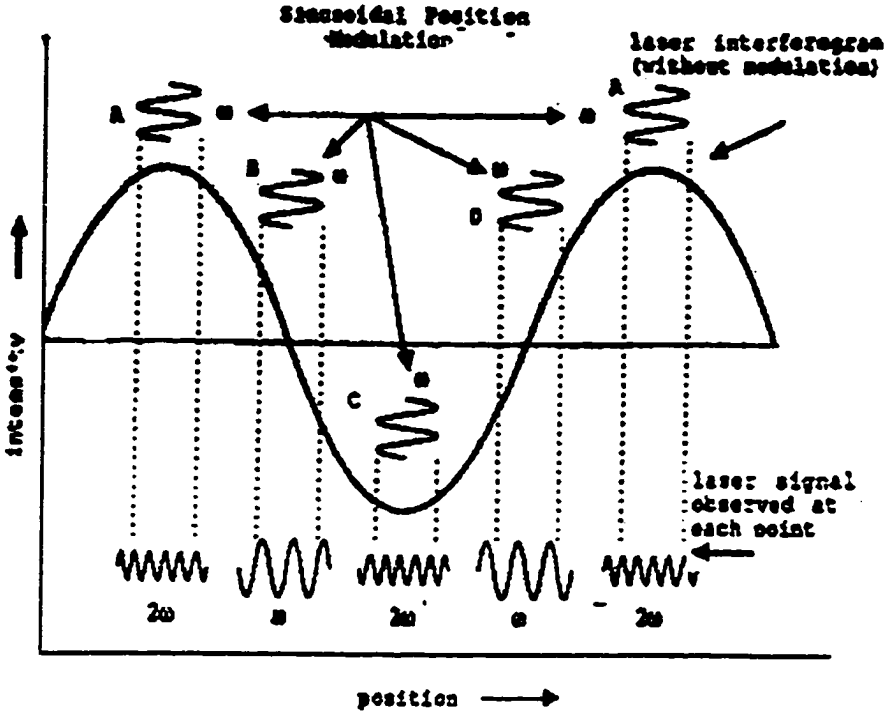

Figure 1-5: Schematic of the reference laser interferogram showing the effects of phase modulation at different retardation points. Adapted from ref. [6]

Reproduced with permission of the copyright owner. Further reproduction prohibited without permission.

1.2- Modulation of the radiant flux in an interferometer:

In step-scanning mode it is advantageous to employ some form of modulation of the radiation so that the signal at the detectors may be measured via A.C. techniques. There are two ways in which an electromagnetic wave my be modulated: by amplitude, or phase modulation techniques [1,2,7]. Amplitude modulation (AM) is used commonly in conventional infrared spectroscopy [2]. In this technique, an opaque chopper interrupts the beam regularly. The output of the detector then mirrors the imposed fluctuations. Since the regular wave form may be decomposed into the frequency components which make up its representation in terms of a Fourier series, the steady D.C. radiation intensity has been transformed into a set of alternating A.C. components, each of whose amplitudes is a measure of the original radiant intensity. A sharply tuned narrow - band amplifier, or a phase sensitive detector, is used to amplify a single frequency component, while all other frequencies are strongly attenuated. There is, therefore, a considerable gain in signal - to -

Reproduced with permission of the copyright owner. Further reproduction prohibited without permission.

noise ratio, but at the usual price of loss of speed of response. If the pass band of the amplifier has width Δf, then the response time of the amplifier is of the order $(\Delta f)^{-1}$ [2].

Another method of modulating the radiation in step-scanning interferometer is phase modulation Figure 1-5 [1,2,6,7]. The radiation traversing a Michelson interferometer may be phase modulated if one of the mirrors (usually the "fixed" one) is oscillated (or 'jittered') rapidly back and forth while maintaining its surface perpendicular to the optical axis. The origin of the modulation is shown in Figure 1-6. When the path difference corresponds to a bright or dark fringe of the monochromatic radiation, the oscillation causes little or no change in the intensity at the detector and there will be no A.C. output. When, however, the path difference corresponds to a point where the intensity is crossing the average value line, there will be a maximum A.C. signal. A cosine intensity wave is therefore translated into a sine voltage wave [2,6,7]. The argument is readily extended to the broad-band case and one arrives at the general conclusion that a

Reproduced with permission of the copyright owner. Further reproduction prohibited without permission.

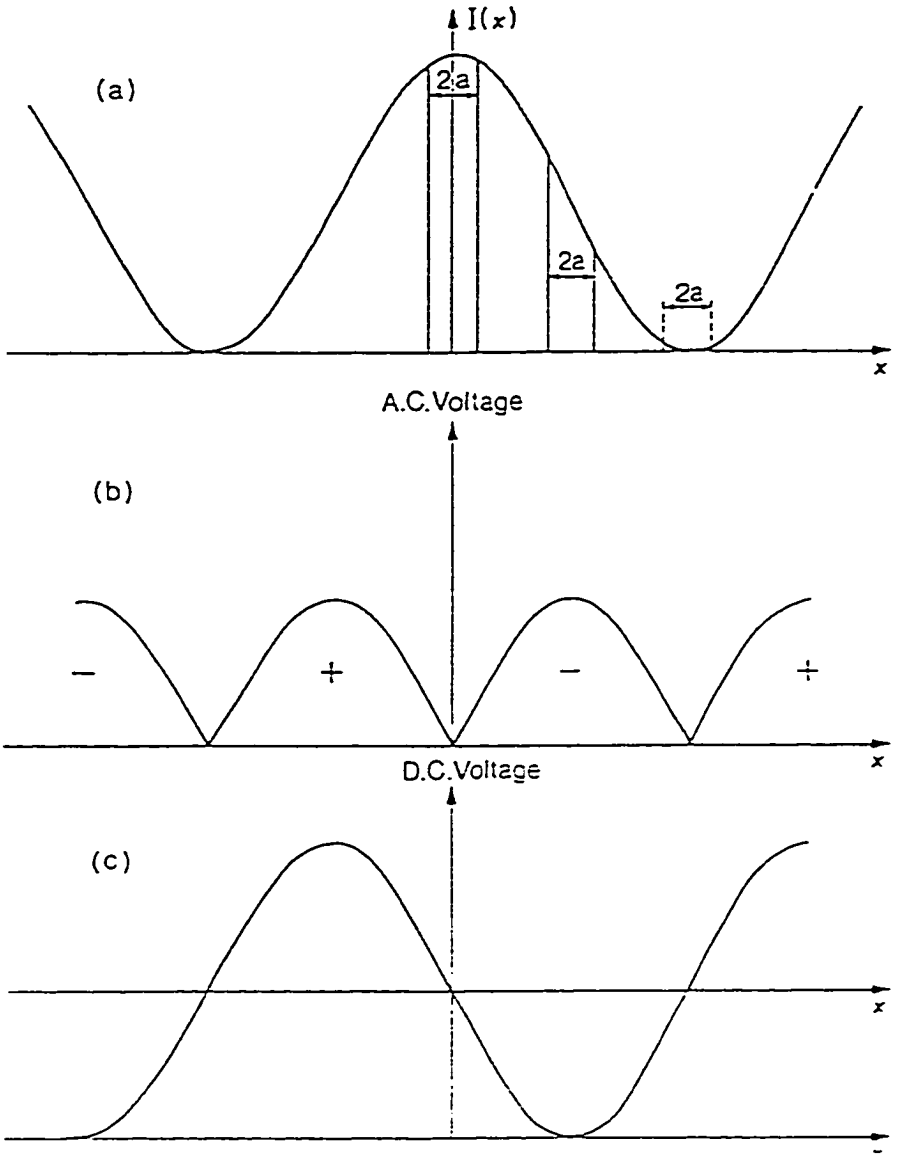

Figure 1-6: *Mechanism of phase modulation. The variation of intensity (a) are converted into a varying a.c. voltage by the oscillation of the mirror.*
2a is the amplitude of the oscillating signal. Adapted from ref. [2]

Reproduced with permission of the copyright owner. Further reproduction prohibited without permission.

PM interferogram looks very like the first derivative of the corresponding AM interferogram [1]. Some advantages of PM emerge from this simple physical visualization of its operation. First, since there is no interruption of the beam by a chopper, the average power reaching the detector is doubled. Second, the average value of the interferogram ordinates is zero and there is no need to use up a large amount of the dynamic range of the digital system with non-interferometrically coded (and therefore useless) information: this waste is especially serious when dealing with dispersive interferograms of low quality. Third, and for the same reason, the noise carried on the background - due for example to source flicker - is eliminated. Thus PM gives a considerable improvement in signal -to- noise ration and at the same time makes better use of the digital system.

Reproduced with permission of the copyright owner. Further reproduction prohibited without permission.

1.3- Mathematical theory of phase modulation

Different modulation functions can be used for the phase modulation, however the most practical one is to use a cosinusoidal function where the mirror moves according to the relation

$$x = x_0 + a \cos 2\pi f t \qquad (1\text{-}9)$$

where a is the amplitude of the phase modulation, and f is the dither frequency.

If the interferometer is being irradiated with monochromatic radiation, then the detector signal, at a fixed path difference x, is

$$V(x) = V_0 [1 + \cos 2\pi\nu x]. \qquad (1\text{-}10)$$

The dithering of the modulating mirror makes x time-dependent, according to the relation

$$V(t) = V_0 (1 + \cos 2\pi\nu[x_0 + a \cos 2\pi f t]) \qquad (1\text{-}11)$$

The Fourier transform of cos (cos ωt) function will involve Bessel functions [3,4] and we therefore expect the Fourier components of V(t) to be expressible in terms of the low order Bessel functions $J_n(f)$, where n is integer. Expanding equation 1-11 we get

Reproduced with permission of the copyright owner. Further reproduction prohibited without permission.

$$V(t)=V_0(1+\cos 2\pi\nu x \bullet \cos(2\pi\nu a \bullet \cos 2\pi f t) - \sin 2\pi\nu x \bullet \sin(2\pi\nu a \bullet \cos 2\pi f t) \quad (1\text{-}12)$$

We now use the identities

$$\cos(k \cos 2\pi\nu t) = J_0(k) - 2J_2(k) \bullet \cos 4\pi\nu t + 2J_4(k) \bullet \cos 8\pi\nu t - \text{..etc.}, \quad (1\text{-}13a)$$

$$\sin(k \cos 2\pi\nu t) = 2J_1(k) \bullet \cos 2\pi\nu t - 2J_3(k) \bullet \cos 6\pi\nu t + \text{..etc} \quad (1\text{-}13b)$$

where $J_n(k)$ are the n^{th} order Bessel functions in variable k, to calculate the powers in the various Fourier components. If the band pass of the detector plus amplifier is such as to admit only the fundamental, then the interferogram will be given by

$$V_0[2J_1(2\pi\nu a)]\sin 2\pi\nu x. \quad (1\text{-}14)$$

The modulation of a cosine function (in this case the interferogram) by another cosine function (the modulation of the mirror) generates Bessel coefficients, equation 1-13. Since only the lowest order coefficient is detected, the energy is lost in the higher order coefficients. Therefore the efficiency of PM measurements relative to AM measurements falls off at the extremes of the spectral range being measured [2].

Reproduced with permission of the copyright owner. Further reproduction prohibited without permission.

The amplitude of the jitter is increased until the greatest signal at the detector is developed. The amplitude should be approximately one - quarter of the central wavelength in the spectral range being measured.

This is usually done by measuring the output signal of the He-Ne laser detector using an oscilloscope. The amplitude should be ½ wavelength of the He-Ne laser [6,7].

Reproduced with permission of the copyright owner. Further reproduction prohibited without permission.

References

1. P. R. Griffiths and J. A. de Haseth (1986) " *Fourier transform infrared spectroscopy*", John Wiley & Sons Inc., New York.

2. J. Chamberlain (1979), *"The Principles of interferometric spectroscopy"*, John Wiley & Sons Inc., New York.

3. Erwin Kreyszing (1967) *"Advanced Engineering mathematics"* John Wiley & Sons, Inc., New York.

4. C. Ray Wylie, L. C. Barrett (1995) " *Advanced Engineering Mathematics*", McGraw-Hill, Inc., New York.

5. R.W. Ditchburn (1961), *Light*, Dover publications, Inc., New York

6. M. J. Smith, C. J. Manning, R. A. Palmer and J. L. Chao (1988), *Appl. Spectrosc.* 42, 546.

7. R. A. Palmer (1993) *Spectroscopy*, 8, 26.

8. M. L. Meade (1983) " *Lock-in amplifiers: Principles and applications*" Short Run Press Ltd., Exeter, London.

Reproduced with permission of the copyright owner. Further reproduction prohibited without permission.

Chapter two

THEORY OF THE FAST FOURIER TRANSFORM

2.1- Introduction

Fourier transform methods at first seem strange to our intuition, because we are prejudiced by our eyes to analyze our surroundings in the frequency domain-we judge light by its color and sound by its pitch. It is, however, equally useful to analyze observations in the time domain or other domains. Figure 2-1a shows two equivalent ways of representing a single-frequency sine wave signal (such as electric field amplitude of monochromatic coherent radiation), using either time domain or frequency domain display, respectively. Figure 2-1b shows a somewhat more complicated signal consisting of the sum of two sine wave oscillations of different amplitudes and different frequencies; again, it is possible to represent the signal using either time or frequency domain display. In fact, it is possible to represent virtually any periodic time domain signal in terms of its frequency "components" as shown in Figure 2-2, where the time

Reproduced with permission of the copyright owner. Further reproduction prohibited without permission.

domain signal is "synthesized" from a sum of sine waves whose frequencies are multiples of the reciprocal of the period of the time domain signal.

For the physical applications, it is usual to sample the time domain signal (from a spectrometer detector for example) at N equally spaced time intervals, t = T/N, 2T/N,.....,T, to give a set of N time domain data points (the amplitude of the time domain signal at each of the sampled times), $y(t_1)$, $y(t_2)$,.....,$y(t_N)$. As for the continuous time domain signals of Figures 2-1 and 2-2, it is possible to represent each time domain data point in terms of a series of frequency domain amplitudes, $x(\omega_1)$,$x(\omega_2)$,.....$x(\omega_N)$, where the frequencies ω_1, ω_2,....ω_N are integral multiples of 1/T [1]:

$$y(t_1) = a_{11}\, x(\omega_1) + a_{12}\, x(\omega_2) + \ldots\ldots + a_{1N}\, x(\omega_N)$$

$$y(t_2) = a_{21}\, x(\omega_1) + a_{22}\, x(\omega_2) + \ldots\ldots + a_{2N}\, x(\omega_N) \qquad (2\text{-}1)$$

$$y(t_N) = a_{N1}\, x(\omega_1) + a_{N2}\, x(\omega_2) + \ldots\ldots + a_{NN}\, x(\omega_N)$$

where

$$t_n = n(T/N), \qquad n=1,2...,N \qquad (2\text{-}2)$$

Reproduced with permission of the copyright owner. Further reproduction prohibited without permission.

$$\omega_m = (2\pi m/T), \qquad m=1,2,...,N \qquad (2\text{-}3)$$

$$a_{nm} = \exp[i\omega_m t_n] = \exp[2\pi i nm/N] \qquad (2\text{-}4)$$

The a_{nm} represent the phases, see Figure 2-2, of each frequency component, using complex notation for brevity. In this notation, a phase factor $\exp(i\theta)$ indicates a phase angle of θ radians, as illustrated in Figure 2-2. For example, $\theta = 0$ denotes a pure cosine wave whose phase factor is $\exp(0) = 1$, while $\theta = \pi/2$ denotes a pure sine wave whose phase factor is $\exp(i\pi/N) = i$; etc. Since there are N independent known sampled time domain amplitudes, $y(t_1)$ to $y(t_N)$, each expressed in terms of all N desired discrete frequency domain spectral amplitudes, $x(\omega_1)$ to $x(\omega_N)$, it is possible to "decode" the sampled time domain data to obtain the desired discrete frequency domain amplitude spectrum, simply by solving the N linear algebraic equations in N unknowns of equation 2-1. For the particular choice of equally spaced time domain samples and equally spaced frequency domain amplitudes equations 2-1 and 2-3, the decoding procedure is called a

Reproduced with permission of the copyright owner. Further reproduction prohibited without permission.

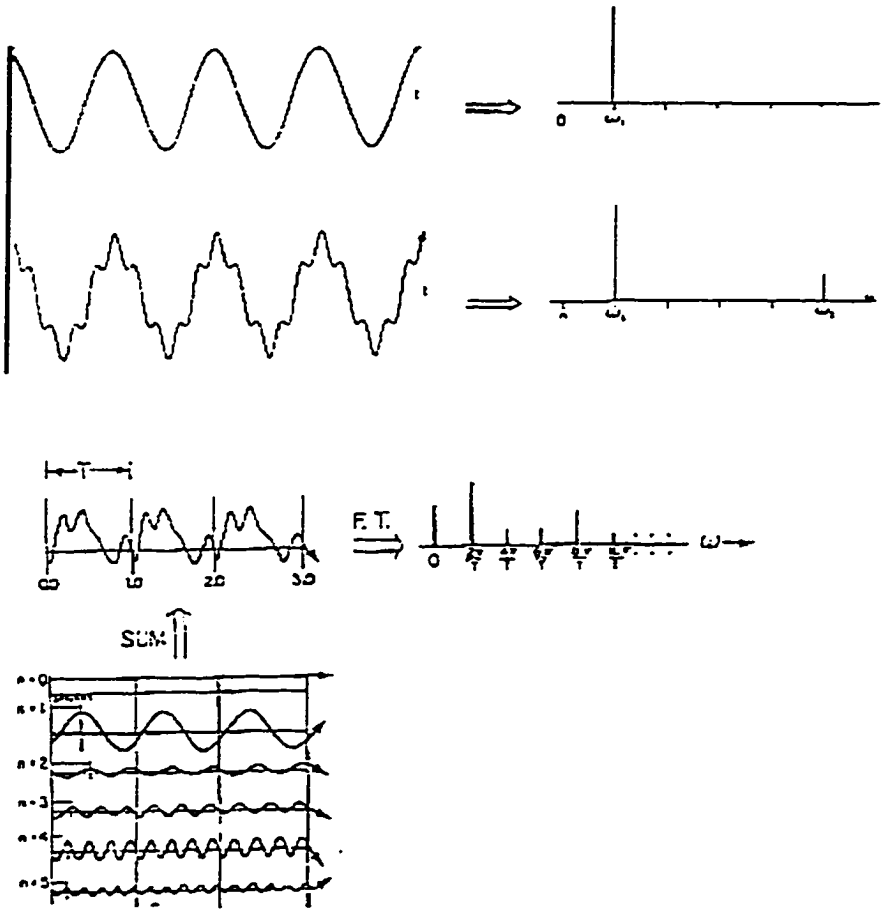

Figure 2-1: *Representing a sine wave in time and frequency domains.*
Figure 2-2: *Representing a periodic time domain signal in terms of frequency domain*
Adapted from ref. [1]

Reproduced with permission of the copyright owner. Further reproduction prohibited without permission.

(discrete) Fourier transformation and equation 2-1 may be solved rapidly and reliably by a digital computer, using the fast Fourier transform technique. The fast Fourier transform (FFT) algorithm [1,2,3,4] will be discussed later. It is therefor necessary to relate the properties of the continuous integral transforms introduced in [section 1-1, chapter 1], to the properties of the finite Fourier transform in order to take advantage of digital computers and the fast Fourier transform algorithm.

In the following sections, a brief mathematical background of the Fourier integral and Fourier series, and the correspondence between the finite Fourier transform and the Fourier integral is described.

The method of FFT which is used to compute the Fourier integral is discussed in detail. Finally, the results and the effect of different types of apodization functions, zero fillings and phase correction are evaluated.

Reproduced with permission of the copyright owner. Further reproduction prohibited without permission.

2.2- Fourier integrals

The Fourier integral is defined by the expression :

$$H(f) = \int_{-\infty}^{\infty} h(t) \exp(-i2\pi ft) dt \qquad (2\text{-}5)$$

If the integral exists for every value of the parameter f, then equation 2-5 defines H(f) the Fourier transform of h(t). h(t) is the time domain and H(f) is the frequency domain or any other domain.

In general, the Fourier transform is a complex operation:

$$H(f) = R(f) + iI(f) = |H(f)| \exp i\theta(f) \qquad (2\text{-}6)$$

where

R(f) is the real part of the Fourier transform,

I(f) is the imaginary part of the Fourier transform,

$|H(f)|$ is the amplitude or Fourier Spectrum of h(t) and is given by

$$[R^2(f) + I^2(f)]^{1/2},$$

θ (f) is the phase angle of the Fourier transform and is given by

$$\tan^{-1} [I(f)/R(f)]$$

Reproduced with permission of the copyright owner. Further reproduction prohibited without permission.

2.3- Sampling theorems and discrete Fourier transform

In the previous section, the basic concept of the Fourier series and Fourier transform is given. We may consider the Fourier series to be an operation that takes a function f(x) and returns a sequence of coefficients α_n . By the same token, the Fourier transform may be considered an operation that maps a function f(x) to another function F(ν). To determine either the Fourier series or Fourier transform of a function we must evaluate one or more integral. Thus, it is only possible to consider functions that can be described analytically and even then these functions must be relatively uncomplicated. In the real world we rarely find such a nice function and, therefore, must turn to digital computers for help. A digital computer, however, does not digest functions but instead, a sequence of numbers that can be handled by computer. The question is: How does the discrete Fourier transform relate to the continuous Fourier transform? To answer this question, it is preferable to derive the discrete Fourier Transform as a special case of continuous Fourier transform theory. Clearly, the discrete

Reproduced with permission of the copyright owner. Further reproduction prohibited without permission.

Fourier transform can be defined independently of the Fourier transform. However, as mentioned above, many applications involving the continuous Fourier transform rely on a digital computer for implementation, which leads to the use of the discrete Fourier transform (DFT) and hence the fast Fourier transform (FFT). Both approaches yield identical results; the distinction is in the interpretation of the results.

The derivation of the DFT is described somewhere else [2,3,4]; here, the DFT equation will be discussed without derivation, relying on Figure 2-3. The DFT equation is:

$$X(n) = \sum_{k=0}^{N-1} x_0(k) \exp(-i2\pi nk/N) \qquad n=0,1,.....,N-1 \qquad (2\text{-}7)$$

where X(n) is the n^{th} frequency domain point, and $x_0(k)$ is the k^{th} time domain point. This equation is similar to the definition of the Fourier coefficient in a Fourier series expansion. If the function h(t) is continuous at t=T, then a sample of h(t) at time equal to T is expressed as

$$h`(t) = h(t)\,\delta(t-T) = h(T)\delta(t-T) \qquad (2\text{-}8)$$

Reproduced with permission of the copyright owner. Further reproduction prohibited without permission.

The impulse that occurs at time T has an area equal to the function value at time T. If h(t) is continuous at t=nT for n= $0, \pm1, \pm2, \ldots$,

$$h`(t) = \sum_{n=-\infty}^{\infty} h(nT)\ \delta(t-nT) \qquad (2\text{-}9)$$

h`(t) is termed the sampled waveform of h(t) with sample interval T. The sampled function h(t) is then an infinite sequence of equidistant impulses, the amplitude of which is given by the value of h(t) corresponding to the time of occurrence of the impulse. Figure 2-3 illustrates graphically the sampling concept [2,3,5,6]. As illustrated in this Figure, the sampled function Figure 2-3e is equal to the product of the waveform h(t) shown in Figure 2-3a and the sequence of impulses $\Delta(t)$ illustrated in Figure 2-3b Δ is called the sampling function or the Dirac delta comb and its defined as an infinite train of equally spaced (T) impulse function. When we multiply the analog function with the Dirac delta comb, the Fourier transform of the interferogram (i.e., the spectrum) is convolved with the Dirac delta comb. The effect of this convolution is to repeat the spectrum ad infinitum, see Figure

Reproduced with permission of the copyright owner. Further reproduction prohibited without permission.

2-3f. If the spectrum covers the bandwidth 0 to ν_{max} the transformed Dirac delta comb must have a period of at least 2 ν_{max}; otherwise the spectra will overlap as a result of the convolution (this will be discussed later).

Reproduced with permission of the copyright owner. Further reproduction prohibited without permission.

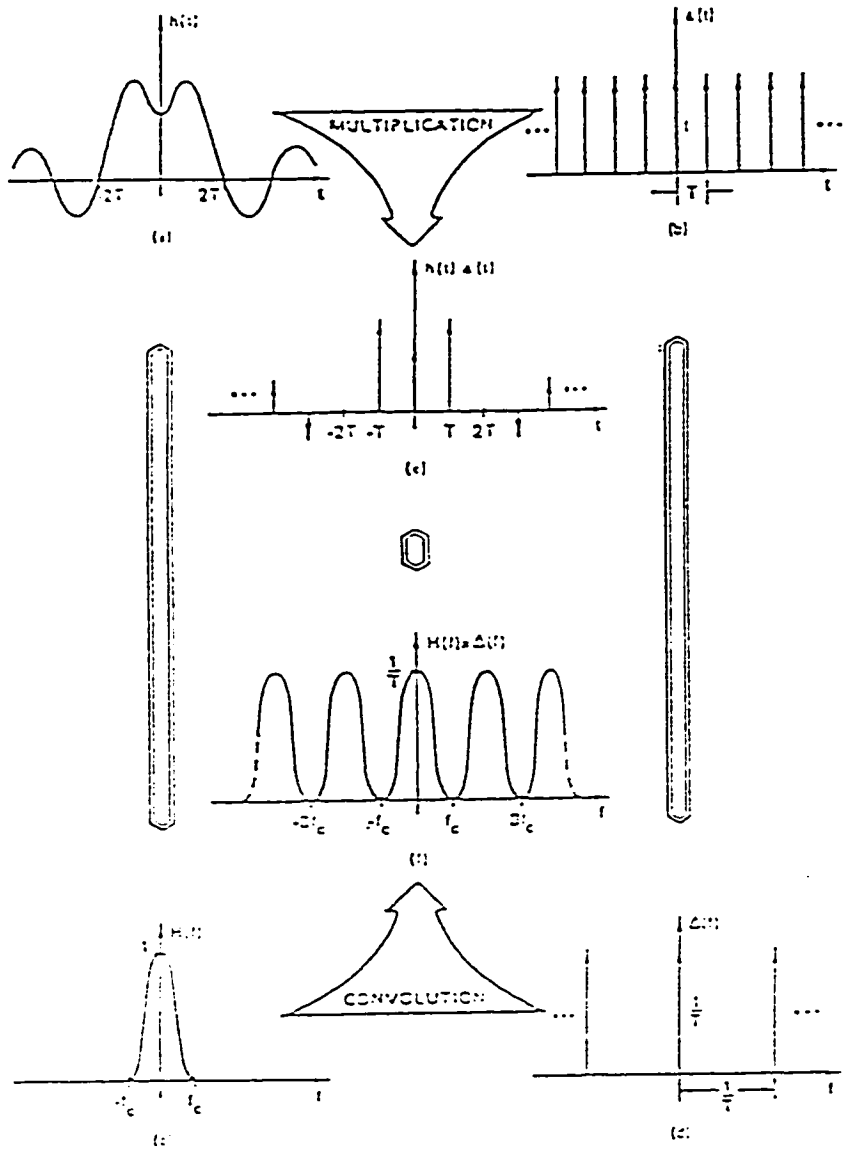

Figure 2-3: Graphical development of the discrete Fourier transform. Adapted from ref. [2]

Reproduced with permission of the copyright owner. Further reproduction prohibited without permission.

2.4- Problems associated with sampling

There are several problems associated with the sampling process. These problems will be discussed in the paragraphs below. To illustrate these problems let us assume that we wish to sample the function shown in the Figure 2-4. To obtain an accurate representation of this function, the sampling size (or sampling rate) Δx must be small in comparison with "detail" of the function. A rough rule of thumb to determine how accurately the sampled sequence represents the function is to construct a smooth curve between the sampled values; the better the representation - the closer this curve will lie to the original function. Clearly the sampling scheme shown in Figure 2-5 is a poor representation of the original function Figure 2-4, because Δx is too large. When this is the situation we say that the data has been ***aliased*** [2,3,5,6].

The second common difficulty encountered in sampling a function is that of ***windowing*** [2,3,5,6]. An example of this is shown in Figure 2-6. In this case the sampling rate Δx appears to be adequate; however, instead of sampling the entire function we

Reproduced with permission of the copyright owner. Further reproduction prohibited without permission.

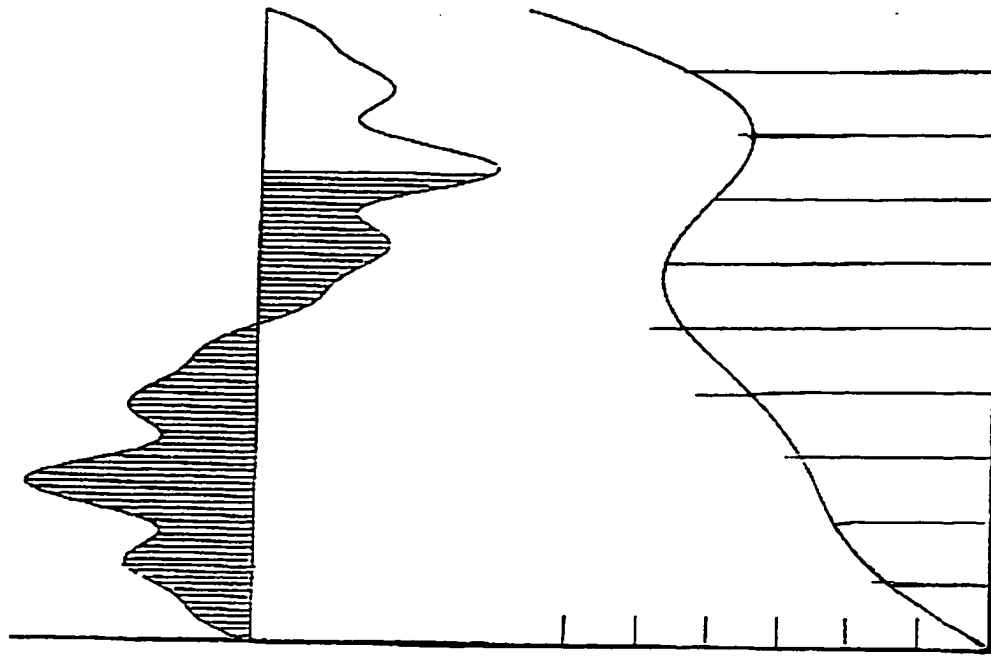

Example of winowing *Example of quantization*

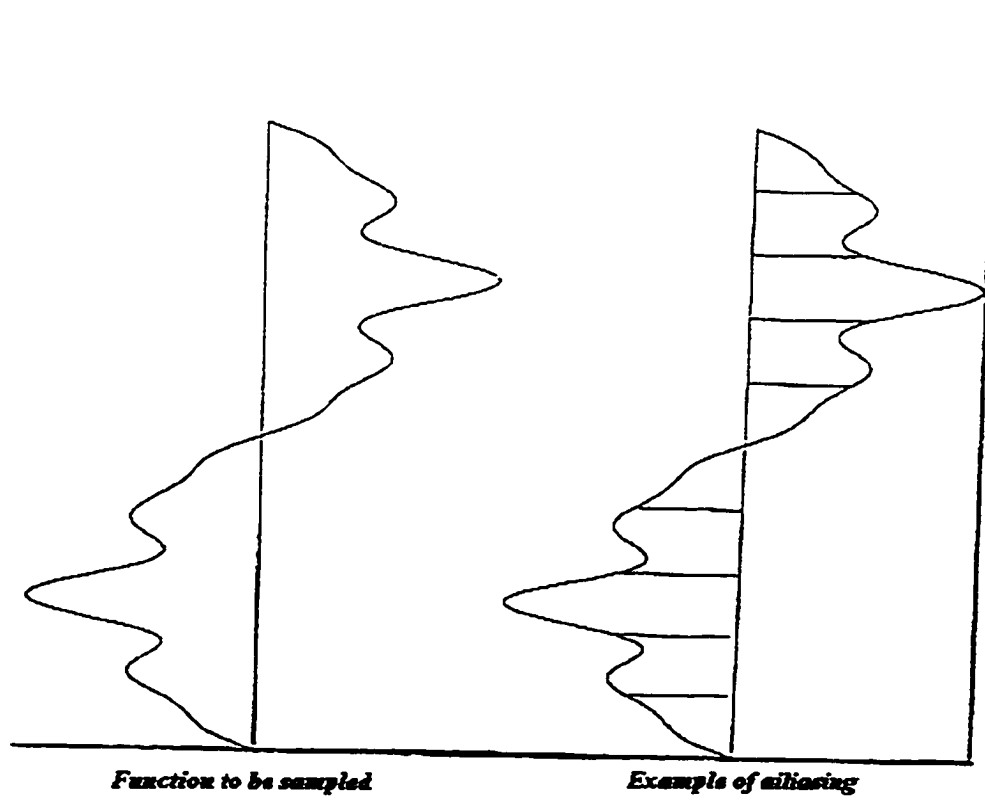

Function to be sampled *Example of ailiasing*

Figures: *2-4 Function to be sampled, 2-5 Example of ailiasing, 2-6 Example of windowing, 2-7 Example of quantization.*

Reproduced with permission of the copyright owner. Further reproduction prohibited without permission.

have sampled only a portion of it. Figuratively, we have placed a window over the function.

Quantization [2,3,5,6], the third common difficulty, is caused because we cannot digitize a function with infinitesimal accuracy but instead with only discrete levels. A "blow up" of a portion of our function is shown in Figure 2-7. In this case the A/D converter assigns a discrete value to the function (at the sampled points) that is, the function; is "rounded off" to the nearest digital level.

In order to sample an arbitrary function h(t) and obtain its Fourier transform, a number of steps are necessary [14] as described above which are summarized in Figure 2-8. If we sample an analog function at regular discrete intervals, we have in effect multiplied the function by a repetitive impulse function. First, the function is sampled by multiplying h(t) by the sampling function Δ_0 (t) illustrated in Figure 2-8b. The sampled function h`(t) and its Fourier transform are illustrated in Figure 2-8c. The Fourier transform in Figure 2-8c is not suitable for machine computation because an infinity of samples of h(t) is considered;

Reproduced with permission of the copyright owner. Further reproduction prohibited without permission.

it is necessary to truncate the sampled h`(t) so that only a finite number of points, say N, are considered. The rectangular, or truncation, function and its Fourier transform are illustrated in Figure 2-8d. The product of the infinite sequence of impulse functions representing h(t) and the truncation function yields the finite - length time function illustrated in Figure 2-8e. Truncation introduces the second modification of the original Fourier transform pair; this effect is to convolve the aliased frequency transform of Figure 2-8c with Fourier transform of the truncation function Figure 2-8d. As shown in Figure 2-8e, the frequency transform now has a ripple to it. The modified transform pair of Figure 2-8e is still not an acceptable discrete Fourier transform pair because the frequency transform is a continuous function. For machine computation, only sample values of the frequency function can be computed; it is necessary to modify the frequency transform by the frequency - sampling function illustrated in Figure 2-8f. The frequency - sampling interval is $1/T_0$. The DFT pair of Figure 2-8g is acceptable for the purpose of digital

Reproduced with permission of the copyright owner. Further reproduction prohibited without permission.

machine computation because both the time and frequency domains are represented by discrete values.

Reproduced with permission of the copyright owner. Further reproduction prohibited without permission.

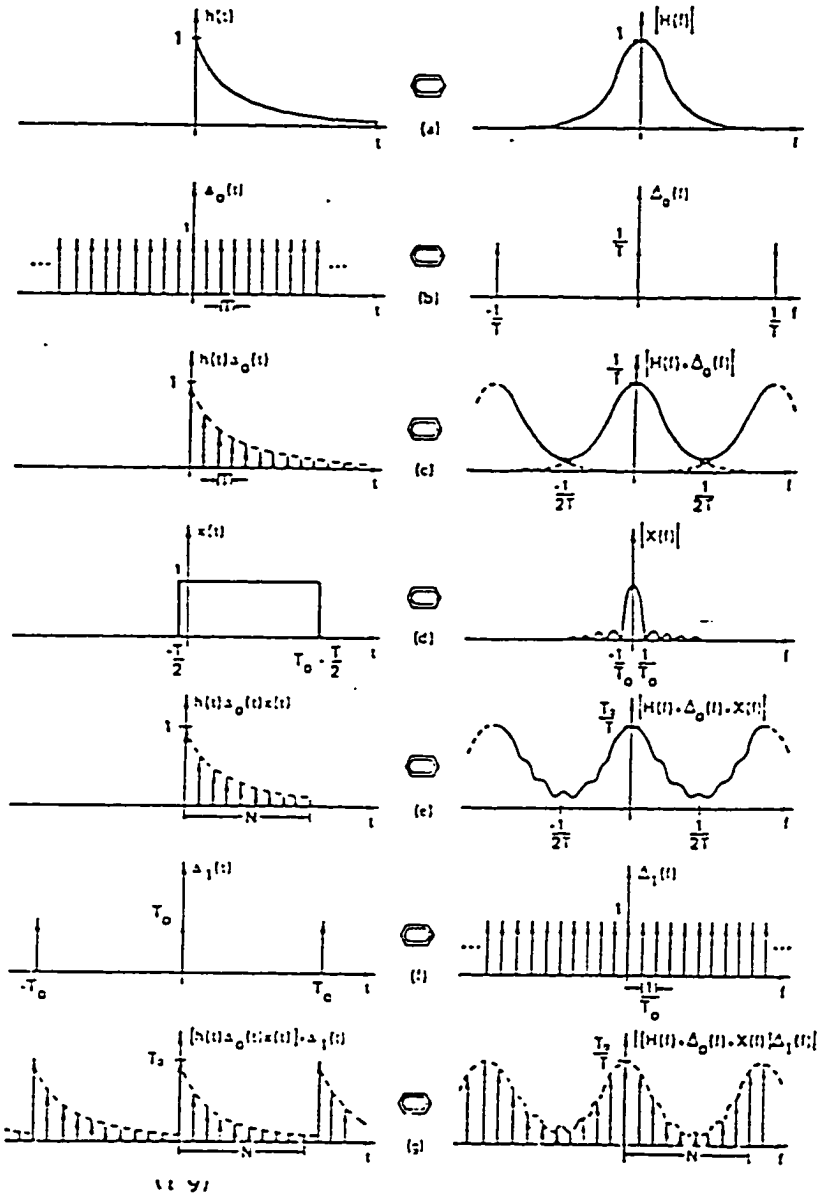

Figure 2-8: Fourier transform of a sampled function. Adapted from ref. [2]

Reproduced with permission of the copyright owner. Further reproduction prohibited without permission.

2.5- The Fast Fourier Transform

The fast Fourier transform (FFT) is an algorithm that was described by Cooly and Tukey [1-6], in which the number of necessary computations is drastically reduced when compared to the discrete Fourier transform DFT. The FFT is based on the idea that the actual DFT expression can be expressed in general matrix form, and that matrix can be factored in a manner that will reduce the overall number of computations [1-4] .

In this section, the matrix formulation, the signal flow graph and a detail discussion about the computational process is described.

2.5.1- Matrix formulation

As stated earlier, the discrete digital expression for the Fourier transform is given by the equation:

$$X(n) = \sum_{k=0}^{N-1} x_0(k) \exp(-i2\pi nk/N) \quad n=0,1,.....,N-1 \qquad (2\text{-}10)$$

Reproduced with permission of the copyright owner. Further reproduction prohibited without permission.

In this equation $x_0(k)$ is the k^{th} time domain point and X(n) is the n^{th} frequency domain point. The x_0 may be, and the X always are complex numbers.

For example, if N=4 equation 2-7 can be written as

$$\begin{aligned} X(0) &= x_0(0)\,W^0 + x_0(1)\,W^0 + x_0(2)\,W^0 + x_0(3)\,W^0 \\ X(1) &= x_0(0)\,W^0 + x_0(1)\,W^1 + x_0(2)\,W^2 + x_0(3)\,W^3 \\ X(2) &= x_0(0)\,W^0 + x_0(1)\,W^2 + x_0(2)\,W^4 + x_0(3)\,W^6 \\ X(3) &= x_0(0)\,W^0 + x_0(1)\,W^3 + x_0(2)\,W^6 + x_0(3)\,W^9 \end{aligned} \qquad (2\text{-}11)$$

where

$$W = \exp(-i2\pi/N) \qquad (2\text{-}12)$$

Equation 2-11 can be more easily represented in matrix form:

$$\begin{bmatrix} X(0) \\ X(1) \\ X(2) \\ X(3) \end{bmatrix} = \begin{bmatrix} W^0W^0W^0W^0 \\ W^0W^1W^2W^3 \\ W^0W^2W^4W^6 \\ W^0W^3\,W^6W^9 \end{bmatrix} \begin{bmatrix} x_0(0) \\ x_0(1) \\ x_0(2) \\ x_0(3) \end{bmatrix} \qquad (2\text{-}13)$$

or

$$X(n) = W^{nk}\,x_0(k) \qquad (2\text{-}14)$$

Since W and $x_0(k)$ may be complex, N^2 complex multiplications and (N) (N-1) complex additions are necessary to perform the required matrix computation. The FFT owes its success to the

Reproduced with permission of the copyright owner. Further reproduction prohibited without permission.

fact that the algorithm reduces the number of multiplications and additions required in the computation of (equation 2-13).

The complex exponential [exp(-i2π/N)] possess the circular property of repeating itself with period N:

$$\exp(-i2\pi nk/N) = \exp(-i2\pi |nk|_N/N \quad (2\text{-}15)$$

where $|nk|_N$ is the modulo of N. Thus, one can write equation 2-14 as

$$W^{nk} = W^{nk(\text{modulo N})} \quad (2\text{-}16)$$

where [nk mod(N)] is the remainder upon division of nk by N. Hence, if N=4, n=3, and k=3, then $W^9 = W^1$ For N=4 this means that $W^4 = W^0$, $W^6 = W^2$ and $W^9 = W^1$. Moreover, when N is any even number, then each value of W^{nk} is always equal to the negative of one that is opposite to it. Thus, for N=4 , $W^2 = -W^0$ and $W^3 = -W^1$.

Therefore, equation 2-13 can be further reduced to

$$\begin{bmatrix} X(0) \\ X(1) \\ X(2) \\ X(3) \end{bmatrix} = \begin{bmatrix} W^0 & W^0 & W^0 & W^0 \\ W^0 & W^1 & -W^0 & -W^1 \\ W^0 & -W^0 & W^0 & -W^0 \\ W^0 & -W^1 & -W^0 & W^1 \end{bmatrix} \begin{bmatrix} x_0(0) \\ x_0(1) \\ x_0(2) \\ x_0(3) \end{bmatrix} \quad (2\text{-}17)$$

Reproduced with permission of the copyright owner. Further reproduction prohibited without permission.

From equation 2-16 we observe, that only W^0 and W^1 need to be evaluated, and that the remaining distinct values of W, namely W^2 and W^3 do not appear in equation 2-17. Thus only half of all of the possible values of W^{nk} will need to be evaluated. For the case N=4, for example, $W^0 = 1$, and we see that in fact we only need to evaluate W^1, which is equal to $(-i)$. Therefore, we can write the so-called ***Fourier matrix*** [10] as :

$$X = Mx \qquad M = W^{nk}$$

$$= [W^{nk}] = \begin{bmatrix} 1 & 1 & 1 & . & 1 \\ 1 & W & W^2 & . & W^{n-1} \\ 1 & W^2 & W^4 & . & W^{2(n-1)} \\ . & . & . & . & . \\ 1 & W^{n-1} & W^{2(n-1)} & . & W^{(n-1)^2} \end{bmatrix} \qquad (2\text{-}18)$$

$$= \begin{bmatrix} 1 & 1 & 1 & 1 \\ 1 & W & W^2 & W^3 \\ 1 & W^2 & W^4 & W^6 \\ 1 & W^3 & W^6 & W^9 \end{bmatrix} = \begin{bmatrix} 1 & 1 & 1 & 1 \\ 1 & W^1 & -W^0 & -W^1 \\ 1 & -W^0 & W^0 & -W^0 \\ 1 & -W^1 & -W^0 & W^1 \end{bmatrix} \text{ for N=4}$$

The second step in the FFT algorithm is to factor the sequence matrix in equation 2-16 as follows:

$$\begin{bmatrix} X(0) \\ X(2) \\ X(1) \\ X(3) \end{bmatrix} = \begin{bmatrix} 1 & W^0 & 0 & 0 \\ 1 & -W^0 & 0 & 0 \\ 0 & 0 & 1 & W^1 \\ 0 & 0 & 1 & -W^1 \end{bmatrix} \begin{bmatrix} 1 & 0 & W^0 & 0 \\ 0 & 1 & 0 & W^0 \\ 1 & 0 & -W & 0 \\ 0 & 1 & 0 & -W \end{bmatrix} \begin{bmatrix} x_0(0) \\ x_0(1) \\ x_0(2) \\ x_0(3) \end{bmatrix} \qquad (2\text{-}19)$$

Reproduced with permission of the copyright owner. Further reproduction prohibited without permission.

Note first that the indices of the vector on the LHS are no longer in their natural order. This reordering is the an inherent part of the factorization process. The method of factorization is based on the theory of the FFT algorithm, which will be discussed later in this chapter. We now split equation 2-19 into the following two matrix multiplication and a bit reversal stage.

stage (1)

$$\begin{bmatrix} X(0) \\ X(1) \\ X(2) \\ X(3) \end{bmatrix} = \begin{bmatrix} 1 & 0 & W^0 & 0 \\ 0 & 1 & 0 & W^0 \\ 1 & 0 & -W & 0 \\ 0 & 1 & 0 & -W \end{bmatrix} \begin{bmatrix} x_0(0) \\ x_0(1) \\ x_0(2) \\ x_0(3) \end{bmatrix} \tag{2-20}$$

stage (2)

$$\begin{bmatrix} X(0) \\ X(1) \\ X(2) \\ X(3) \end{bmatrix} = \begin{bmatrix} 1 & W^0 & 0 & 0 \\ 1 & -W^0 & 0 & 0 \\ 0 & 0 & 1 & W^1 \\ 0 & 0 & 1 & -W^1 \end{bmatrix} \begin{bmatrix} x_0(0) \\ x_0(1) \\ x_0(2) \\ x_0(3) \end{bmatrix} \tag{2-21}$$

Bit reversal

$$\begin{bmatrix} X(0) \\ X(1) \\ X(2) \\ X(3) \end{bmatrix} \rightarrow \begin{bmatrix} x_0(0) \\ x_0(2) \\ x_0(1) \\ x_0(3) \end{bmatrix} \tag{2-22}$$

Reproduced with permission of the copyright owner. Further reproduction prohibited without permission.

In stage 1, we started with x_0, which is the data vector obtained from the analytical definition of the input function. This is transformed in 2-20 to produce the stage 1 vector x_1. In stage 2 the vector x_1 is transformed to produce the stage 2 vector x_2.

Finally, in the bit reversal, x_2 is resequenced to produce the output vector X. From the equations above, we see that column vector $x_1(k)$ is equal to the product of the two matrices on the right in equations 2-20 and 2-21.

Element $x_1(0)$ is computed by one complex multiplication and one complex addition :

$$x_1(0)=x_0(0) + W^0x_0(2) \qquad (2\text{-}23)$$

Element $x_1(1)$ is also determined by one complex multiplication and addition. Only one complex addition is required to compute $x_1(2)$ because $W^0 = W^2$, therefore

$$\begin{aligned} x_1(2) &= x_0(0) + W^2x_0(2) \\ &= x_0(0) - W^0x_0(2) \qquad (2\text{-}24) \end{aligned}$$

where the complex multiplication $W^0x_0(2)$ has already been computed in the determination of $x_1(0)$. By the same reasoning, $x_1(3)$ is computed by only one complex addition and no

Reproduced with permission of the copyright owner. Further reproduction prohibited without permission.

multiplications. The intermediate vector $x_1(k)$ is then determined by four complex additions and two complex multiplications. Term $x_2(1)$ is computed by one addition because $W^0 = -W^2$. By the same reasoning, $x_2(2)$ is determined by one complex multiplication and addition, and $x_2(3)$ by only one addition. It is convenient to choose the number of sample points of $x_0(k)$ according to the relation $N= 2^\gamma$, where γ is an integer.

For $N= 2^\gamma$, the FFT algorithm is simply a procedure for factoring an N x N matrix into γ matrices (each N x N), such that each of the factored matrices has the special property of minimizing the number of complex multiplication's and additions. We note from the illustration above that the FFT requires $N\gamma/2$ complex multiplications and $N\gamma$ complex additions, whereas the direct method requires N^2 complex multiplications and N(N-1) complex additions. If we assume that computing time is proportional to the number of multiplications, then the approximate ratio of computing time for DFT *vs.* FFT is given by:

$$\frac{N^2}{N\gamma/2} = \frac{2N}{\gamma} \qquad (2\text{-}25)$$

Reproduced with permission of the copyright owner. Further reproduction prohibited without permission.

For N=1024 $=2^{10}$, for example, equation 1-47 produces a computational reduction of more than 200 to 1.

2.5.2- The signal flow graph

It is easy to understand the Fourier transform calculation process through the use of a signal flow graph [3,4,7], given in Figure 2-9. This graph shows the transform of eight complex points from the time domain (X's) to the frequency domain (A's). Each intersection at a dot represents the complex addition of two points to form a new point, and each W term alongside a line represents complex multiplication of that point by that power of W before the addition takes place. Thus each new point at a dot or node is calculated by:

$$X'_i = X_i + W^y X_k \qquad (2\text{-}26)$$

Where X'_i is the new point, y the power of W at that point, and X_k another X point with which it is combined.

Looking further into the graph, we see that there are several intermediate columns of points calculated between the original X's and the final A's . Each of these columns is called a pass and represents an intermediate result in the transform process. There

Reproduced with permission of the copyright owner. Further reproduction prohibited without permission.

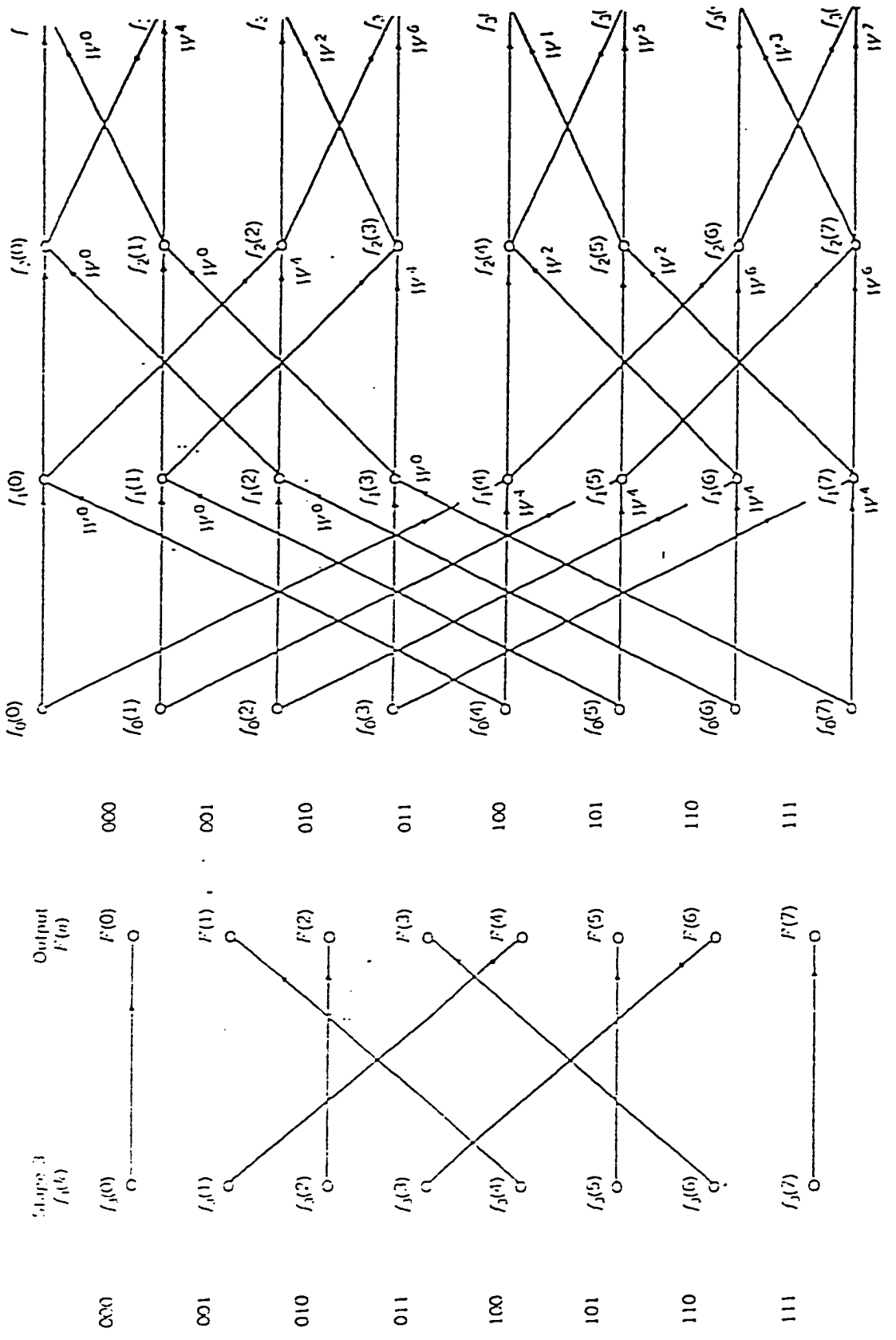

Figure 2-9: *FFT flow graph of N = 8. Adapted from ref. [3]*

Reproduced with permission of the copyright owner. Further reproduction prohibited without permission.

will always be $\log_2 N = \gamma$ passes through the transform for N complex points.

Within each pass we see that only two points contribute each new point and that these two points subsequently influence only two other points in the next pass. The two equations describing these two points have the form:

$$X'_1 = X_1 + X_2 W^{r} \quad , \quad X'_2 = X_1 + X_2 W^{z} \qquad (2\text{-}27)$$

Thus one can carry out this transform in place since one operates on a pair of points at a time.

The basic idea of a signal flow graph is that nodes, shown as small circles in the two figures, have inputs and outputs (information pipes) shown by the arrows entering and leaving them. The rules are as follows:

- Multiple inputs entering a node are added.
- The arrowheads may have values associated with them, shown in Figure 2-10 as various powers of W. The information flowing along any of these lines is multiplied by the power of W shown next to it. If no explicit multiplier is shown, then multiplication by unity is implied.

Reproduced with permission of the copyright owner. Further reproduction prohibited without permission.

Every node is computed from precisely two inputs, the upper of which always has a multiplier of 1 and the lower of which always appear with a multiplier W^p with various values of p.

Figure 2-10 can be summarized as follows:

The stage 1 vector is computed from the input vector by the following four equations:

$$\begin{aligned} x_1(0) &= x_0(0) + W^0 x_0(2) \\ x_1(2) &= x_0(0) - W^0 x_0(2) \\ x_1(1) &= x_0(0) + W^0 x_0(3) \\ x_1(3) &= x_0(0) - W^0 x_0(3) \end{aligned} \tag{2-28}$$

The stage 2 vector is computed from the stage 1 vector by the following equations:

$$\begin{aligned} x_2(0) &= x_1(0) + W^0 x_1(1) \\ x_2(2) &= x_1(0) - W^0 x_1(1) \\ x_2(1) &= x_1(2) + W^1 x_1(3) \\ x_2(3) &= x_1(2) - W^1 x_1(3) \end{aligned} \tag{2-29}$$

Reproduced with permission of the copyright owner. Further reproduction prohibited without permission.

The final stage is unscrambling the FFT, and its obtained as follows:

$$\begin{bmatrix} X(00) \\ X(01) \\ X(10) \\ X(11) \end{bmatrix} = \begin{bmatrix} x_2(00) \\ x_2(10) \\ x_2(01) \\ x_2(11) \end{bmatrix} \quad (2\text{-}30)$$

2.5.2.1- Dual nodes

Inspection of Figure 2-10 reveals that in every array we can always find two nodes whose input transmission path stem from the same pair of nodes in the previous array. For example, nodes $x_1(0)$ and $x_1(8)$ are computed in terms of nodes $x_0(0)$ and $x_0(8)$. Note that nodes $x_0(0)$ and $x_0(8)$ do enter into the computation of any other node. We define such nodes as a dual - node pair.

2.5.2.2- Dual node separation

In stage 1 of Figure 2-10, $x_1(0)$ and $x_1(2)$ are both computed from the same two inputs coming from the previous stage. For this reason, they are known as a dual - node pair.

The upper input to the pair, $x_0(0)$, is called the primary source node, and the lower input, $x_2(2)$ is called the secondary source node. Observe that the dual - node pair and its source nodes have

Reproduced with permission of the copyright owner. Further reproduction prohibited without permission.

exactly the same indices, that is, they have the same vertical positions in the Figure, differing only in that the source node are in a previous stage.

The dual - node pairs in stage 1 are two nodes apart, and in stage 2 they are one node apart. In terms of N and the stage number, which we shall call l, we have the following rule:

$$\text{Dual node separation} = N/2^{l} \qquad (2\text{-}31)$$

Reproduced with permission of the copyright owner. Further reproduction prohibited without permission.

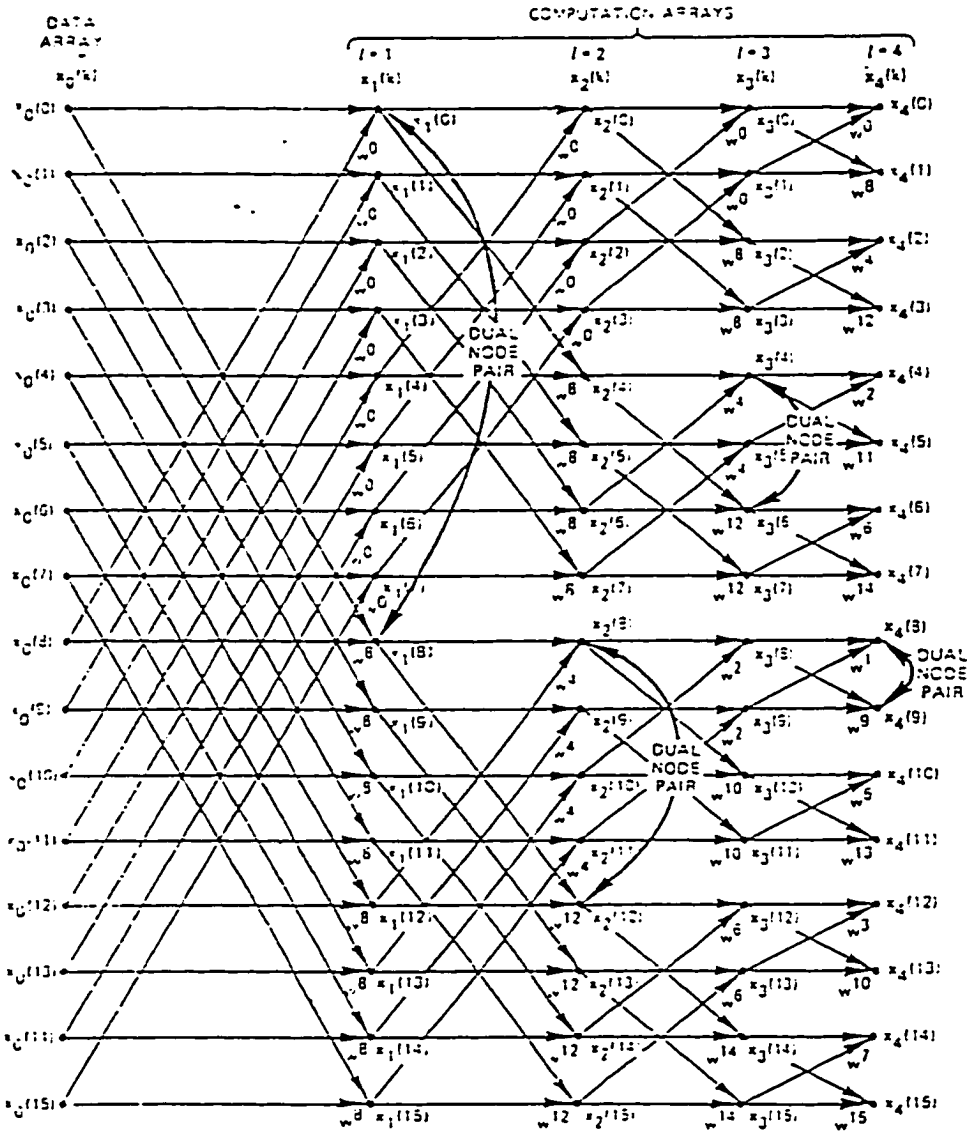

Figure 2-10: Dual - node computation. Adapted from ref. [2]

Reproduced with permission of the copyright owner. Further reproduction prohibited without permission.

2.5.2.3- The form of W

We have defined the matrix W as [1]

$$W = \exp(-i2\pi/N) \tag{2-32}$$

However, this particular form is quite time consuming to use, since the calculation of a number of exponential can be very slow and awkward in the computer. Instead, we invoke Euler's formula:

$$\exp(iy) = \cos(y) + i \sin(y) \tag{2-33}$$

and then represent W as

$$W^{y} = \exp(-i2\pi y/N) = \cos(-2\pi y/N) + i \sin(-2\pi y/N) \tag{2-34}$$

For y =3, for example, we have

$$W^{3} = \exp(6\pi i/8) = \cos(0.75\pi) + i \sin(0.75\pi) = -0.707+0.707i \tag{2-35}$$

Since all of the X are complex , we need to multiply the complex number X by the complex number derived from W. We further note that the exponents of W for X'1 and X'2, which we term y and z above, are related in that they differ by N/2:

$$z = y + N/2 \tag{2-36}$$

Reproduced with permission of the copyright owner. Further reproduction prohibited without permission.

and that :

$$W^{z} = W^{y+N/2} = W^{y} \exp(-i2\pi N/2N) = W^{y}(-1) \qquad (2\text{-}37)$$

Thus we have :

$$W^{z} = - W^{y} \qquad (2\text{-}38)$$

The two equations , that we evaluate for any pair of complex can then be written as :

$$X'_1 = X_1 + X_2 W^{y} \qquad (2\text{-}39)$$

$$X'_2 = X_1 - X_2 W^{y}$$

If we expand the representations of X to represent the real and imaginary coefficients,

$$X_1 = R_1 + i I_1 , \qquad X_2 = R_2 + i I_2 \qquad (2\text{-}40)$$

we can expand equation 2-39 to:

$$X'_1 = R_1 + i I_1 = (R_1 + i I_1) + (R_2 + i I_2)(\cos y + i \sin y) \qquad (2\text{-}41)$$

$$X'_2 = R_2 + i I_1 = (R_1 + i I_1) - (R_2 + i I_2)(\cos y + i \sin y)$$

Collecting terms, we have : $R'_1 = R_1 + R_2 \cos y - I_2 \sin y$

$$R'_2 = R_1 - R_2 \cos y - I_2 \sin y \qquad (2\text{-}42)$$

$$I'_1 = I_1 + R_2 \sin y + I_2 \cos y$$

$$I'_2 = I_1 - R_2 \sin y - I_2 \cos y$$

Reproduced with permission of the copyright owner. Further reproduction prohibited without permission.

These are the fundamental equations of the Fourier transform, and they are evaluated for all complex points for a given set of y's to form one pass through the data.

In applying the FFT, we often consider only functions to be real of time, whereas the frequency functions are, in general, complex. The FFT computer program may be used to calculate both the discrete transform and its inverse is written such that a complex time waveform is assumed :

$$H(n) = \frac{1}{N} \sum_{k=0}^{N-1} [h_r(k) + i\, h_i(k)] \exp(-i2\pi nk/N) \qquad (2\text{-}43)$$

If the time function being considered is real, (scientific data is, in fact, all real) we must set to zero the imaginary part of the complex time function in equation 2-43. This approach is inefficient in that the computer program still performs the multiplications involving $h_i(k)$ even though $ih_i(k)$ is zero. Therefore, its more efficient if we split the data into two parts, real and imaginary and each of them used to compute the transform of a function simultaneously.

Two techniques were developed for using this imaginary part of the complex time function to more efficiently compute the FFT of

Reproduced with permission of the copyright owner. Further reproduction prohibited without permission.

real functions. The detail of the techniques is discussed somewhere else; here I give only a summary of the method that were used for our computational purpose in building the FTVCD. In this method, the data is divided into odd and even points which are arbitrarily called real and imaginary points for the purpose of the transform. Next, the data is shuffled so that the real part is in the first half of the array (pass) and the imaginary in the second half of the array. Finally, the complex transform of these data is computed.

Reproduced with permission of the copyright owner. Further reproduction prohibited without permission.

2.6- Theoretical development of the base-2 FFT algorithm

So far we used a matrix argument to develop an understanding of why the FFT is an efficient algorithm. We then constructed a signal flow graph that described the algorithm for any $N=2^{\gamma}$. In this section, we relate each of these developments to a theoretical basis [2].

It desirable to represent k and n in the DFT equation

$$X(n) = \sum_{k=0}^{N-1} x_0(k) \exp(-i2\pi nk/N) \qquad n=0,1,.....,N-1$$

as an integer power of 2 ; that is, if we assume N=4, then γ =2 and we can represent k and n as two - bit binary numbers

$k=0,1,2,3$ or $k = (k_1, k_0) = 00, 01, 10, 11$

$n=0,1,2,3$ or $n = (n_1, n_0) = 00, 01, 10, 11$

A compact method of writing k and n is

$$k= 2k_1 + k_0 \qquad n= 2n_1 + n_0 \qquad (2\text{-}44)$$

Using the representations in equation 2-44, we can rewrite the DFT equation for the case N=4 as

Reproduced with permission of the copyright owner. Further reproduction prohibited without permission.

$$X(n_1, n_0) = \sum_{k_0=0}^{1} \sum_{k_1=0}^{1} x_0(k_1, k_0)\, W^{(2n_1 + n_0)(2k_1 + k_0)} \qquad (2\text{-}45)$$

We see that the single summation in equation for DFT must be replaced by γ (in case of N=4 , $\gamma = 2$) summations in order to enumerate all the bits of the binary representation of k.

After factoring W^p, (since $W^{a+b} = W^a W^b$) , equation 2-45 can be written in the form

$$X(n_1, n_0) = \sum_{k_0=0}^{1} \left[\sum_{k_1=0}^{1} x_0(k_1, k_0)\, W^{2 n_0 k_1} \right] W^{(2n_1 + n_0) k_0} \qquad (2\text{-}46)$$

This equation represents the foundation of the FFT algorithm. By considering each of the summations of this equation individually, we can form the matrices for the case N=4 from the equations below:

$$x_1(n_0, k_0) = \sum_{k_1=0}^{1} x_0(k_1, k_0)\, W^{2\, n0k1} \qquad (2\text{-}47)$$

$$x_2(n_0, n_1) = \sum_{k_0=0}^{1} x_1(n_0, k_0)\, W^{(2n1 + n0)\, k0}$$

$$X(n_1, n_0) = x_2(n_0, n_1)$$

The first two summation equations represent the two matrices demonstrated in stage 1 and stage 2 of (equation 2-19) , and the third one represents the bit reversal matrix of the same equation.

Reproduced with permission of the copyright owner. Further reproduction prohibited without permission.

As mentioned above, the basic idea of FFT is to factorize the N x N matrix into a smaller matrices so that we will have as many as zeros as possible to make the computational proceed faster. This means that for $N=2^{\gamma}$ data points, γ[N x N] matrix equations can be obtained,

$$[NxN] \Rightarrow \begin{bmatrix} N/2 & 0 \\ 0 & N/2 \end{bmatrix} \Rightarrow \begin{bmatrix} N/4 & 0 & 0 & 0 \\ 0 & N/4 & 0 & 0 \\ 0 & 0 & N/4 & 0 \\ 0 & 0 & 0 & N/4 \end{bmatrix} \Rightarrow \text{(2-48)}$$

This process of dividing the problem into simpler problems of half the size can be carried out γ-1 times, leading finally to a stage in which the matrix appears as

$$\begin{vmatrix} M & 0 & 0 & 0 & 0 & 0 \\ 0 & M & 0 & 0 & 0 & 0 \\ 0 & 0 & . & 0 & 0 & 0 \\ 0 & 0 & 0 & . & 0 & 0 \\ 0 & 0 & 0 & 0 & . & 0 \\ 0 & 0 & 0 & 0 & 0 & M \end{vmatrix} \qquad \text{(2-49)}$$

where M are $[2x2]$ matrix. This formula premultiplies a suitable rearrangement of the given vector coefficients x and converts that vector into the earliest or most "primitive" of the vector X vectors.

Reproduced with permission of the copyright owner. Further reproduction prohibited without permission.

To illustrate FFT algorithm farther, let us consider equation 2-7 for the case $N=8=2^3$. In this case, the binary representation for n and k will be:

$$n = 4n_2 + 2n_1 + n_0 \qquad n_i = 0 \text{ or } 1 \qquad (2\text{-}50)$$

$$k = 4k_2 + 2k_1 + k_0 \qquad k_i = 0 \text{ or } 1$$

Using the same procedure as for N=4, we can obtain the following equations to construct the matrices for N = 8:

$$x_1(n_0,k_1,k_0) = \sum_{k_2=0}^{1} x_0(k_2,k_1,k_0)\, W^{4n_0k_2}$$

$$x_2(n_0,n_1,k_0) = \sum_{k_1=0}^{1} x_1(n_0,k_1,k_0)\, W^{(2n_1+n_0)(2k_1)} \qquad (2\text{-}51)$$

$$x_3(n_0,n_1,n_2) = \sum_{k_0=0}^{1} x_2(n_0,n_1,k_0)\, W^{(4n_2+2n_1+n_0)(k_0)}$$

$$X(n_2,n_1,n_0) = x_3(n_0,n_1,n_2)$$

From these equations, now we form 4 matrices, 3 for three stages and one for the bit reversal:

Reproduced with permission of the copyright owner. Further reproduction prohibited without permission.

Stage 1

$$x_1(n_0,k_1,k_0) = \sum_{k_2=0}^{1} x_0(k_2,k_1,k_0)\, W^{4n_0k_2}$$

$$x_1(000) = x_0(000)\, W^0 + x_0(100)\, W^0$$

$$x_1(001) = x_0(001)\, W^0 + x_0(101)\, W^0$$

$$x_1(010) = x_0(010)\, W^0 + x_0(110)\, W^0$$

$$x_1(011) = x_0(011)\, W^0 + x_0(111)\, W^0$$

$$x_1(100) = x_0(000)\, W^0 + x_0(100)\, W^4$$

$$x_1(101) = x_0(001)\, W^0 + x_0(101)\, W^4$$

$$x_1(110) = x_0(010)\, W^0 + x_0(110)\, W^4$$

$$x_1(111) = x_0(011)\, W^0 + x_0(111)\, W^4$$

$$\begin{bmatrix} W^0 & 0 & 0 & 0 & W^0 & 0 & 0 & 0 \\ 0 & W^0 & 0 & 0 & 0 & W^0 & 0 & 0 \\ 0 & 0 & W^0 & 0 & 0 & 0 & W^0 & 0 \\ 0 & 0 & 0 & W^0 & 0 & 0 & 0 & W^0 \\ W^0 & 0 & 0 & 0 & W^4 & 0 & 0 & 0 \\ 0 & W^0 & 0 & 0 & 0 & W^4 & 0 & 0 \\ 0 & 0 & W^0 & 0 & 0 & 0 & W^4 & 0 \\ 0 & 0 & 0 & W^0 & 0 & 0 & 0 & W^4 \end{bmatrix} \begin{bmatrix} x_0(000) \\ x_0(001) \\ x_0(010) \\ x_0(011) \\ x_0(100) \\ x_0(101) \\ x_{01}(110) \\ x_{01}(111) \end{bmatrix} \qquad (2\text{-}52)$$

Reproduced with permission of the copyright owner. Further reproduction prohibited without permission.

Stage 2

$$x_2(n_0,n_1,k_0) = \sum_{k_1=0}^{1} x_1(n_0,k_1,k_0)\, W^{(2n_1+n_0)(2k_1)}$$

$$x_2(000) = x_1(000)\, W^0 + x_1(010)\, W^0$$

$$x_2(001) = x_1(001)\, W^0 + x_1(011)\, W^0$$

$$x_2(010) = x_1(000)\, W^0 + x_1(010)\, W^4$$

$$x_2(011) = x_1(001)\, W^0 + x_1(011)\, W^4$$

$$x_2(100) = x_1(100)\, W^0 + x_1(110)\, W^2$$

$$x_2(101) = x_1(101)\, W^0 + x_1(111)\, W^2$$

$$x_2(110) = x_1(100)\, W^0 + x_1(110)\, W^6$$

$$x_2(111) = x_1(101)\, W^0 + x_1(111)\, W^6$$

$$\begin{bmatrix} W^0 & 0 & W^0 & 0 & 0 & 0 & 0 & 0 \\ 0 & W^0 & 0 & W^0 & 0 & 0 & 0 & 0 \\ W^0 & 0 & W^4 & 0 & 0 & 0 & 0 & 0 \\ 0 & W^0 & 0 & W^4 & 0 & 0 & 0 & 0 \\ 0 & 0 & 0 & 0 & W^0 & 0 & W^2 & 0 \\ 0 & 0 & 0 & 0 & 0 & W^0 & 0 & W^2 \\ 0 & 0 & 0 & 0 & W^0 & 0 & W^6 & 0 \\ 0 & 0 & 0 & 0 & 0 & W^0 & 0 & W^6 \end{bmatrix} \begin{bmatrix} x_1(000) \\ x_1(001) \\ x_1(010) \\ x_1(011) \\ x_1(100) \\ x_1(101) \\ x_1(110) \\ x_1(111) \end{bmatrix} \qquad (2\text{-}53)$$

Reproduced with permission of the copyright owner. Further reproduction prohibited without permission.

Stage 3

$$x_3(n_0,n_1,n_2) = \sum_{k_0=0}^{1} x_2(n_0,n_1,k_0)\, W^{(4n_2+2n_1+n_0)(k_0)}$$

$$x_3(000) = x_2(000)\, W^0 + x_2(001)\, W^0$$

$$x_3(001) = x_2(000)\, W^0 + x_2(001)\, W^4$$

$$x_3(010) = x_2(010)\, W^0 + x_2(011)\, W^2$$

$$x_3(011) = x_2(010)\, W^0 + x_2(011)\, W^6$$

$$x_3(100) = x_2(100)\, W^0 + x_2(101)\, W^1$$

$$x_3(101) = x_2(100)\, W^0 + x_2(101) W^5$$

$$x_3(110) = x_2(110)\, W^0 + x_2(111)\, W^3$$

$$x_3(111) = x_2(110)\, W^0 + x_2(111)\, W^7$$

$$\begin{bmatrix} W^0 & W^0 & 0 & 0 & 0 & 0 & 0 & 0 \\ W^0 & W^4 & 0 & 0 & 0 & 0 & 0 & 0 \\ 0 & 0 & W^0 & W^2 & 0 & 0 & 0 & 0 \\ 0 & 0 & W^0 & W^6 & 0 & 0 & 0 & 0 \\ 0 & 0 & 0 & 0 & W^0 & W^1 & 0 & 0 \\ 0 & 0 & 0 & 0 & W^0 & W^5 & 0 & 0 \\ 0 & 0 & 0 & 0 & 0 & 0 & W^0 & W^3 \\ 0 & 0 & 0 & 0 & 0 & 0 & W^0 & W^7 \end{bmatrix} \quad \begin{bmatrix} x_2(000) \\ x_2(001) \\ x_2(010) \\ x_2(011) \\ x_2(100) \\ x_2(101) \\ x_2(110) \\ x_2(111) \end{bmatrix} \qquad (2\text{-}54)$$

Reproduced with permission of the copyright owner. Further reproduction prohibited without permission.

Bit-reversal

$$X(n_2,n_1,n_0) = x_3\,(n_0,n_1,n_2)$$

$$X(000) = x_3(000)$$

$$X(001) = x_3(100)$$

$$X(010) = x_3(010)$$

$$X(011) = x_3(110)$$

$$X(100) = x_3(001)$$

$$X(101) = x_3(101)$$

$$X(110) = x_3(011)$$

$$X(111) = x_3(111)$$

$$\begin{bmatrix} 1 & 0 & 0 & 0 & 0 & 0 & 0 & 0 \\ 0 & 0 & 0 & 0 & 1 & 0 & 0 & 0 \\ 0 & 0 & 1 & 0 & 0 & 0 & 0 & 0 \\ 0 & 0 & 0 & 0 & 0 & 0 & 1 & 0 \\ 0 & 1 & 0 & 0 & 0 & 0 & 0 & 0 \\ 0 & 0 & 0 & 0 & 0 & 1 & 0 & 0 \\ 0 & 0 & 0 & 1 & 0 & 0 & 0 & 0 \\ 0 & 0 & 0 & 0 & 0 & 0 & 0 & 1 \end{bmatrix} \quad \begin{bmatrix} x_3(000) \\ x_3(001) \\ x_3(010) \\ x_3(011) \\ x_3(100) \\ x_3(101) \\ x_3(110) \\ x_3(111) \end{bmatrix} \qquad (2\text{-}55)$$

Reproduced with permission of the copyright owner. Further reproduction prohibited without permission.

Inspections of the source code of a modern FFT algorithm[13] reveals the following steps,

step 1:

The Fourier transform is performed by starting with the X indices in bit-reversed order and ending up with the A indices in natural order. This order, with bit-inversion first, has the additional advantage that the orders of the W exponents are easily discernible and thus easier to program.

In the algorithm used for the FT-VCD instrument, the bit - reversal process is programmed in assembly language .

The Bit - reversal requires that, for each element of the vector, we must:

- Express the index of the element in binary formula
- Reverse the binary bits
- Convert back to decimal
- Move the value in the element into the location of the output vector whose index is specified by that new decimal number.

Reproduced with permission of the copyright owner. Further reproduction prohibited without permission.

step 2:

The array of data points of 1024, 2048, 4096. etc. data points is divided into two array of half the size. For example, an array of 8192 points is divided into two 4096 arrays.

The second part of the data, are starts at 4096 and increases to 8192.

After the process of separation, we take these separated data to represent real and imaginary FFT arrays.

step 3

In the next stage which is referred to as "Shuffle", we take the real array and feed them as odd numbered into the first half; real, and the second half imaginary.

step 4

After the shuffle is done the actual FFT algorithm will be used. The basic idea of this algorithm is to compute dual - node pairs from the input data and to find out the FT of these data in frequency domain. Since the first array has no multiplications we do it specially and then we start to compute for other passes.

Reproduced with permission of the copyright owner. Further reproduction prohibited without permission.

2.7-Apodization (weighting) functions

2.7.1- Definition:

The term "***Apodization***" derives from the Greek expression meaning "***take off the feet***" . In the discussion of the DFT, we illustrated that in order to be able to use a digital computer for calculating the Fourier transform, the data has to be sampled in discrete intervals and has to be finite, i.e., it has to be limited in a certain region.

The equations for Fourier transforms imply had the Fourier integrals need to be evaluated between $-\infty$ to $+\infty$. In reality, it is impossible to collect data for path difference $-\infty$ to $+\infty$, therefore we have to restrict the retardation to a limited value through which we obtain the best resolution. By restricting the maximum retardation of the interferogram to a certain value, say Δ cm, we effectively multiplying the complete interferogram between $\delta=-\alpha$ and $\delta=+\alpha$, by a truncation function, $D(\delta)$ which is unity between $\delta=-\Delta$ and $+\Delta$, and zero at all other points, that is,

Reproduced with permission of the copyright owner. Further reproduction prohibited without permission.

$$D(\delta)=1 \qquad \text{if} \quad -\Delta \le \delta \le +\Delta$$

$$D(\delta)=0 \qquad \text{if} \quad \delta > |\Delta| \qquad (2\text{-}56)$$

In view of the shape of this function [2,3,7,11], $D(\delta)$ is called a boxcar truncation function. Therefore the spectrum will be convoluted with $D(\delta)$ as follows:

$$B(\upsilon)= \int_{-\infty}^{+\infty} I(\delta)\, D(\delta) \cos 2\pi\nu\delta \, d\delta \qquad (2\text{-}67)$$

It can be shown that the Fourier transform (FT) of the product of two functions is the convolution of the FT of each function.

The result of multiplying the collected interferogram $I(\delta)$, with the boxcar function $D(\delta)$ yields a spectrum that is a convolution of the FT of $I(\delta)$, $B(\nu)$, with the FT of $D(\delta)$, $f(\nu)$

$$FT(D(\delta)) = f(\nu) = \frac{2\Delta \sin(2\pi\nu\Delta)}{2\pi\upsilon\Delta} \qquad (2\text{-}58)$$

$$\equiv 2\Delta \mathrm{sinc} 2\pi\nu\Delta$$

This function is shown in Figure 2-11. When a spectrum is measured dispersively on a monochromator, the true spectrum is convolved with the slit function of the monochromator [7]. The situation with a FTIR spectrometry is similar, except that the true

Reproduced with permission of the copyright owner. Further reproduction prohibited without permission.

spectrum is convolved with the sinc function $f(\nu)$. Since the FTIR spectrometer does not have any slits, $f(\nu)$ has been called the instrument line shape (ILS) function [7].

The boxcar function is not a particularly useful line shape for infrared spectrometry in view of its fairly large amplitude well away from the line center; i.e., it has sidelobes (feet) that diminishes inversely with distance from the line center.

The existence of the sidelobes is related to the idea of "Gibbs phenomena" in Fourier series, or to the approximation of the calculated spectrum to the real spectrum. Because the window is finite ($-\Delta$ to $+\Delta$) and because the instrument line function is abrupt, i.e., a boxcar, one sees the phenomenon of sidelobes in the spectra. These side lobes are responsible for additional frequency components that occur after frequency-domain sampling. Apodization is the technique used to reduce those sidelobes. The technique consists of weighting the interferogram by a function that monotonically and continuously reduces the value of the interferogram so that it reaches zero at its maximum domain L [2,3,4,9,10].

Reproduced with permission of the copyright owner. Further reproduction prohibited without permission.

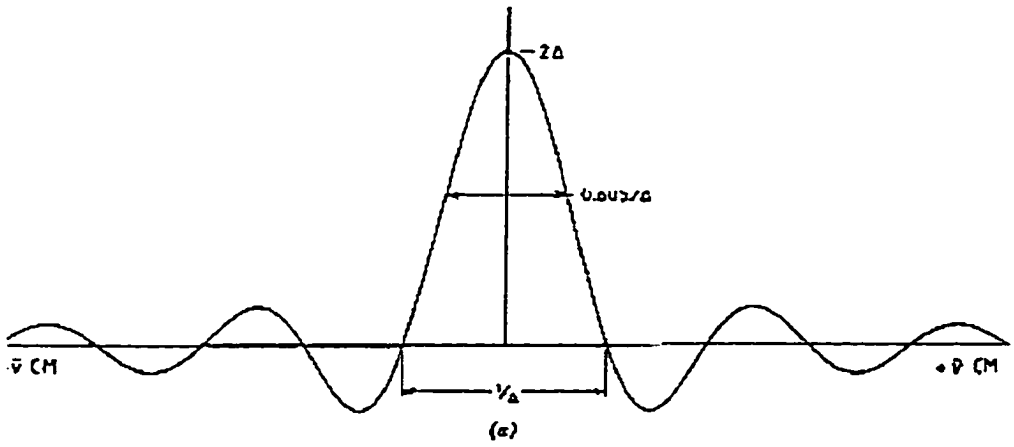

Figure2-11: *Fourier transform of a boxcar function of unit amplitude extending from -Δ to -Δ. Adapted from ref.[7]*

Reproduced with permission of the copyright owner. Further reproduction prohibited without permission.

2.7.2- FFT Data-weighting (apodization) functions

From the discussion above, we see that when a cosine wave interferogram is unweighted, the shape of the spectral line is the convolution of the true spectrum and a sinc function. This convolution, as its mentioned above, introduces additional frequency - domain components because of the side lobe characteristics of the sinc x function. These additional components are termed leakage. This terminology arises because the original frequency impulse function has leaked through the sidelobes of the sinc x function.

To reduce leakage, it is necessary to employ a time-domain truncation (apodization) function that has frequency-domain side lobe characteristics that are of smaller magnitude than those of the sinc x function. The smaller the sidelobes, the less the leakage affects the results of the FFT. These functions are applied to the N - point sampled function before the FFT is computed.

Several popular truncation or apodization functions that have been employed with the FFT are shown in Figure 2-12. For example, the simple triangular apodization function of the form

Reproduced with permission of the copyright owner. Further reproduction prohibited without permission.

$$A(\delta)=1-\left|\frac{\delta}{\Delta}\right| \qquad \text{for } -\Delta\leq\delta\leq\Delta$$

$$A(\delta)=0 \qquad \text{for } \delta>|-\Delta| \tag{2-59}$$

is used instead the boxcar function.

The true spectrum is then convolved with the Fourier transform of A(δ) and this function would therefore determine the ILS [2,7,9]. The Fourier transform of A(δ) has the form

$$f(\nu)=\Delta\frac{\sin^2(\pi\nu\Delta)}{(\pi\nu\Delta)^2} \equiv \Delta\ \mathrm{sinc}^2\ (\pi\nu\Delta) \tag{2-60}$$

This function is shown in Figure 2-13. It can be seen that the amplitude of the side lobes has been considerably reduced from the example before. This function A(δ) is called a ***triangular*** function and is the most common apodization function used in infrared FT spectroscopy.

The other popular apodization function is Hanning (or raised cosine) function [2,7,11]:

$$A(\delta) = 1/2[1+\cos(\frac{\pi\delta}{\Delta})]$$

Reproduced with permission of the copyright owner. Further reproduction prohibited without permission.

$$|\delta| \le \frac{\Delta}{2} \quad = 0 \qquad\qquad |\delta| > \frac{\Delta}{2} \tag{2-61}$$

$$A(f) = \frac{\Delta}{2} \frac{\sin(\pi f \Delta)}{\pi f \Delta [1 - (f\Delta)^2]}$$

which gives the highest reduction in the side lobe intensities, but has the advantage of much easier computation.

Reproduced with permission of the copyright owner. Further reproduction prohibited without permission.

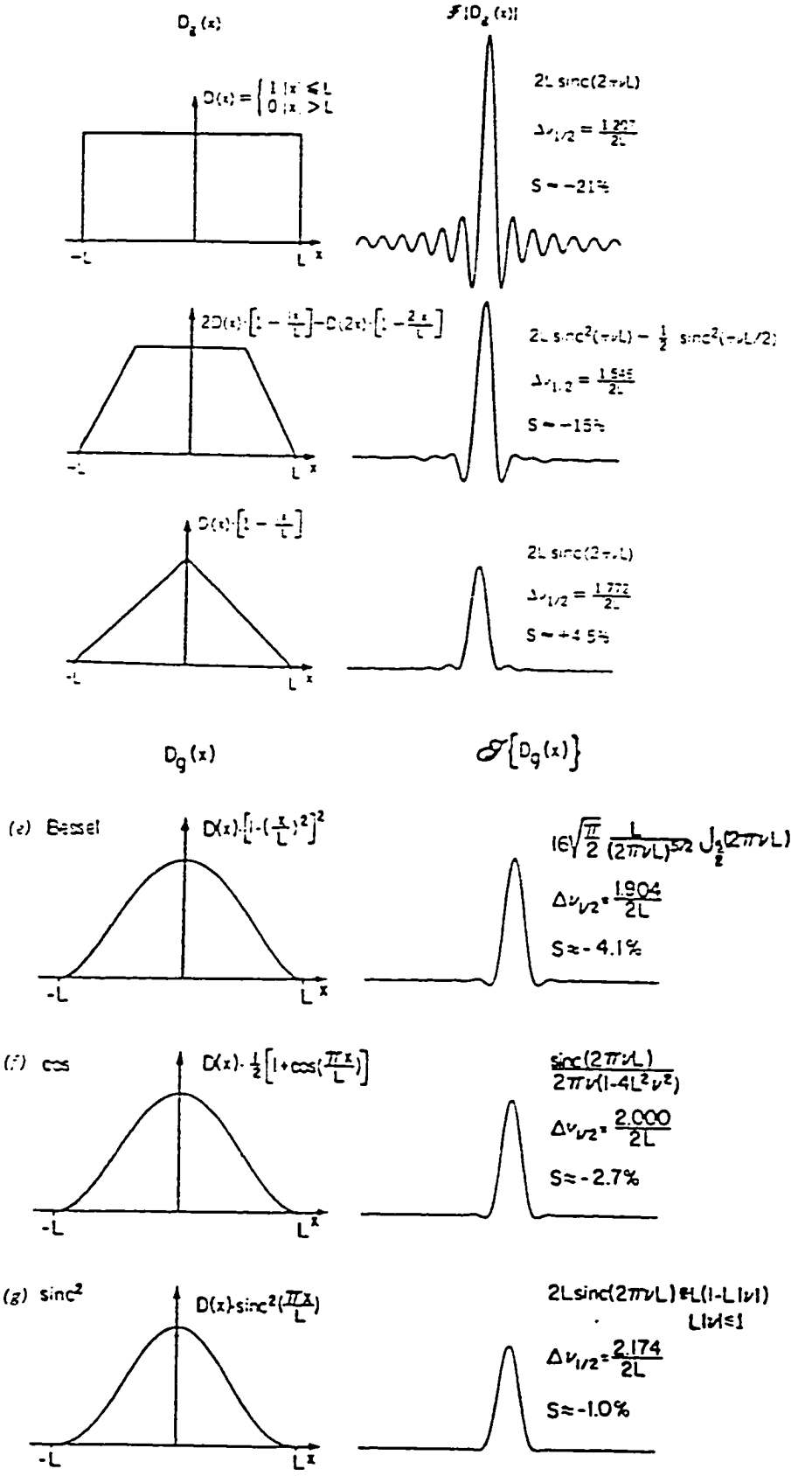

Figure2-12: *Popular apodization functions. Adapted from ref.[11]*

Reproduced with permission of the copyright owner. Further reproduction prohibited without permission.

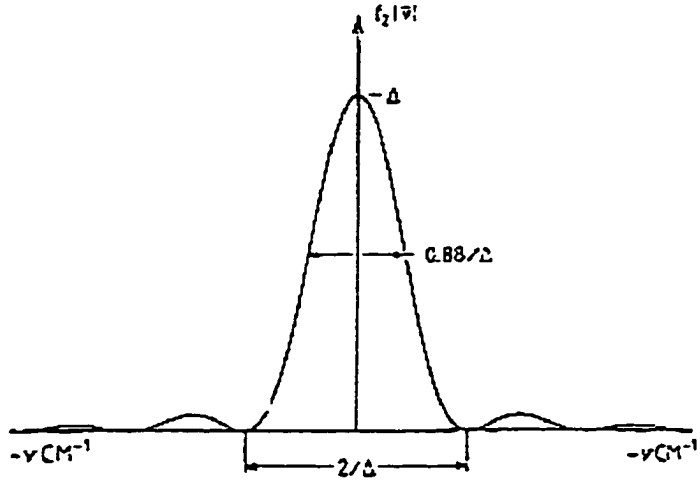

Figure 2-13: *The sinc² instrument line shape function. Adapted from ref.[7].*

Reproduced with permission of the copyright owner. Further reproduction prohibited without permission.

2.8- Zero Filling

If a spectrum has been sampled for which the number of points is not an exact power of 2, a string of zeros is appended in order to bring the total number to the next larger power of 2. This process is known as ***zero filling*** [2,5,6,12] . There is a second reason why zeros are sometimes appended, and that is to produce a better representation of the spectrum after FFT.

If x data are taken originally one may add an additional x data points, which are all set to zero. For example, if 8k zeros are added to 8k data points one can now execute a 16k transform that results in 8k real (absorption) and 8k imaginary (dispersion) data points in the frequency domain. Thus, zero filling has the advantage of doubling the number of data points. It also has distinct advantage of increasing the resolution by a factor of two. It has been argued that this is not possible since adding zeros does not add new information and consequently cannot improve the resolution, but improves the spectral. This point of view, however, is somewhat extreme; it could be reasoned that the Fourier transform itself adds no new information. This in fact is

Reproduced with permission of the copyright owner. Further reproduction prohibited without permission.

true since all the information is contained in the time domain, but not in a very usable form. Adding zeros does not add new information but it does allow one to make full use of the information contained in the time domain signal. As a result of Fourier transformation, half of the resolution information contained in the signal is lost; adding the additional zeros allows one to regain this lost information.

Griffiths [12] indicates that digitally recorded spectra containing lines of width less than, or equal to, the resolution at which the measurements has been made, are observed to show some photometric errors. These errors originate from the fact that the computed spectrum is described by a rather limited number of independent data points. To double the number of independent data points per unit frequency interval, the length of the interferogram must be doubled, thereby not only increasing the data collection time by a factor of two but also increasing the noise level in the spectrum by a factor of $\sqrt{2}$. A more reliable way of increasing the photometric accuracy is to increase the number of interpolated output points by adding N or 3N zeros to

Reproduced with permission of the copyright owner. Further reproduction prohibited without permission.

the original N point input data array. In this way the measurement time is not increased, but the computation time is effectively doubled or quadruped.

When the spectrum is computed in this fashion using triangular apodization, an apparent increase in resolution is seen along with some small artifacts on the baseline of the spectrum. To eliminate these artifacts, the interferogram has to be correctly apodized before the transform, i.e., to compute a spectrum from a zero - filled interferogram so that it has the same resolution and ILS as the spectrum computed from a triangularly apodized non-zero-filled interferogram, one should multiply the zero filled interferogram with the type of apodization function shown in Figure 2-14. In this case the resolution of resultant spectrum becomes identical with that of the spectrum computed without zero-filling, but since more data points are calculated, a much smoother spectrum, and one with higher photometric accuracy results.

Reproduced with permission of the copyright owner. Further reproduction prohibited without permission.

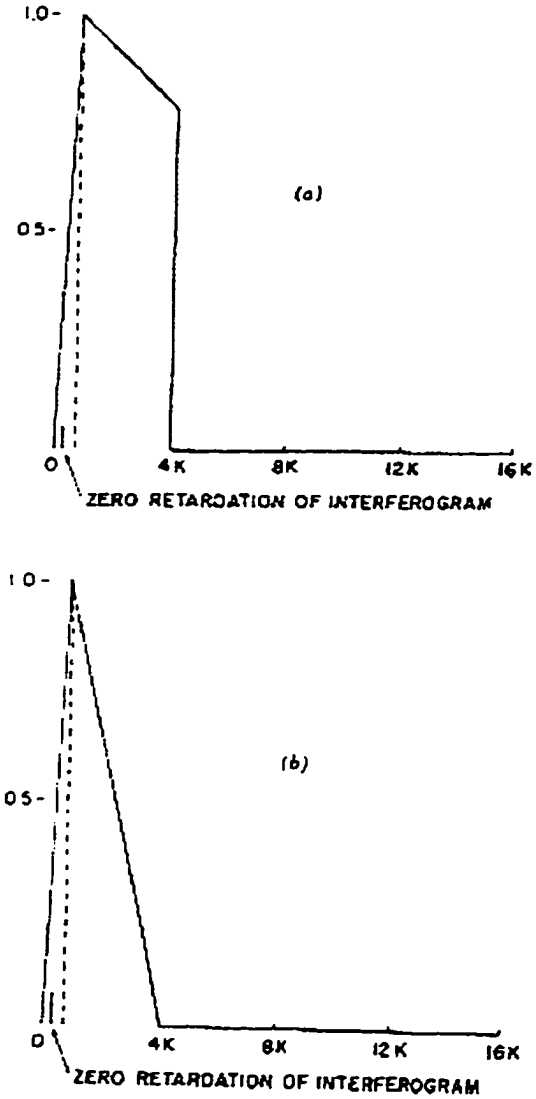

Figure 2-14: *Apodization function, triangular, for an interferogram with zero filling. Adapted from ref. [12]*

Reproduced with permission of the copyright owner. Further reproduction prohibited without permission.

2.9- Phase Correction

The presence of inherent asymmetry in the interferogram and displacement in the sampling are equivalent to a wavenumber dependent phase error $\phi(\bar{\nu})$ in the observed interferogram. This phase error is introduced due to several sources; optical, electronic, sampling effects, etc.. . The ideal way, is to eliminate these errors physically in the interferometer itself. In practice, this may be extremely difficult. Therefore the next possibility of removing the cause is to use some corrections in the software. Several authors have proposed ways in which a phase error may be corrected [7,13]. The unsymmetrical interferogram as a result of phase error can, be written:

$$I(\delta)=\int_0^{\infty} B(\bar{\nu})\cos(2\pi\bar{\nu}\delta-\theta_{\bar{\nu}})d\bar{\nu} \qquad (2\text{-}62)$$

Since the interferogram obtained is not symmetric, a complex FFT must be used to obtain the spectrum $B(\bar{\nu})$

$$B(\bar{\nu}) = \int_{-\infty}^{+\infty} I(\delta)e^{-i2\pi\nu\delta}d\delta \qquad (2\text{-}63)$$

Reproduced with permission of the copyright owner. Further reproduction prohibited without permission.

After transformation , $B(\bar{\nu})$ is calculated by the complex addition

$$B'(\bar{\nu}) = \mathrm{Re}(\bar{\nu}) + i\,\mathrm{Im}(\bar{\nu}) \qquad (2\text{-}64)$$

where $\mathrm{Re}(\bar{\nu})$ and $\mathrm{Im}(\bar{\nu})$ are the real and imaginary parts of $B(\bar{\nu})$. The phase $\phi(\bar{\nu})$ of each FFT output can be computed as

$$\phi(\bar{\nu}) = \tan^{-1}\frac{\mathrm{Im}(\bar{\nu})}{\mathrm{Re}(\bar{\nu})} \qquad (2\text{-}65)$$

This phase angle is a slowly varying function with wavenumber; therefore, $\phi(\bar{\nu})$ does not need to be measured to a high resolution. The phase angle can be adequately calculated from a short, symmetrically sampled interferogram and subsequently applied to a much higher resolution spectrum. Of course, when this is done, the phase angle spectrum must be interpolated to the same resolution as the amplitude spectrum from the whole interferogram. This method of phase correction was first developed by Mertz [7] method are described somewhere else [7,13].

The Mertz method assumes that only positive intensities are present in the experiment and that, as a result, the position of zero phase retardation for all Fourier frequencies can be determined by

Reproduced with permission of the copyright owner. Further reproduction prohibited without permission.

locating the point of maximum intensity in the interferogram. For the FT-VCD measurement, however, the form of the VCD interferogram prevents this procedure of phase correction. This is, because of the VCD intensities can be both positive and negative, and the centerburst may not coincide with maximum point of the interferogram. de Haseth et.al., [14] developed a method to solve this problem, in which they stated that it is possible to calculate the centerburst position by the symmetrical displacement of the two dichroic bursts. The centerburst position is simply the midpoint between the two bursts. In positions of the negative peaks were positive peaks, each identical in shape to the negative peaks but reflected 180° about the zero axis. Nafie [15] has suggested that the solution of this problem is to transfer the entire phase correction (zero point and wavelength dependence) from another spectrum, such as an appropriate calibration spectrum measured under conditions identical to the desired difference spectrum and where the calibration spectrum contains only positive or negative intensities. If such a monosignate

Reproduced with permission of the copyright owner. Further reproduction prohibited without permission.

calibration interferogram is not available, then the transmission interferogram of the sample may be used to obtain a close approximation to the true phase correction. The only errors introduced by using the transmission phase correction are due to phase shifts that occur in the high frequency modulation filter and the lock-in.

Reproduced with permission of the copyright owner. Further reproduction prohibited without permission.

References:

1- W. Cooper (1981), " *Introduction to Pascal for Scientists*", John Wiley & sons, New York.

2- E. O. Brigham (1988) *"The fast Fourier transform and its applications"* , Prentice Hall, Englewood Cliffs, New Jersey.

3- N. Morrison (1994) " *Introduction to Fourier analysis*" John Wiley & sons, New York

4- J. W. Cooley, P. A. Lewis and P. D. Welch (1967) *"IEEE transactions on Audio and electroacoustics"* Au-15(2), 79.

5- P. C. Kelly and G. Horlick (1973) , *Analytical Chemistry*, 45(3), 518.

6- G. Horlick (1972), *Analytical Chemistry*, 44(6), 943.

7- P. R. Griffiths and J. A. de Haseth (1986) " *Fourier transform infrared spectroscopy*", John Wiley & sons, New York.

8- L. Glasser (1987), *J. of chem. Education*, 64(12), A306.

9- D. Morgan (1994), *Practical DSP modeling, techniques, and programming in C*", John Wiley & sons, New York.

Reproduced with permission of the copyright owner. Further reproduction prohibited without permission.

10- C. Ray Wylie, L. C. Barrett (1995) " *Advanced Engineering Mathematics* ", McGraw-Hill, Inc., New York.

11- J. K. Kauppinen, D. J. Moffatt (1981), *Appl. Spectrosc.*

12- P. R. Griffiths (1975), *Appl. Spectrosc.*, 29, 11.

13- J. Chamberlain (1979), " *The Principles of interferometric spectroscopy* ", JOHN WILEY & SONS , New York.

14- A. C. McCoy and J. A. de Haseth (1988), *Applied Spectrosc.*, 42, 336.

15- L. A. Nafie (1988), " *Polarization modulation FTIR spectroscopy* " , JOHN WILEY & SONS , New York.

Reproduced with permission of the copyright owner. Further reproduction prohibited without permission.

Chapter three

Instrumentation for the observation of vibrational circular dichroism

3.1- Introduction

Infrared circular dichroism, also known as vibrational circular dichroism (VCD), was first reported nearly simultaneously by Stephens and coworkers in 1975 [1], and Holzwarth and coworkers in 1974 [2]. These first experimentally verifications in the 3 μm spectral region were the culmination of ongoing efforts to observe this elusive effect that had been predicted to exist on theoretical grounds. The theoretical predictions also anticipated an enormous increase in the stereochemical sensitivity of VCD over conventional circular dichroism, observed in electronic transitions in ultraviolet spectral region. UV-CD, or ECD, was found in the late sixties to be a valuable tool in the determination of the solution conformation of biological molecules such as peptides and proteins [3] and nucleic acids [4]. However, early

Reproduced with permission of the copyright owner. Further reproduction prohibited without permission.

theorist in VCD had argued that the higher resolution of infrared spectra, coupled with well-established sensitivity of infrared spectroscopy toward molecular structure, should make VCD a very desirable tool for conformational studies of biomolecules. However, it was not until the mid 1980's that VCD results of a large number of these molecules were reported in the literature [5], and even now, in the mid 1990's, the number of research groups involved in experimental VCD studies is small. Even worse, there are only very few research groups worldwide were instruments are available that routinely can detect the VCD of biomolecules from dilute aqueous solutions, and without requiring enantiomeric or racemic samples to construct a baseline. Therefore, the growth in VCD and its general acceptance has been slow, although its conformational and structural sensitivity is far superior to that ECD, and rival that of modern NMR techniques in some cases.

The slow growth and acceptance of VCD is attributed to the fact that at the time this research was started, no successful commercial instrument existed. Researchers most interested in

Reproduced with permission of the copyright owner. Further reproduction prohibited without permission.

VCD are generally biophysicists and structural biochemists; researchers who possess VCD instruments are physical chemists with strong background in instrument development, or theoretical interests. Nicolet, Inc. introduced a Fourier transform FT-VCD instrument in the early 1980's, which consistent of their standard FT-IR spectrometer to which the necessary hard and software was added to perform VCD measurements. A similar approach was later taken by Digilab/Biorad. Although these instruments work reasonably well for chiral organic molecules, virtually all biologically oriented VCD results in the literature were recorded on dispersive instruments in the laboratories of Keiderling at the University of Illinois at Chicago, or by Diem's group at the City University of New York, Hunter College.

3.2- Observation of VCD

3.2.1- Dispersive VCD

Dispersive instrumentation has been described in the literature in quite some detail [6]. The instruments at Hunter College may serve as examples for state of the art dispersive VCD, since they have been continuously updated and improved to produce a

Reproduced with permission of the copyright owner. Further reproduction prohibited without permission.

hitherto unachievable level of sensitivity. A schematic of these instruments is shown in Figure 3-1. The light of a small (12 x 1.8 mm), very hot Nernst glower, driven by about 60V AC and dissipating about 100 W, is imaged via gold coated optics into a short focal length (32 cm), large aperture Czerny-Turner monochromator (Instruments, SA) such that the image of the source can be sampled without intensity loss due to the entrance slit. This implies that the dispersion of the monochromator was selected such that at *ca.* 2 mm mechanical slit width, 6 cm^{-1} bandpass was achieved at 6 μm wavelength.

A frequency stabilized chopper, operating at 79 Hz, is placed in front of the monochromator, and an order sorting filter is placed at the exit slit. The emerging radiation is partially polarized by the grating in the monochromator, and further polarized via a wire grid polarizer (Perkin Elmer Corporation). The polarized radiation impinges on a photoelastic modulator (PEM, Hinds International), using a ZnSe crystals, to provide the circular polarization.

Reproduced with permission of the copyright owner. Further reproduction prohibited without permission.

Samples are contained in temperature controlled infrared cells, consisting of 19 mm diameter CaF_2 or BaF_2 plates with Teflon spacers of appropriate thickness. Required sample volume are about 60 μL. Light emerging from the samples is collected by a lens, since reflective surfaces at this point in the optical path may introduce polarization artifacts.

Detection is provided by a number of differently doped MCT (HgCdTe) detectors with detectivities in the range of 3 to 9 x 10^{10} (cm $Hz^{1/2}$ / watt).

Electronically, the I_{ac} signal (the signal modulated at the PEM frequency) is demodulated by two lock-in amplifiers in tandem. The first one, operating at a time constant significantly shorter than the chopper on-off cycles, is tuned to the PEM frequency and operates at relatively low gain (~ 1000). The second amplifier is tuned to the chopper frequency; thus, it demodulates the output of the first lock-in amplifier at the chopper frequency. Its gain is adjusted under computer control such that the signal is always between 40 and 110% of the full-scale sensitivity

Reproduced with permission of the copyright owner. Further reproduction prohibited without permission.

selected. The double modulation/double demodulation system used in most dispersive VCD instruments allows for the detection

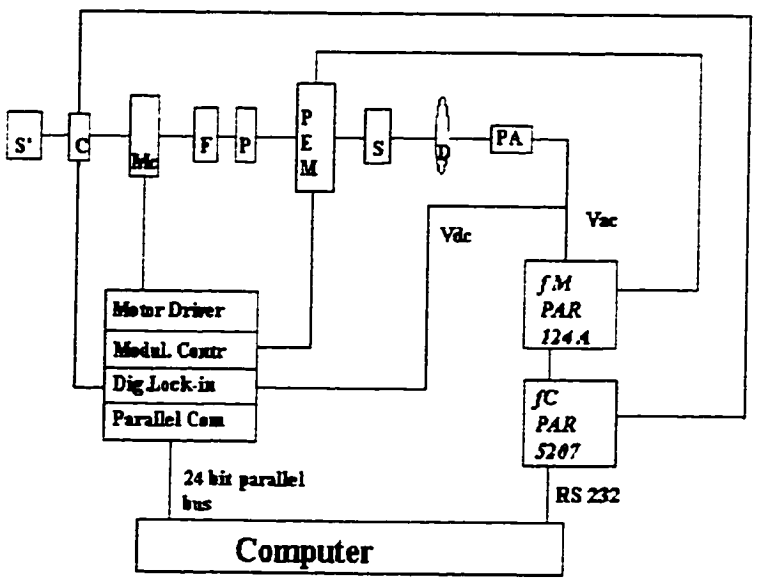

Figure 3-1: *Schematic layout of the dispersive VCD instrument*

Reproduced with permission of the copyright owner. Further reproduction prohibited without permission.

of the very small I_{ac} signal in the presence of much larger noise levels.

The instrument transmission, also referred to as I_{dc} (although it is a low frequency AC signal at the chopper frequency), is detected via digital signal processing (DSP). Instead of using an analog lock-in amplifier for measuring this signal, a chopper reference and the actual detector output are both fed into two inputs of a fast A/D board of the instrument control computer. After a positive - or negative - going transition of the reference signal is detected, data are collected every 25 μs, coadded in one of two counters, and subsequently subtracted. In this fashion, the action of a lock-in amplifier can be emulated in software at a fraction of the cost and without any external amplifiers.

Digital division of the I_{ac} signal by the instrument transmission (I_{dc}) yields the VCD signal, which is displayed in real-time during data acquisition.

The PEM retardation level is coupled, via software, to the wavelength of the monochromator during a scan, such that at

Reproduced with permission of the copyright owner. Further reproduction prohibited without permission.

every spectral point, perfect modulation conditions are maintained.

Figure 3-2 shows theoretical wave forms of the signal that occur at the detector in this kind of a dispersive VCD instrument. For a real VCD measurement, I_{ac} is too small to be observed, but for the calibration setup (utilizing a birefringent plate and a second polarizer [6]), these signals may be observed via an oscilloscope.

Reproduced with permission of the copyright owner. Further reproduction prohibited without permission.

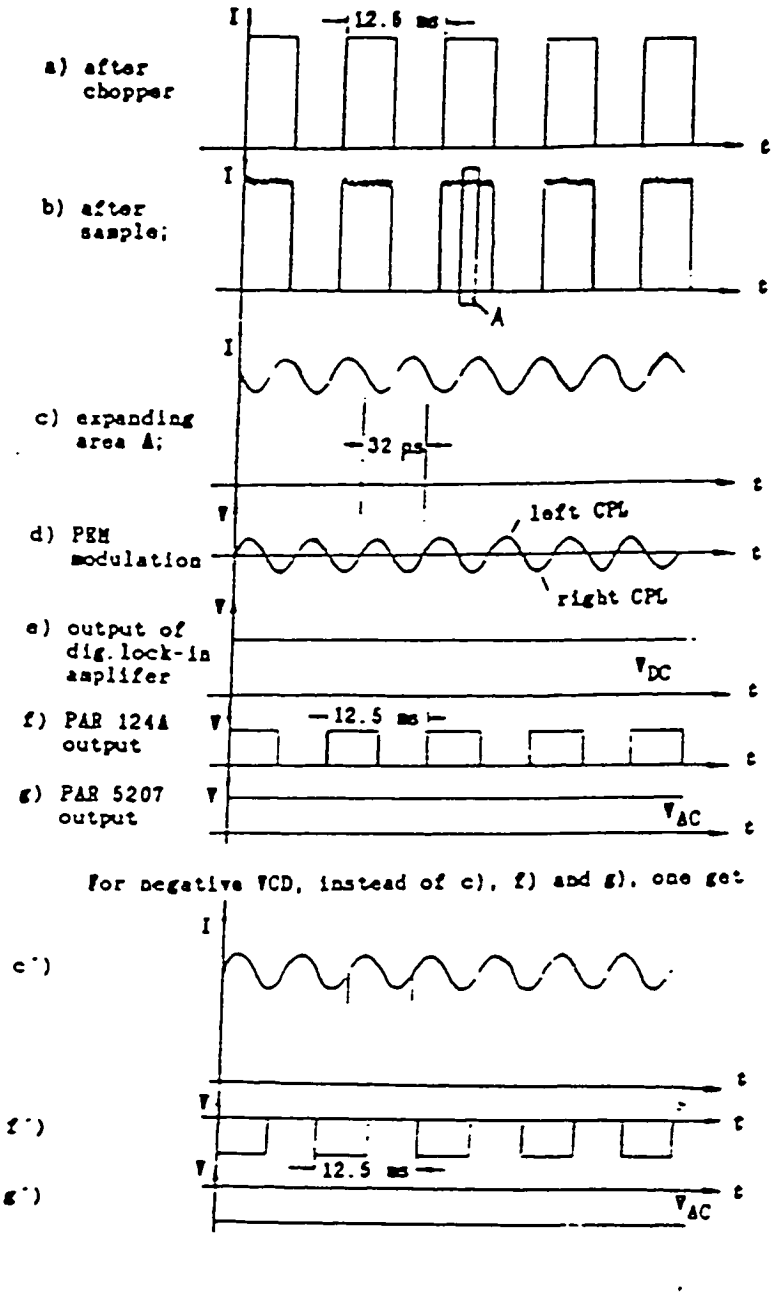

Figure 3-2: Wave forms of VCD signal. Adapted from ref. [10]

Reproduced with permission of the copyright owner. Further reproduction prohibited without permission.

3.2.2- FT VCD - Introduction

The VCD measurement can be carried out in two ways: using dispersive instrumentations, including a monochromator, and Fourier transform methodology where an infrared interferometer is used. In FTVCD, two different approaches can be followed depending on the way of producing the polarization modulation, but both of them use interferometers. To measure VCD in the first class, the signal is modulated twice, first in the interferometer to create the Fourier frequencies and second using a PEM at its resonance frequency. The detector signal is first sent to a lock-in-amplifier to demodulate the high frequency polarization modulation. The output of the lock-in amplifier is a VCD interferogram which is Fourier transformed in much the same way as the ordinary transmission interferogram. If the detector signal bypasses the lock-in and is Fourier transformed directly, the ordinary transmission is obtained. Since there are two interferograms generated simultaneously by the instrument, this general approach to the measurement of FT-VCD is a *double modulation measurement*.

Reproduced with permission of the copyright owner. Further reproduction prohibited without permission.

The second class of FT-VCD instrument is also based on the use of a interferometer. In this approach, the modulation of the polarization is generated in the interferometer itself by substituting a polarizing wire-grid beamsplitter for an ordinary dielectric one. In such an FT-VCD spectrometer, the radiation at various wavelengths is polarization modulated through successive complete 360 degree cycles. This approach to VCD measurement, is known as *polarization modulation interferometry* (PMI). The unique aspect of the PMI-FTVCD instrument is that there is no photoelastic modulator. In the paragraphs below, a background and recent developments of these types of FTVCD instruments will be discussed.

3.2.2.1- Original FTVCD (rapid-scan)

The first approach to design and build an FT-VCD instrument was reported by Nafie and Diem in 1979 [7]. In this instrument, data were collected on standard FTIR instrumentation (Nicolet 7199 FTIR) to which polarization modulation optics (BaF_2 wire grid polarizer and ZnSe photoelastic modulator) and phase sensitive detector electronics (lock-in amplifier) were added, to

Reproduced with permission of the copyright owner. Further reproduction prohibited without permission.

obtain VCD spectra using double modulation technique (DM-FT-VCD). Following this design, there have been many attempts to build FT-VCD instruments.

All DM-FT-VCD instruments reported were based in theory and principle on the original FT-VCD developed by Nafie and Diem in 1979.

a- Double modulation instruments

These instruments used continuous mirror motion (rapid-scan interferometer) using the standard FTIR instruments (Nicolet, Digilab/Biorad, BOMEM, etc.) and non-simultaneous acquisition of the I_{ac} and the transmission data. Since transmission and VCD were collected consecutively and since the I_{ac} spectrum is very weak and devoid of a centerburst, the position of the centerburst, and the phase spectrum of the transmission spectrum are used to Fourier transform the I_{ac} data. After the separate transmission, I_{ac} is obtained by FFT of the A.C. interferogram, and subsequently divided by the I_{dc} to obtain the VCD data.

The main idea behind the design and construction of the original FT-VCD instrument was to use well documented

Reproduced with permission of the copyright owner. Further reproduction prohibited without permission.

advantages of interferometric over dispersive methodology [8]. These advantages are:

1. The Fellgett Advantage

This represents the fundamental advantage over the dispersive instrument, in that the information from all frequencies of the spectrum is gathered simultaneously. An interferogram can be measured in the time it takes to measure one resolution element by a dispersive spectrometer with the same source, detector, and optical throughput. Thus, the time taken to measure the complete spectrum decreases over that for the same spectrum using a monochromator by a factor equal to the number of resolution elements N. For the same measurement time, the signal-to-noise ratio of a spectrum measured interferometrically, therefore, shows an improvement over that measurement using a dispersive spectrometer with the same source, detector, and throughput by a factor of $\sqrt{N}$.

2. The Jacquinot Advantage

This advantage represents the improvement in the optical throughput that is possible using an interferometer. The frequency

Reproduced with permission of the copyright owner. Further reproduction prohibited without permission.

component at ν with bandwidth $\Delta\nu$ reaching the detector of a dispersive spectrometer has passed through the entrance and exit slits of the monochromator. However, there is no such an intensity -reducing obstruction in an interferometer.

3. The Connes Advantage

Most modern interferometers use a He-Ne laser to reference the position of the moving mirror in the interferometer. While this gives no advantage in signal-to-noise ratio over dispersive spectrometers, it does give a large advantage in frequency accuracy.

In addition, interferometry provides for

very large resolution power and,

vastly reduced stray light levels.

It was hoped that FT-VCD would bring the same advantages over dispersive VCD. Accordingly there have been many affords to build FT-VCD instruments [5,9]. Unfortunately, in the early stages, few of the above advantages carried over to FT-VCD due to a variety of technical limitations [10] :

Reproduced with permission of the copyright owner. Further reproduction prohibited without permission.

1) Because of the multiplexing nature of the FT-VCD, its not possible to adjust the PEM modulation amplitude during a scan. The PEM is designed to produce the circularly polarized light waves at one setting, i.e., one wavelength only. As a result the possibility of computer adjusting the electronics at any spectral point such that the signal can be processed under optimum conditions not possible.

2) Artifacts occurring in the baseline due to absorption by the sample and to other light loss mechanisms in the instrument. Most FT-VCD spectra measured are subject to these artifacts that were larger than the VCD signals of the samples and occurred at the same frequency and with the same band shape as did the absorption. The origin of absorption artifacts in FT-VCD experiments is not quite clear at this moment. Lipp and Nafie [11] enumerated several optical effects as the possible sources of the artifacts among them misalignments, sample/sample cell interface, optical aperture and polarization sensitivity of the detector.

Reproduced with permission of the copyright owner. Further reproduction prohibited without permission.

3) The dynamic range of several electronic components, such as the detector, the lock-in amplifier, and the analog-to-digital converter, also restrict FT-VCD from fully exercising its advantages.

This problem arises since VCD measures very small changes in absorbance (10^{-3}-10^{-6} absorbance unit) in the presence of a large signal, especially at the centerburst in the interferogram. Furthermore, the gain of the lock-in amplifier has to be set to accommodate the centerburst, which may be two orders of magnitude greater than the nearby the interference pattern in the interferogram. As a result, the sensitivity for measuring the nearby patterns must be somewhat sacrificed.

These problems, made FT-VCD less attractive and, has made dispersive VCD preferable over FT-VCD prior to the mid 1990's.

b- PMI instruments

In 1990 Nafie, et al designed and constructed an FT-VCD instrument around a BOMEM DA3 interferometer [12].This design was based on the use of a polarizing Michelson

Reproduced with permission of the copyright owner. Further reproduction prohibited without permission.

interferometer (PMI). In this approach, a polarizing grid beamsplitter is substituted for a conventional dielectric beamsplitter. The motion of the mirror introduces a phase shift between the two arms of the interferometer, resulting in full cycles of polarization modulation at the Fourier frequencies. A similar approach was reported by Polavarapu [13]

3.2.2.2- Recent developments (step-scan)

In recent years, commercial instruments using both rapid scan and step - scan interferometers have been used in wide variety of applications in time dependent and dynamic spectroscopy due to the advantages of the step-scan over the rapid-scan interferometers. These advantages will be explained in the following section. Researchers in the field of vibrational optical activity took advantage of the step-scan over the rapid scan interferometers to develop new FT-VCD instruments to overcome the problems associated with the rapid scan based FT-VCD instruments.

The first step-scan FT-VCD instrument was reported by Marcott et al [14]. Its design was based on the idea of double

Reproduced with permission of the copyright owner. Further reproduction prohibited without permission.

modulation technique, first modulating the signal by dithering the moving mirror (phase modulation) of a step - scan interferometer (Bio-Rad FTS-60A, 896 interferometer). A photoelastic modulator (PEM) was used to produce the second modulation. Before Marcott's report, we started independently and simultaneously with the idea of the designing and constructing a FT-VCD instrument based on a step scan interferometer.

While we started the design of the step - scan FT-VCD instrument, a report of a new, step-scanning FT-VCD instrument appeared by Keiderling et al [15] which demonstrated results as good as dispersive VCD, and could carry the advantages of the FTIR over to the FTVCD instruments. This instrument is build around a Bio-Rad FTS-60A FTIR interferometer, to which optical modulation components (BaF_2 wire grid polarizer and CaF_2 or ZnSe photoelastic modulator) were added.

Two different approaches have emerged to achieve step-scanning interferometry.

The Bruker IFS66/Cs uses a truly fixed mirror, and a moving mirror that is achieved by a voice coil. Depending on the wave

Reproduced with permission of the copyright owner. Further reproduction prohibited without permission.

form applied to the voice coil, rapid-scan and step-scan with mirror dithering can be achieved.

The notable difference between the Bio-Rad FTS-60A FTIR interferometer and the Bruker IFS66/CS, is the "sawtooth-type" operation of the fixed mirror to achieve the step scanning:

The step-scan operation in the Bio-Rad interferometer is achieved by a combination of the constant motion of the moving mirror and the sawtooth type motion of the fixed mirror. The moving mirror is translated very slowly, while the fixed mirror is drawn back by piezoactuators to keep the optical retardation constant. After a period of time, determined by the step-scan rate, the fixed mirror is rapidly moved forward to increase the optical retardation to a new step. This configuration allows the interferometer to settle rapidly after each step. The settling time is fast in comparison to the step rate, and hence gives a very high measurement time duty cycle.

Reproduced with permission of the copyright owner. Further reproduction prohibited without permission.

3.3- SS-FT-VCD vs. RS-FT-VCD

Although all early optical interferometers were based on the step-scan principle [16], beginning in the late 1960s increasingly powerful rapid - scan instruments replaced step-scan technology for all but a few specialized research instruments, primarily for the far-IR. In 1966 the first optoelectronically controlled step - scan interferometer was reported [17], but, perhaps because of the growing acceptance of commercial rapid - scan instruments, this did not lead to commercial development. In 1987 Manning et.al. [16] briefly described the conversion of a commercial rapid FTIR spectrometer to step-scan operation. Other efforts have also been and the utility of step - scan FTIR as a complimentary alternative to rapid-scan is gaining wide acceptance.

3.3.1- The disadvantages of the rapid scan method in dynamic spectroscopy

While the high throughput of the interferometer gives it a clear advantage over the dispersive instruments for wide wavelength range, the use of the conventional rapid - scan FTIR instrument

Reproduced with permission of the copyright owner. Further reproduction prohibited without permission.

for dynamic vibrational spectroscopy introduces a serious complication, namely, confusion of the time dependence of the signal due to the response of the sample, with the time dependence of the spectral multiplexing. This later time dependence is the result of the continuous motion of the moving mirror, which causes each wavelength to be modulated at its own Fourier frequency, $f=2\upsilon/\lambda$, where υ is the mirror velocity and λ is the wavelength of the radiation. The problem is that in order to demodulate the time-dependent response of the sample, this response must have a frequency (or frequency range) which is separated by at least an order of magnitude from the Fourier frequency range.

Currently available rapid-scan FTIR instruments, even operating at the lowest available mirror velocities, generate Fourier frequencies ranging from ~100 to 1000 Hz for the region from 400 to 4000 cm^{-1} (mid-IR). Lowering the mirror velocity by a factor of 10 is feasible and would seem useful, but, since lock-in amplification would still be unusable, the predicted S/N enhancement would be largely negated by low-frequency

Reproduced with permission of the copyright owner. Further reproduction prohibited without permission.

vibrations and $1/f$ noise, since they would be in the same as ranges the Fourier modulation frequencies.

3.3.2-Advantages of step-scan technology for dynamic spectroscopy

The central challenge of step-scan FTIR instruments is to provide accurate measurement and control of the interferometer retardation. The applicability of FTIR to dynamic vibrational spectroscopy made it the focus of interest again. This capability includes both the use of vibrational spectroscopy to monitor time-dependent phenomena and use of certain time-dependent phenomena for vibrational spectroscopic detection.

A step-scan interferometer offers the following advantages over rapid-scan units:

a- accommodates any desired modulation frequency,

b- applies that frequency at all wavelengths,

c- allows measurement with the use of a lock-in amplifier.

For step-scan operation, the position of the moving mirror must be held constant while data are being collected. The result is an interferogram, created point by point, which is otherwise

Reproduced with permission of the copyright owner. Further reproduction prohibited without permission.

equivalent to that created by collecting rapid-scanning interferograms. Thus, the step-scan operation can be applied to virtually any modulation of the ir radiation. Since the frequencies of modulation are not a function of any retardation velocity, they have no dependence on radiation wavelength. In addition, the use of a lock-in amplifier detection provides a high degree of noise rejection, analogous to the Fourier filtering effective in rapid-scan mode.

In both step-scan and rapid-scan modes, a laser interference pattern is used, to generate feedback signals to maintain constant velocity in rapid-scan, and to generate feedback signals to control the mirror position in step-scan instruments.

It could be deduced from the discussion above that the simpler, more convenient, and more broadly useful approach to the application of interferometry to dynamic spectroscopy is to move the mirror incrementally -"step-scanning"- and thus to eliminate the Fourier frequencies. Since the mirror is stationary during data collection, the spectral multiplexing is decoupled from the temporal domain, and any temporal change in detector response

Reproduced with permission of the copyright owner. Further reproduction prohibited without permission.

is related to only the dynamic properties of the sample. Modulation of any desired frequency can be applied to the radiation, either by chopper or any other suitable device [chapter 1]. In the general dynamic experiments the time resolution is limited only by the signal strength, the rise time and sensitivity of the detector, and the data acquisition electronics. If interferometry is to be used to obtain dynamic spectral information, step - scan operation offers not only conceptual and practical simplicity of experimental design, but in some cases, access to data essentially unavailable in the rapid - scan mode.

3.4- Theoretical principals of FT-VCD

In this section which follows the discussion in reference [18] the basic mathematical and operational principles necessary to describe step-scan Fourier transform VCD is described.

First we consider two infrared spectra, $I_\alpha(\tilde{\nu})$ and $I_\beta(\tilde{\nu})$, given as a function of wavenumber, $\tilde{\nu}$, where $\tilde{\nu}=1/\lambda$. Rather than measure $I_\alpha(\tilde{\nu})$ or $I_\beta(\tilde{\nu})$ separately, we modulate rapidly between these two spectra at the frequency, f_m. This procedure results in a

Reproduced with permission of the copyright owner. Further reproduction prohibited without permission.

total intensity, or photon flux, which is given as a function of time by

$$I(\tilde{\nu},t) = I_{dc}(\tilde{\nu}) + I_{ac}(\tilde{\nu})\sin 2\pi f_m t \qquad (3\text{-}1a)$$

where

$$I_{dc}(\tilde{\nu}) = 1/2\,[I_\alpha(\tilde{\nu}) + I_\beta(\tilde{\nu})] \qquad (3\text{-}1b)$$

$$I_{ac}(\tilde{\nu}) = 1/2\,[I_\alpha(\tilde{\nu}) - I_\beta(\tilde{\nu})] \qquad (3\text{-}1c)$$

The $I_{dc}(\tilde{\nu})$ is the time independent average transmission intensity, and the $I_{ac}(\tilde{\nu})$ is the differential spectrum of interest and is measured as the amplitude of the sinusoidal intensity modulation at frequency f_m. In conventional modulation spectroscopy the intensity $I_{dc}(\nu)$ is measured point by point as a function of ν, as one scans the spectrum with a dispersive element such as the grating of a monochromator, where as in FTIR it is gathered simultaneously.

Although the difference spectrum given by $I_{ac}(\tilde{\nu})$ is an adequate description, the molecular properties expressed in terms of the decadic absorbance A are used commonly.

A is defined in relation to the transmission spectra by

Reproduced with permission of the copyright owner. Further reproduction prohibited without permission.

$$I_{dc}(\bar{\nu}) = \tfrac{1}{2} I_0(\bar{\nu}) [\, 10^{-A_\alpha(\bar{\nu})} + 10^{-A_\beta(\bar{\nu})}] \qquad (3\text{-}2a)$$

$$I_{ac}(\bar{\nu}) = \tfrac{1}{2} I_0(\bar{\nu}) [\, 10^{-A_\alpha(\bar{\nu})} - 10^{-A_\beta(\bar{\nu})}] \qquad (3\text{-}2b)$$

The expressions in square brackets represent the absorptive contributions. If desired, the difference spectrum can be expressed directly, in terms of absorbance by writing

$$\Delta A_{\alpha\beta}(\bar{\nu}) = A_\alpha(\bar{\nu}) - A_\beta(\bar{\nu}) \qquad (3\text{-}3)$$

We next provide the details of how $I_{ac}(\bar{\nu})$ and $\Delta A_{\alpha\beta}(\bar{\nu})$ can be measured using FTIR interferometry. In chapter 1 we showed that the interferogram is described in terms of the path difference, δ, as

$$I_\alpha(\delta) = \int_0^\infty I_0(\bar{\nu}) \cos(2\pi \bar{\nu}) d\nu \qquad (3\text{-}4)$$

Phase modulation of the moving mirror using a sine wave with a fixed frequency and amplitude , results in an interferogram after the phase modulation:

$$I_\alpha(\delta) = \int I_0(\bar{\nu}) + I_0(\bar{\nu}) \cos 2\pi \bar{\nu} [\delta + a \cos 2\pi f_p t] \qquad (3\text{-}5)$$

when an absorbing sample is placed in the beam one needs to replace $I_0(\bar{\nu})$ with $I(\bar{\nu})$, whereupon one can write

Reproduced with permission of the copyright owner. Further reproduction prohibited without permission.

$$I(\delta) = \int_0^{\pi} [I_{dc}(\bar{\nu}) + I_{ac}(\bar{\nu}) \sin 2\pi f_m t] \cos 2\pi \bar{\nu}(\delta + a \cos 2\pi f_p t) \qquad (3\text{-}6)$$

In order to extend this formalism to circular dichroism measurement, one needs to find expressions involving the absorbance spectra of an optically active molecule with respect to left and right circularly polarized absorption. These we designate as $A_L(\bar{\nu})$ and $A_R(\bar{\nu})$. The general intensity expression which arises in the Grosjean - Legrand method [18] is given by

$$I(\bar{\nu},t) = I_{dc}(\bar{\nu}) + I_{ac}(\bar{\nu}) \sin [\alpha(\bar{\nu},t)] \qquad (3\text{-}7a)$$

where

$$I_{dc}(\bar{\nu}) = \tfrac{1}{2} I_0(\bar{\nu}) [10^{-A_{R(\bar{\nu})}} + 10^{-A_{L(\bar{\nu})}}] \qquad (3\text{-}7b)$$

$$I_{ac}(\bar{\nu}) = \tfrac{1}{2} I_0(\bar{\nu}) [10^{-A_{R(\bar{\nu})}} - 10^{-A_{L(\bar{\nu})}}] \qquad (3\text{-}7c)$$

$$\sin [\alpha(\bar{\nu},t)] = \sin [\alpha_0(\bar{\nu}) \sin (2\pi f_m t)] \qquad (3\text{-}7d)$$

Equation 3-7b and 3-7c are extensions of equations 3-1b and 3-1c . The sinusoidal factor in equation 3-7a represents the action of the modulator as it induces phase retardation in the beam and the magnitude of the intensity variation depends upon the sine of the retardation angle $\alpha(\bar{\nu},t)$. As expressed in equation 3-7d this angle varies sinusoidal as the modulator oscillates. In addition,

Reproduced with permission of the copyright owner. Further reproduction prohibited without permission.

the magnitude of retardation for a given stress in the modulator depends linearly on the wavenumber frequency, corresponding to a lower degree of retardation for lower values of $\tilde{\nu}$. The angle $\alpha_0(\tilde{\nu})$ corresponds to the maximum retardation amplitude achieved by the modulator at a given $\tilde{\nu}$ during the course of its oscillation cycle. Equation 3-7d can be further expressed in a series of odd order spherical Bessel functions as

$$\sin[\alpha_0(\tilde{\nu}) \sin \omega_m t] = 2 \sum_{n.odd} J_n [\alpha_0(\tilde{\nu})] \sin (2\pi n f_m t) \qquad (3\text{-}8)$$

We are concerned with only the first term in this summation which corresponds to the fundamental frequency of the modulator. The higher harmonics are eliminated electronically when the signal $I(\tilde{\nu},t)$ is processed by a lock-in amplifier tuned to f_m. The resulting total intensity expression which one seeks to measure in circular dichroism is given by

$$I(\tilde{\nu},t)=I_{dc}(\tilde{\nu})+I_{ac}(\tilde{\nu})2J_1[\alpha_0(\tilde{\nu})] \sin (2\pi f_m t) \qquad (3\text{-}9)$$

The factor of $2J_1[\alpha_0(\tilde{\nu})]$ accounts for the effectiveness of the modulator to produce circularly polarized radiation at various wavenumbers. In order to determine the differential absorbance

Reproduced with permission of the copyright owner. Further reproduction prohibited without permission.

spectrum $\Delta A_{CD}(\bar{\nu})$. the ratio of $I_{ac}(\bar{\nu})/I_{dc}(\bar{\nu})$ is calculated. The signal from the detector therefore will be, expressed in terms of voltage:

$$V(t)= [V_{dc} + V_{ac}\, 2J_1[\alpha_0(\bar{\nu})] \sin(2\pi f_m t)]\, 2J_1(2\pi\bar{\nu}a) \sin 2\pi\bar{\nu}\delta \qquad (3\text{-}10)$$

In the FTVCD instrument at Hunter College, V_{vc} and V_{ac} are determined by demodulating them at frequencies of 400 Hz and 37 kHz respectively. They are subsequently divided to obtain the VCD signal.

Using the expressions developed in equation 3-7b and 3-7c , we can write

$$\frac{I_{ac}(\bar{\nu})}{I_{dc}(\bar{\nu})} = \frac{10^{-A_R(\bar{\nu})} - 10^{-A_L(\bar{\nu})}}{10^{-A_R(\bar{\nu})} + 10^{-A_L(\bar{\nu})}} \qquad (3\text{-}11)$$

Conversion to the natural logarithm base and multiplication of the numerator and denominator of the equation 3-11 by

$\exp\{ \tfrac{1}{2} \ln 10[A_R(\bar{\nu}) + A_L(\bar{\nu})]\}$ leads to

$$\frac{I_{ac}(\bar{\nu})}{I_{dc}(\bar{\nu})} = \tanh\{ \tfrac{1}{2} \ln 10 [-\Delta A_{RL}(\bar{\nu})]\} \qquad (3\text{-}12)$$

For small values of ΔA_{RL} , the hyperbolic tangent may be replaced by its tangent. Using the notation that $\Delta A_{RL} = -\Delta A_{LR}$ and

Reproduced with permission of the copyright owner. Further reproduction prohibited without permission.

½ ln 10 ≅1.15, we have

$$\frac{I_{ac}(\nu)}{I_{dc}(\nu)} \cong 1.15\Delta A_{RL}(\nu) \qquad (3\text{-}13)$$

Thus, we have determined the difference spectrum in terms of absorbance.

3.5- Design and Construction of the step-scan FT-VCD

3.5.1- Introduction

Vibrational circular dichroism (VCD), the differential absorption between left and right circularly polarized infrared light, is generally measured using polarization modulation methods. Measurement of the VCD has utilized dispersive [6] and Fourier transform[14,15] instrumentations. The main difference between the dispersive VCD instruments at Hunter College {VC1 and VC2 } and the FT-VCD instrument {VC3} is the use of a Michelson interferometer instead of the monochromater. The Michelson interferometer operates on the principal of amplitude splitting of the incoming light [chapter 1]. In conventional infrared spectroscopy, the FT method has several

Reproduced with permission of the copyright owner. Further reproduction prohibited without permission.

advantages over the dispersive ones. These advantages are explained in section 3.2.2.1 of this chapter.

Nafie et al. [1] proposed and later developed Fourier transform based VCD, to carry the advantages of the conventional FTIR over to VCD measurements. The original design was on the basis of a rapid-scan FTIR in which the moving mirror of the Michelson interferometer moves continuously [chapter 1]. This method had some restrictions due to a cross - talk between the high frequency modulation of the PEM frequency, and the Fourier frequency introduced from the movement of the moving mirror [chapter 1]. With availability of step-scan Fourier transform infrared instrumentation, in which the moving mirror moves incrementally step - by - step, it has become possible to explore new approach to the measurement of FT-VCD.

3.5.2- Description of main components:

In this section, the process of the design and construction of the step-scan based FT-VCD instrument {VC3} at Hunter College described in detail. Reference is made to Figure 3-3 for this discussion.

Reproduced with permission of the copyright owner. Further reproduction prohibited without permission.

1- ***Source:***

The light source utilized is a very high temperature Nernst glower, produced by Ayer Engineering, Ramona, CA. This glower, with 0.9 mm diameter and axial leads, is thermally much less sensitive than the source utilized in VC1 and VC2 at Hunter College and can be preheated to its ignition temperature via a cigarette lighter or a small propane torch. It is operated from a regulated AC voltage source, and dissipates about 100W.

2- ***Interferometer:***

The IFS66/CS interferometer is a Michelson interferometer with a fixed and a movable mirror and a KBr beamsplitter. It provides resolution of better than 0.1 cm^{-1} and in the near, mid and far infrared regions. The angle of incidence of the infrared radiation onto the exchangeable KBr beamsplitter is 45^0, insuring highest efficiency, high throughput and reduced effect of polarization.

The fixed mirror of the interferometer has three degrees of adjustments. Two of them use two stepping motors (A and B) to tilt the mirror in the x and y directions. These two motors can be

Reproduced with permission of the copyright owner. Further reproduction prohibited without permission.

controlled both manually and automatically using the Bruker IFS66/CS commands and software written in our laboratory. The third adjustment is done manually by a screw to move the mirror back and forth in the z direction.

The interferometer has the capability to work both in rapid-scan and in step scan modes. In rapid scan mode, the mirror moves continuously at different velocities (0.05 cm/s - 5.06 cm/s). In step-scan mode, however it moves incrementally from one step to another with a minimum step size of 0.316 μm and a settling time of 20 μsec. The moving mirror is moved by an electromagnetic transducer similar to the voice coil of a loudspeaker. A slowly increasing current is applied to the coil to drive the mirror at a constant velocity in rapid-scan mode, and a step-wise voltage approximately (0.89 mA, 11.6 Ω) is applied in step-scan mode to move the mirror from one step to another. The mirror is driven on an air bearing mounted on the center of mass of the scanning mirror carriage. Approximately 150 *l*/h, 26 PSI regulated air is required for the air bearing. The mirror can be dithered for phase modulation by applying a sine wave from a wave generator at a

Reproduced with permission of the copyright owner. Further reproduction prohibited without permission.

frequency up to 1KHz and an amplitude depending on the sampling condition.

A He-Ne laser located outside the interferometer compartment is used to create a feedback signal to control the voltage supplied to the voice coil in order to collect the data accurately [chapter 1]. The intensity of the laser signal is detected by a photodiode detector located on the laser tube. The output of this detector is read using the connections located at the interferometer board or the laser board via an oscilloscope.

The interferometer is interfaced to the external laboratory computer via the interferometer board, laser board, stop-and-go board, motor control board, and the CPU board. It is controlled using Bruker IFS66/CS commands and the software written in our laboratory.

3- ***Photoelastic modulator (PEM):***

A PEM consists of a uniaxial piece of material which is transparent in the spectral range of interest and is aligned with its unique axis (the z axis) along the propagation direction of the light. Under the influence of a mechanical stress or strain, and

Reproduced with permission of the copyright owner. Further reproduction prohibited without permission.

along the crystal's x or y axes, the refractive indices along these axes, n_x and n_y become unequal, causing light waves polarized along the x and y direction to travel with different velocities through the crystal. At the exit face of the crystal, circularly polarized light is produced if the retardation between the two orthogonal components of the light is a quarter wavelength. The strain/stress is commonly produced by utilizing a modulator bar consisting of two piezoelectric crystals between which the transmitting crystal is cemented. If the resonance frequencies of all three are matched, self-oscillation of the modulator bar can be achieved. In this case, an AC voltage of the appropriate frequency and amplitude is applied to the piezoelectric crystals; the entire modulator bar will then act as a frequency stabilizing feedback device. The amplitude of the AC voltage determines the stress/strain and therewith, the retardation. One of the major advantages of photoelastic modulators is the large aperture of acceptance, which makes alignment easy and allows them to be used in strongly converging or diverging beams of light. Their use, however, is restricted mostly to differential absorption

Reproduced with permission of the copyright owner. Further reproduction prohibited without permission.

measurements, where fixed frequency and sinusoidal modulation may be employed.

The PEM (Hinds International, Inc., Model PEM-90) used in VC3 instrument has a clear aperture of 35.5 mm in diameter. Its heart is a broad band antireflection-coated ZnSe crystal (transmission > 90% between 12 and 5μm). The stress axis of the PEM is 45^0 with respect to the horizontal, the direction of the linear polarizer. It modulates at 37 kHz, at which frequency it alternately produces left and right circularly polarized light.

4- ***Detector:***

A high sensitivity detector (Infrared Associates, Inc., model HCT 6-7) is used. This detector is operated in the photoconductive mode: that is the HgCdTe crystal's conductance increases when infrared radiation of the proper wavelength is incident on the active area. The change in conductance is manifested as a voltage change across the detector when passing a constant current through it. Its active element HgCdTe (0.5 mm x 0.5 mm) exhibits sensitivity of a peak about 17.45×10^9 cm $Hz^{1/2}$ /w at 1404 cm^{-1}. The detector is

Reproduced with permission of the copyright owner. Further reproduction prohibited without permission.

operated at 77K (liquid nitrogen temperature) and its spectral range is 2.0 -10μm.

3.5.3- Optical layout

3.5.3.1- phase(1)

The original design was based on double modulation methodology, accomplished by inserting a mechanical chopper in the optical path. The light from the Nernst glower [vide supra] is collected at F/4 and focused into a frequency stabilized chopper (Oriel instruments, model 75155), operating at 100 Hz, to modulate the amplitude of the signal (amplitude modulation). This step is particularly important, since the absence of Fourier frequencies due to the fixed mirror position effectively would create single frequency modulation experiment. Although the chopper reduces the light intensity by a factor of two, we believed that the double modulation (low frequency modulation using the chopper and the high frequency modulation using the PEM) is one of the key features of the VCD instruments [vide supra].

Reproduced with permission of the copyright owner. Further reproduction prohibited without permission.

The light from the chopper is collected with a CaF_2 lens and enters the Bruker IFS66/CS interferometer [vide supra] as a parallel beam, *cf.* Figure 3-3. In spite of the fact that lenses produce various aberrations, all optical elements used refractive, rather than reflective, optics to maintain a Gaussian intensity profile of the light beam. The collected light is directed into the Bruker IFS66/CS interferometer, from which it emerges as a parallel beam Figure 3-3. It is refocused at F/4, passed through the wire grid linear polarizer on a KRS-5 substrate (International Crystal Labs), and the photoelastic modulator, PEM [vide infra]. The PEM mount has the flexibility for the alignment in five directions: x, y, z, and pitch and yaw. We believe that this freedom of movement is particularly important: from our experience on VC1 and VC2 we found that most of the absorption artifacts are introduced because of the misalignment of the PEM. Therefore, we designed the mount to allow adjustment of the PEM in five directions to produce a better alignment.

Samples are mounted on a sample holder which can be temperature controlled by a circulating water bath. The polarizer,

Reproduced with permission of the copyright owner. Further reproduction prohibited without permission.

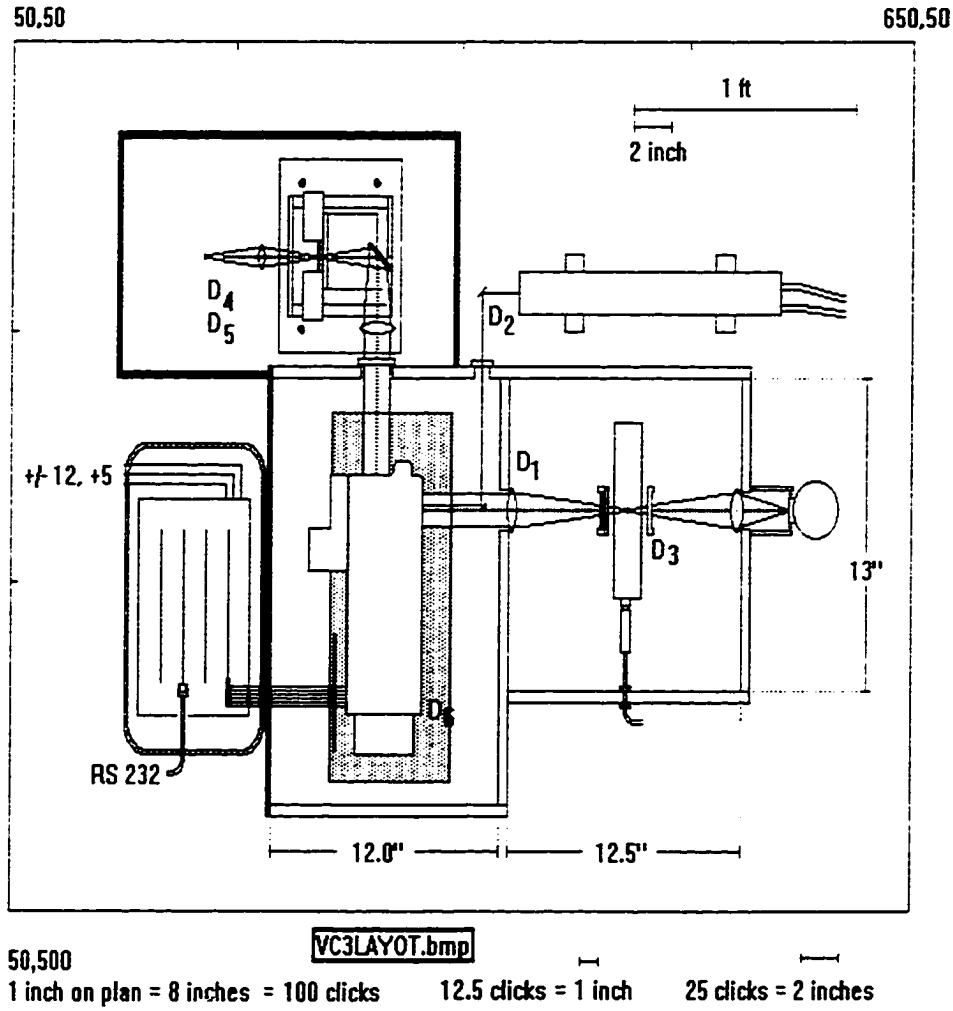

Figure 3-3: Optical layout of phase-1

Reproduced with permission of the copyright owner. Further reproduction prohibited without permission.

modulator and the sample holder are very closely together, occupying only about 6 cm along the optical path to allow light to be transmitted without vignetting. After final focusing at F/1 by a BaF_2 lens, the light is detected the 0.5 x 0.5 mm^2 HgCdTe detector.

The SS- FT- VCD instrument is build on a small (3' x 4') vibration isolated optical table (Newport corporation) tapped with ¼- 20 holes on a 1 inch grid. Compressed and dried air is available at sufficient pressure and flow rate to float the table, to provide the interferometer with air pressure for the bearing, and to purge the SS- FT- VCD instrument.

3.5.3.1.1- Results from phase-1

A typical DC interferogram from this instrument layout is shown in Figure 3-4. We find that the signal to noise ratio was very poor, and under these conditions was impossible to collect an AC interferogram. Therefore, our goal at this stage was to eliminate this noise and obtain an interferogram with a better signal to noise ratio. In order to decide the origin of this noise and to obtain a better interferogram we assumed that the noise may have

Reproduced with permission of the copyright owner. Further reproduction prohibited without permission.

three different sources: optical, ground loop, and mechanical (environmental) noise.

a- Optical artifact:

The optical artifact would mainly result from misalignment of the optics and the interferometer. Two effects dependent on the alignment of the mirrors in a Michelson interferometer can affect the quality of a spectrum. The first depends on the alignment of the fixed mirror relative to the moving mirror (see the following section ***a1*** for the alignment), and the second depends on how accurately the plane of the moving mirror is maintained during the scan. If the moving mirror is held at a different angle than the fixed mirror relative to the plane of the beamsplitter, then the image of the beam to the moving mirror will hit the plane of the detector at a different position than the beam that traveled to the fixed mirror. If the images from the fixed and moving mirrors are not centered at the same point on the detector, fringe contrast can be drastically reduced.

The interferogram is usually perfectly symmetrical when the interferometer is in good alignment; as the alignment deteriorates,

Reproduced with permission of the copyright owner. Further reproduction prohibited without permission.

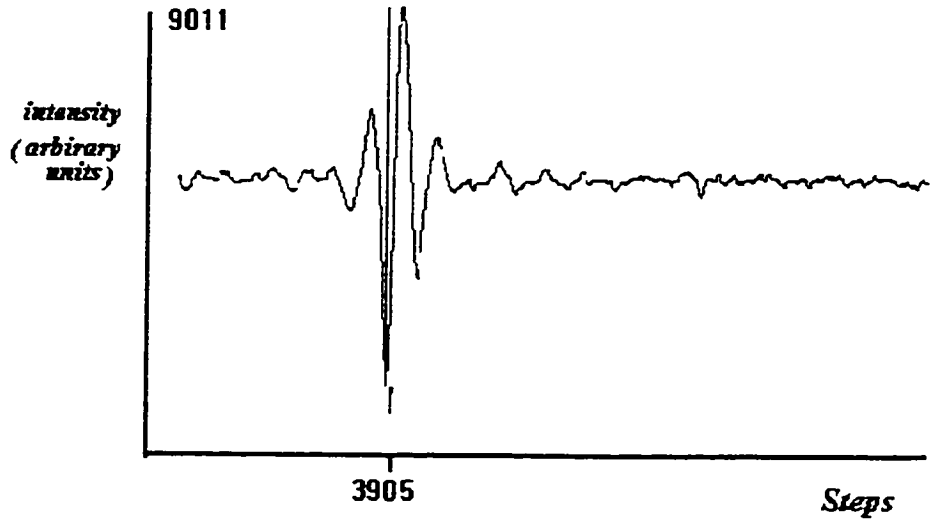

Figure 3-4: A typical interferogram obtained from the VC3-phase 1 layout.

Reproduced with permission of the copyright owner. Further reproduction prohibited without permission.

not only does the amplitude of the signal at the ZPD decrease but the interferogram also becomes asymmetrical. This behavior demonstrates that the ZPD point no longer occurs at the same path difference for all wavelengths.

Neither of these misalignments would actually contribute to the noise observed in the interferogram. However, they would reduce the amplitude of the interferogram to such an extend that other sources of noise (detector, amplifiers etc.) would become significant.

From our experience on the dispersive VCD, we found that one of the most important aspects of the instrumentation is the alignment of the optics. The procedure for the alignment of the VC1 is described in Appendix-I. A similar procedure and the procedure for the alignment of the interferometer [next section] is used to align the optics and the interferometer of VC3.

Aligning the optics did not result in a better signal to noise ratio, *cf.* Figure 3-5. Thus, we concluded that the alignment of the interferometer reasonably good.

Reproduced with permission of the copyright owner. Further reproduction prohibited without permission.

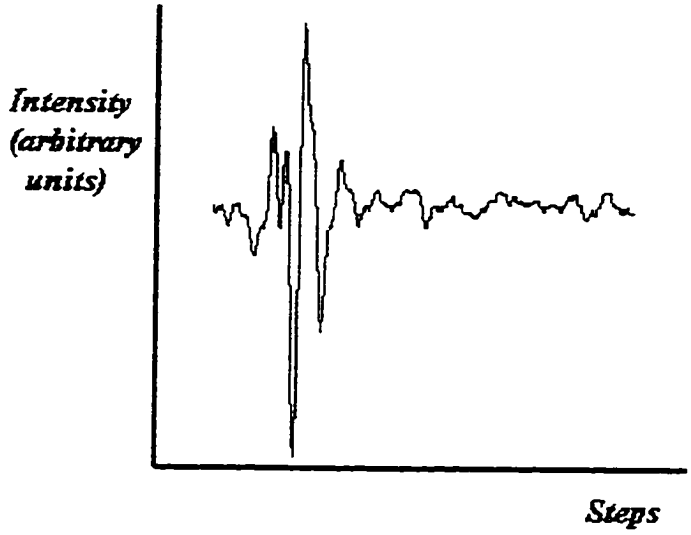

Figure 3-5: An interferogram obtained from phase 1 layout after optical alignment.

Reproduced with permission of the copyright owner. Further reproduction prohibited without permission.

a1- Alignment of the Bruker IFS66/CS interferometer

One of the fundamental aspects of the Fourier transform interferometry is finding the position of the centerburst accurately and maximizing the laser signal in order to assure the movement of the mirror and sampling the data precisely. Therefore, the first step in this design process was the alignment of the Bruker IFS66/CS interferometer.

Since the centerburst depends on the position of the fixed mirror and its distance from the beamsplitter [chapter 1], the position of the centerburst will change by changing the fixed mirror position with respect to the beamsplitter.

Thus, after alignment of the fixed mirror, or replacing the beam splitter, zero path difference (ZPD) has to be re-established. Furthermore, we found that the ZPD position in Bruker interferometer is not defined in absolute interferometer steps, but an original position defined by the starting position of the mirror motion. Thus, the centerburst moves according to an equation depending on the scan parameters selected.

Reproduced with permission of the copyright owner. Further reproduction prohibited without permission.

Accordingly, our first problem in this project was finding the centerburst. As mentioned before, the centerburst occurs whenever the retardation (δ) is zero [chapter 1]. To find this point we started the moving mirror from different arbitrary positions, defined by BRUKER IFS66/CS command SAS and SCL: These commands, define mirror absolute starting position and scan length in full laser periods, respectively.

In terms of these parameters, the ZPD position is given (in laser fringes) by:

$$\text{centerburst} = 2^* \text{SAS} + 700$$

By giving different values for SAS one can find the centerburst.

- The procedure for the alignment of the instrument using fast-scan mode via an oscilloscope.

The alignment of the interferometer is carried out in fast-scan mode, by maximizing the amplitude of the interferogram.The way to align the instrument is as follows:

Communication with the control electronics is established using the terminal emulation program of windows 3.11 to change the

Reproduced with permission of the copyright owner. Further reproduction prohibited without permission.

parameters and control the interferometer. After setting the communication parameters with the interferometer control boards, we use the Bruker IFS66/CS commands to control the interferometer and to change the parameters such as the velocity (VEL), absolute start position (SAS) , and the scan length (SCL).

1- Using the terminal emulation program of windows 3.11, we initiate the communication between the computer and the Bruker IFS66/CS interferometer. This is done by using the Bruker command VSN. After the communication is established, the maximum value for the velocity (VEL=15) and the values for the parameters SAS (e.g. SAS=3000) and SCL (e.g. SCL= 2500) will be entered.

2- The detector output, after preamlification, is directly connected to the channel-1 of the oscilloscope. The other signal is taken from the take data (TKDA) connector on the stop-and-go board to the trigger channel of the oscilloscope in order to trigger the signal from the detector.

After establishing these two steps, the interferogram will be displayed on the oscilloscope. This signal, i.e. the interferogram

Reproduced with permission of the copyright owner. Further reproduction prohibited without permission.

will be maximized by aligning the optics to obtain an optimum S/N ratio.

- Obtaining a maximum laser signal

The fringes of the laser signal are used to control the velocity of the moving mirror in the fast scan mode, and its position in step scan mode to sample the data accurately at each zero - crossing of the laser signal. Accordingly, obtaining a good and maximum laser signal is mandatory for proper results. Since the laser is a monochromatic light, therefor the output of the interferometer will have no centerburst but a symmetrical sine wave corresponding to a single frequency. This sine wave can be monitored and its amplitude measured via an oscilloscope. The output of the laser photodiode, taken from the interferometer board, is displayed directly via the oscilloscope. Subsequently, this signal is maximized by aligning the fixed mirror via stepping motors A and B.

Software was written in house to perform this experiment automatically. Here, the motors A and B will turn in small steps

Reproduced with permission of the copyright owner. Further reproduction prohibited without permission.

under the control of the computer and after each turn the laser signal output is monitored via a computer.

Using the first method however, is recommended since it will give more accurate and rapid results.

b- Grounding:

The use of proper grounding techniques is an important consideration in any system processing low-level signals. If grounding is improperly done, ground loop currents can contaminate the signal and make the measurement impossible produce noisy signals. A ground loop can result when various parts of a circuit are returned to separate ground points. Almost every measurement system contains some ground loops, that is, closed circuits formed by tying together all system grounds to bring them to the same potential.

One possible ground loop may have been produced by using a 12 V DC output from the lock-in amplifier as the DC voltage for the detector, and having both the detector and the lock-in amplifier grounded separately.

Reproduced with permission of the copyright owner. Further reproduction prohibited without permission.

In order to eliminate this source of ground loop a battery was used for detector power. The results from this experiment are shown in Figure 3-6. From this experiment, we concluded that the origin of the noise was not due to the ground loops.

Electromagnetic fields at the power line frequency and its harmonics can be found in almost every laboratory. They come from a wide variety of sources; motors, transforms, coils, AC power supplies, etc. In other words, these fields cannot be avoided. The electrical line frequency (60 Hz in the United States) often falls in the range of modulated spectral frequencies (for example, the amplitude modulation of the light using the chopper).

Shielding and grounding of all supplies and the power cabels should in principle, eliminate electromagnetic pick-up. Careful adherence for the grounding and shielding did not improve the S/N ratio either.

Reproduced with permission of the copyright owner. Further reproduction prohibited without permission.

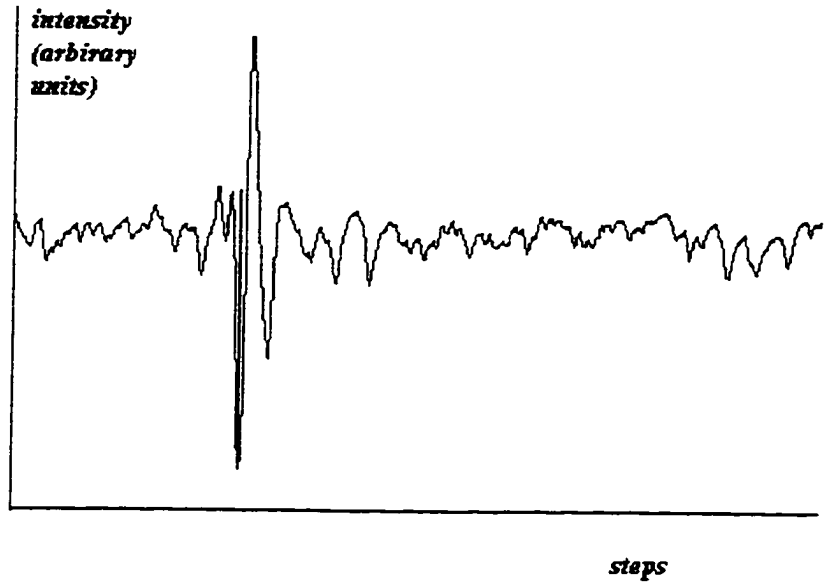

Figure 3-6: *The effect of eliminating detector power ground loop.*

Reproduced with permission of the copyright owner. Further reproduction prohibited without permission.

c- Mechanical (environmental) noise:

As mentioned above, the moving mirror in a step-scan interferometer moves nearly frictionlessly on an air bearing, and is driven by a voice coil. In step - scan mode data are collected while the moving mirror is stationary. If a vibration of frequency f is picked up throughout a scan (e.g. by poorly damped mirror vibrating at its resonant frequency), or from an acoustic signal, a spike or "glitch" will be seen at a wavenumber $\tilde{\nu}$.

In our experiments the source of this noise was not clear, therefore we tried different possibilities in order to decide the origin of this noise.

The air to the air bearing is supplied to the interferometer from a compressor via a long tubing. This long tubing may pick up some vibrations, either from the compressor itself or from the environment (sound, mechanical vibration) and may transmit it to the interferometer and thereby modulating the moving mirror which will produce a noisy interferogram. To test this possibility, we exchanged the compressor with an air tank with a shorter

Reproduced with permission of the copyright owner. Further reproduction prohibited without permission.

tubing. The results we obtained was not enhanced and still noisy, *cf.* Figure 3-7.

One source of mechanical noise we considered was the chopper. The mechanical vibration of the chopper can be transmitted through the table to the interferometer. The moving mirror is stationary during the data collection and the vibration of the chopper may move this mirror and produce a signal contaminated with noise.

The second possible source for the noise may be due to the fact that the chopper does not produce a proper square wave. The output signal from the detector was found to contain the second harmonic of the chopper modulation frequency (100 Hz). Since the Fourier analysis of a square wave is a sum of the odd harmonics, we concluded that the chopper does not produce a good square wave modulation, but instead a trapezoidal wave form. If the modulated signal is not a square wave but a trapezoidal wave, its Fourier frequencies will contain even harmonics.

Reproduced with permission of the copyright owner. Further reproduction prohibited without permission.

The noise due to the chopper vibration or to the fact that the chopper does not produce a proper square wave can be reduced by damping the vibration of the chopper. However, in this step of the project we did not proceed in this direction, since we had an alternative, the phase modulation which gives a better S/N ratio than the amplitude modulation for reasons discussed in chapter 1. In the following section we will be describing the layout and results from the phase modulation experiments.

Reproduced with permission of the copyright owner. Further reproduction prohibited without permission.

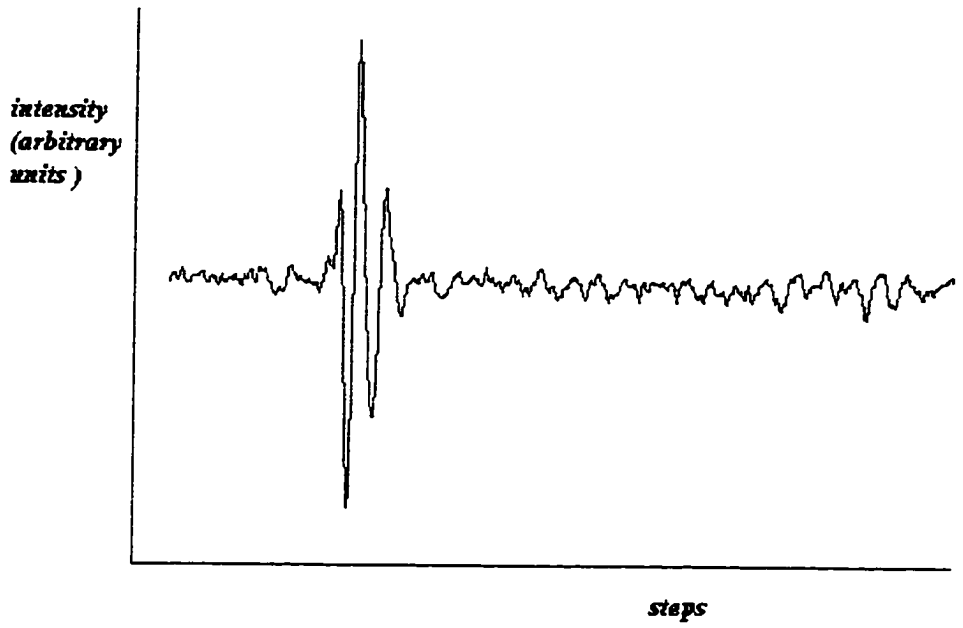

Figure 3-7: *The effect of exchange the compressor with an air tank an the shape of the interferogram.*

Reproduced with permission of the copyright owner. Further reproduction prohibited without permission.

3.5.3.2-Phase (2)

The layout of this design is shown in Figure 3-8. This layout differs from that of phase 1 by the use of phase modulation instead of the amplitude modulation.

As mentioned in chapter 1 that, in step - scan mode the moving mirror will be stationary during data collection. This, in effect will produce a DC signal; therefore we need some sort of modulation in order to convert the DC signal into an AC signal. This modulation can be generated by modulating the radiation in two ways, externally and internally. External or amplitude modulation (AM) can be provided by a mechanical chopper. This method, however introduces some noise problems (vide supra) that prevented the observation of VCD, since we need a very high signal to noise ratio. Internal (or phase) modulation provides an alternative which avoids the problems associated with the amplitude modulation. Phase modulation of the interferometer beam is provided by the "dithering" the moving mirror. This is done by applying a sine wave to the voice coil at the frequency of

Reproduced with permission of the copyright owner. Further reproduction prohibited without permission.

400 Hz and an amplitude between $\lambda/4$ to 2λ at the He-Ne wavelength .

The sine wave is provided from a wave generator. Since the lock-in amplifier used in our experiments has the capability of generating such a sine wave, we used the lock-in amplifier source of the signal for the moving mirror. The oscillator output from the lock-in amplifier is connected to the Stop- and-Go board of the interferometer electronics. The amplitude and the frequency of the oscillator is controlled via the lock-in amplifier. This amplitude of the oscillator is particularly important in the process of data collection. Since we stop the mirror and collect the data at every laser signal zero-crossing, the amplitude should not exceed the range and reach the other zero-crossing point, because this will affect the collected data and will be mixed with other points from different steps of the mirror. In order to achieve this, i.e. collection the data at each zero-crossing, we need the amplitude of the oscillator to be $\lambda/4$ of the laser wavelength from each side; that is, the maximum amplitude should be $\lambda/2$ of the

Reproduced with permission of the copyright owner. Further reproduction prohibited without permission.

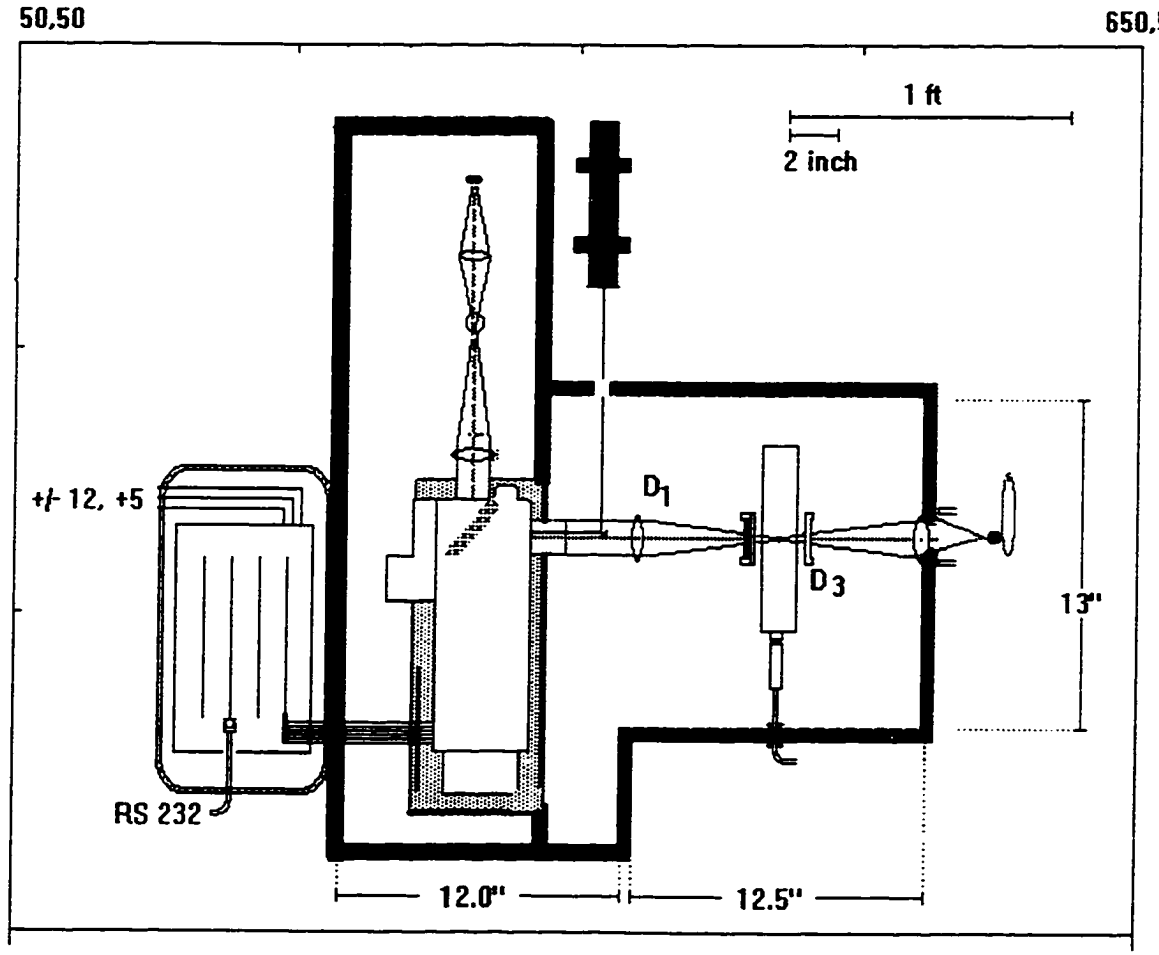

Figure 3-8: Optical layout of phase-2

Reproduced with permission of the copyright owner. Further reproduction prohibited without permission.

laser wavelength. The procedure for determining this amplitude is described below:

3.5.3.2.1- Determination the amplitude of the phase modulation (PM)

A sine wave will be applied to the moving mirror from a wave generator at a desired frequency, 400 Hz in our experiments. The value of this frequency is important, since the VCD is a double modulation instrument, that is the phase modulation and a modulation at PEM (vide infra). Therefore, in order to avoid the cross-talk between these two frequencies one needs them to be apart from each other as much as possible. As a result of the applied sine wave the moving mirror will dither at the frequency of the sine wave, applied to the mirror coil, and a distance proportional to the amplitude of the sine wave. As a result, the laser reference signal will also be modulated and will appear as a single sine wave at the same frequency as the applied jitterng frequency. The laser signal can be monitored via an oscilloscope, simply by connecting the output of the laser detector from the interferometer board to the oscilloscope. As we

Reproduced with permission of the copyright owner. Further reproduction prohibited without permission.

mentioned above, we need to take samples at every laser zero crossings; therefore we need to set the amplitude of the sine wave such that the mirror dithers at only that point i.e., it won't reach the other point or points. To assure this, the amplitude of the sine wave is adjusted until the shape of the modulated laser signal on the oscilloscope reaches close to a flat top sine wave shape, Figure 3-9b. If however, the amplitude is increased above this level, the frequency of the sine wave monitored on the oscilloscope doubles, because the moving mirror is reaching a second zero crossing point and the data are mixed with other points. Figure 3-9 is the schematic illustration for the connections and the shape of the laser sine wave on the oscilloscope.

Reproduced with permission of the copyright owner. Further reproduction prohibited without permission.

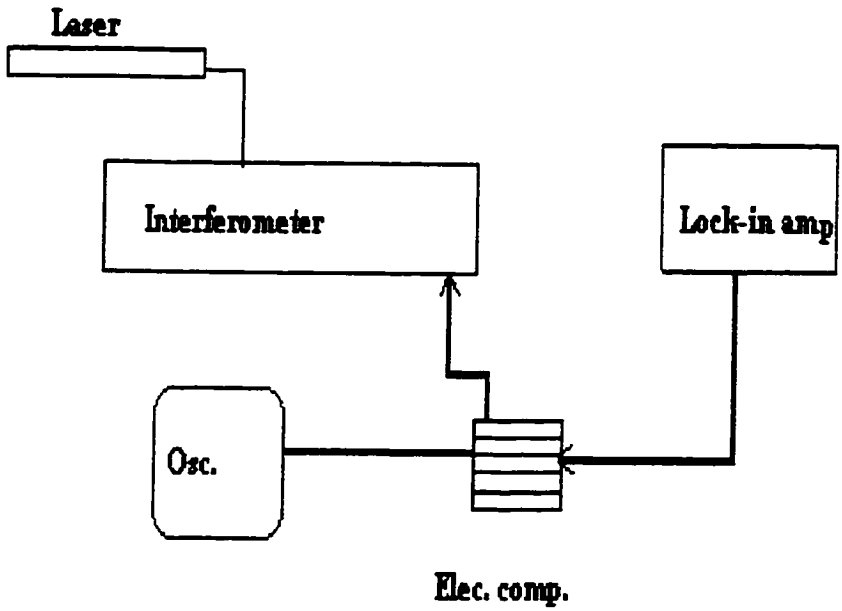

(a)

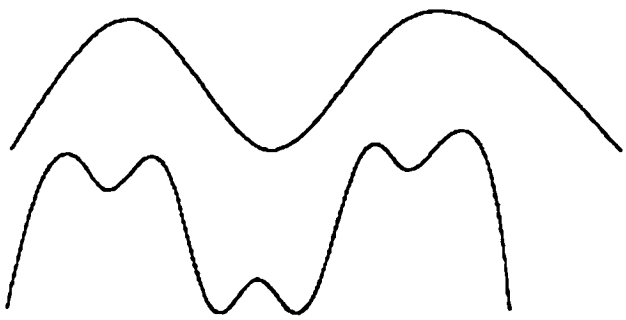

(b)

Figure 3-9: *(a) Schematic illustration of the phase modulation amplitude determination setup, (b) Shape of the modulated laser signal.*

Reproduced with permission of the copyright owner. Further reproduction prohibited without permission.

3.5.4- Electronic layout, Phase 2

The electronic layout of the SS-FT-VCD unit is summarized in Figure 3-10. The double modulation is provided by the PEM (at 37KHz) and the phase modulation, provided by a signal generator from the lock-in amplifier. This signal at 400 Hz and with an amplitude corresponding for ½ He-Ne wavelength is supplied to the stop-and-Go board of the electronic controller of the interferometer.

The signal from the detector is first amplified by a preamplifier (Infrared Associates), and subsequently split into two paths for processing I_{dc} and I_{ac}. One of them leads to the first lock-in amplifier (SR5 10, Stanford Research Systems), demodulating at internal phase modulation frequency (400 Hz) of the interferometer to extract the I_{dc} signal. The output of this lock -in amplifier is the I_{dc} analog signal and its converted to a digital signal by a 100 kHz, 16 bit A/D converter (CIO-DAS1600)and read via a 90MHz Pentium PC computer (Gateway 2000 P5-90).

Reproduced with permission of the copyright owner. Further reproduction prohibited without permission.

The other signal from the detector is first passed through an active filter to remove contamination of the I_{ac} from the I_{dc} components. The output of this filter is send to the second lock-in amplifier (EG & G Instruments, model 5209) to demodulate the I_{ac} signal at 37 KHz. The output of this lock-in amplifier is fed into another channel of the A/D converter, and read via the computer. After both signals, I_{dc} and I_{ac} are send to the computer, the VCD is obtained by calculations using the software written in our laboratory.

Reproduced with permission of the copyright owner. Further reproduction prohibited without permission.

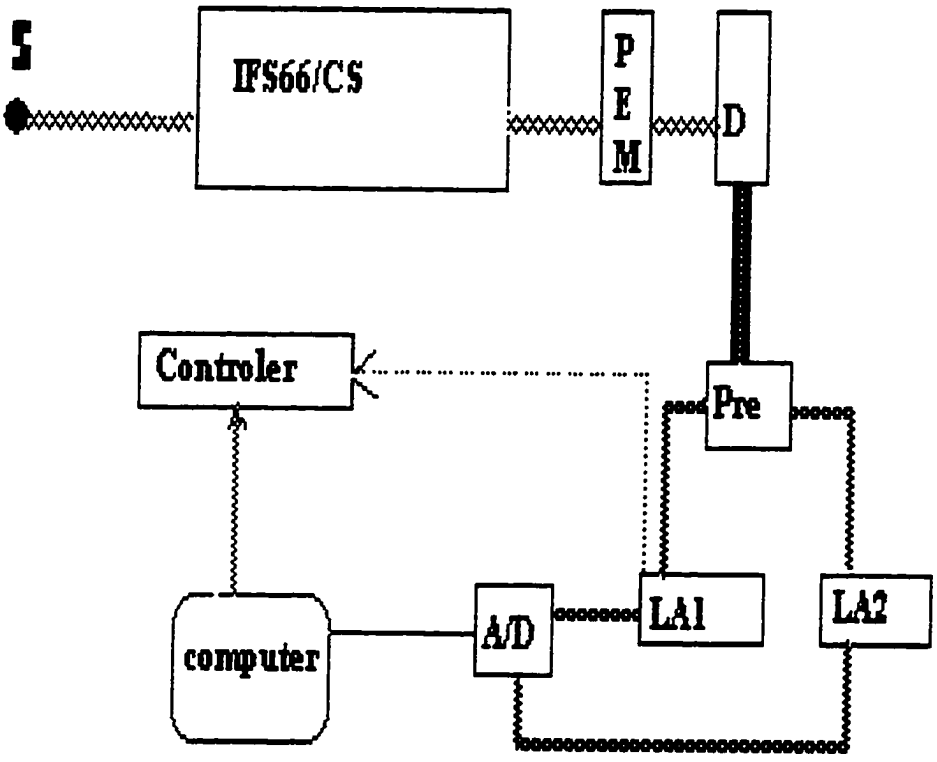

Figure 3-10: *Electronic layout of the VC3 instrument*

Reproduced with permission of the copyright owner. Further reproduction prohibited without permission.

3.5.5- Calibration and testing the performance of the instrument.

The conversion of phase 1 to phase 2 layout of VC3 has produced a drastic improvement of the DC and AC interferograms.

After obtaining a better signal-to-noise ratio for the I_{dc}, we started to measure the I_{ac} and obtain a VCD signal.

As in a dispersive VCD instrument, one needs first to calibrate the intensity and make sure that the instrument works properly. For this purpose we use a birefringent plate followed by a polarizer at the sample position. There are four possible orientations of the birefringent plate and second polarizer. In each of these cases the light from the interferometer is first vertically polarized and the principal modulator stress is oriented at 45^0 with respect to the first polarizer. The fast axis of the birefringent plate can then be either parallel or perpendicular to the first one. At the wavelength point of quarter - wave retardations, the wave plate will convert alternating left and right circularly polarized light from the modulator to light that is alternating between

Reproduced with permission of the copyright owner. Further reproduction prohibited without permission.

vertical and horizontal linearly polarized light. The second polarizer then alternately beam at the modulation frequency. This corresponds to a pseudo - CD signal that is of the same magnitude as the overall instrumental transmission. Figure 3-11 shows this signal which is the first artificial VCD signal obtained from the FTVCD [VC3] instrument and it shows that the instrument is calibrated and can be used to VCD measurements for a real samples.

For most of the VCD instrument calibration and the test of the performance, an organic compound Pinene is used and compared to the standard spectra obtained from the instruments with an optimum operational conditions. Therefore, to test the performance of the VC3 we used (+)- pinene and obtained the VCD spectrum. The sample used is neat (+)- pinene in a variable path length CaF_2 cell at a path length. From this spectrum, by comparing it to previous results we have from the dispersive VCD instrument (VC1) we can see that the instrument is ready for the operation.

Reproduced with permission of the copyright owner. Further reproduction prohibited without permission.

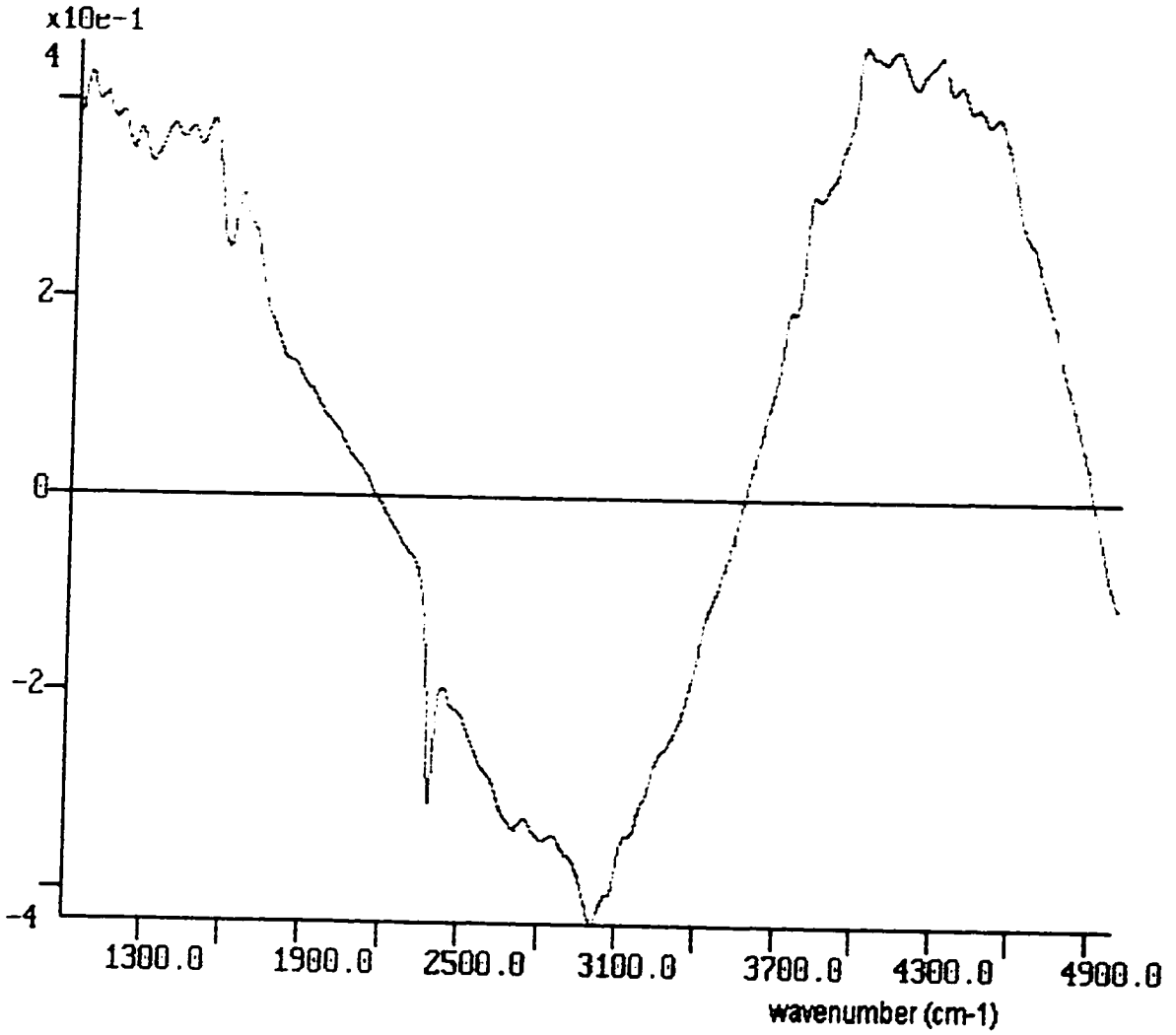

Figure 3-11: The first pseudo - CD signal obtained from FTVCD (VC3).

Reproduced with permission of the copyright owner. Further reproduction prohibited without permission.

Reference:

1- L. A. Nafie, L. C. Cheng and P. J. Stephens (1975) *J. Amer. Chem. Soc.* , 97, 3842.

2- G. Holzwarth, E. C. Hsu, H. S. Mosher, T.R. Faulkner and A. Moscowitz (1974) *J. Amer. Chem. Soc.*, 96, 251.

3- N. J. Greenfield and G.D. Fasman (1969) *Biochemistry*, 8, 4108.

4- F. M. Pohl and T.M. Jovin (1972) *J. Mol. Biol.*, 67, 375.

5- T. A. keiderling (1990), *"Practical Fourier transform infrared spectroscopy: Industrial and laboratory chemical analysis"*, J. R. Ferraro, & K. Krishnan, Eds., Academic Press, NY, pp. 203-284.

6- M. Diem, G. M. Roberts, O. Lee and A. Barlow (1988) *Appl. Spectrosc.*, 42,

7- L. A. Nafie, M. Diem and D.W. Vidrine (1979) *J. Amer. Chem. Soc.*, 101, 496.

8- P. R. Griffiths and J. A. de Haseth (1986) *" Fourier transform infrared spectroscopy"*, JOHN WILEY & SONS.

Reproduced with permission of the copyright owner. Further reproduction prohibited without permission.

9- P. Malon and T. A. Keiderling (1988) *Appl. Spectrosc.*, 42, 32.

10- O. Lee (1992), Ph.D. theses, CUNY.

11- E. D. Lipp and L. A. Nafie (1984) *Appl. Spectrosc.*, 38, 20.

12- N. Ragunathan, N. S. Lee, T. B. Freedman, L. A. Nafie, C. Tripp, and H. Buijs (1990) *Appl. Spectrosc.*, 44, 5.

13- P. L. Polavarapu, (1985), " *Fourier transform Infrared vibrational circular dichroism* ", Academic press, New York.

14- C. Marcott, A. E. Dorey, and I. Noda (1993) *Appl. Spectrosc.*, 47, 1324.

15- B. Wang and T. A. Keiderling (1995) *Appl. Spectrosc.*, 49, 1347.

16- C. J. Manning and R. A. Palmer (1991) *Rev. Sci. instrum.* 62(5), 1219.

17- J. Connes and P. Connes (1966) *J. Opt. Soc. Am.*, 56, 896.

18- L. A. Nafie and M. Diem (1979) *Appl. Spectrosc.*, 33.130.

19- ay Wylie, L. C. Barrett (1995) " *Advanced Engineering Mathematics* ", McGraw-Hill, Inc., New York.

Reproduced with permission of the copyright owner. Further reproduction prohibited without permission.

Chapter four

The Solution Structure of Small Peptides: An Infrared CD Study of Aqueous Solutions of (L-Ala)n [n=3,4,5,6] at Different Temperatures and Ionic Strengths

Reproduced with permission of the copyright owner. Further reproduction prohibited without permission.

4.1- Introduction

The determination of the solution structure of biological molecules is one of the central themes of modern biophysical research, and many experimental and theoretical methods have been developed to deduce this information. There exist a number of spectroscopic techniques which have been used successfully to measure or deduce the structure of several classes of biomolecules, among them peptides and proteins. These molecules are of particular significance since proteins are the catalysts of most biochemical reactions, and their enzymatic activity is a direct result of their solution conformation.

Small peptides, with less than 20 amino acids, are known to fulfill a number of biological roles as well, be it as small peptide hormones, pheromones or other functions. The actions of such small peptides is in a sense even more fascinating than that of large peptides or proteins, because the solution structure is less well defined in a small peptides. This is, because in a large protein there are often covalent linkages, or long structural motifs such as helices and sheets, which determine and stabilize the

Reproduced with permission of the copyright owner. Further reproduction prohibited without permission.

secondary structure of a protein. In a small peptide, such stabilizing motifs are necessarily much shorter, and structures are generally less rigid and less well defined.

In addition to a lesser degree of structural integrity of these small peptides, there exists a problem of observing these solution structures. For larger peptides, up to about 120 or 150 amino acids, NMR spectroscopy is the major technique for the determination of accurate solution conformations. Most of this information is derived from the measurement of through - space coupling of nuclear spins in NOE experiments, which yield a map of distance relationships of spins less than about 3.5 $\overset{0}{A}$ apart.

The distances between the interacting nuclei is refined into a molecular structure, using the primary peptide structure and preferred conformational angles as constraint parameters. These, and related NMR techniques, have produced solution structures in excellent agreement with solid phase conformations, and are considered reliable and accurate.

One limitation of these methods is the slow spin - spin relaxation in NMR spectroscopy, which sets a lower limit of

Reproduced with permission of the copyright owner. Further reproduction prohibited without permission.

interaction time scale: if the molecule conformation changes faster than the time required for two spins to interact, then the corresponding signal is subject to averaging over all conformations populated during the NMR time scale. Thus, small, flexible peptides often have not revealed a discernible solution conformation. This problem has only recently been addressed in detail by NMR spectroscopists [1].

In order to study the conformation of flexible peptide chains, other spectroscopic techniques have been utilized, among them vibrational spectroscopy and CD. Both these techniques sample molecular conformation on a time scale more than a million times faster than NMR spectroscopy and faster than the conformational fluctuations of the peptide. Unfortunately, vibrational spectroscopy is mostly a qualitative conformational tool, and the assignment of peptide structure from CD spectra is very difficult due to extension overlap of CD signals. Nevertheless, CD data often have suggested that small peptides have some structure, although a quantitative structure determination is difficult.

Reproduced with permission of the copyright owner. Further reproduction prohibited without permission.

Diem [2,18] and others [4] have shown that infrared circular dichroism, also known as vibrational CD (VCD) is a sensitive probe of peptide solution conformation. VCD can detect peptide structure even in molecules where NMR yields no observable structural information, and where the CD data are ambiguous. VCD signals may be used, in some instances, to determine the peptide conformation qualitatively or even quantitatively, based on model studies and computational methods developed.

4.1.1- The Coupled Oscillator, applied to the determination of peptide solution conformation.

VCD has been applied to conformational investigations of peptides, in both aqueous [1-3] and organic media [4-8]. In all these reports, the sensitivity of VCD towards the peptide secondary structure was demonstrated, mostly for the amide I and I' vibrations (the prime denotes vibrations of the deutrated peptide linkage). This sensitivity toward the secondary structure originates from the coupling of identical and virtually achiral transitions of the peptide linkage, which are arranged in a

Reproduced with permission of the copyright owner. Further reproduction prohibited without permission.

dissymmetric pattern. The optical activity of such dissymmetric structure has been investigated in detail [9-13].

One of the important intermolecular interactions that has been found to be a sensitive probe of conformation, is the "coupled oscillator", a mechanism that results from quantum mechanical interaction of degenerate or near-degenerate states. This interaction was found to be necessary to explain certain band splitting in the ir and Raman spectra of extended chain polypeptides and may be used to explain certain features in the VCD spectra as well.

In the coupled oscillator model, two identical achiral groups, such as carbonyl stretching or amide I vibration interact and form symmetrically and antisymmetrically coupled vibrational states |+> and |->, respectively. The |+> and |-> states are split by the equivalent of a vibrational exciton, which can amount from a few to about a hundred wave numbers, depending on the dipole strength, geometry, and proximity of the oscillators.

The vibrational optical activity of a dimer of oscillation is characterized by the rotational strengths R of the vibrational

Reproduced with permission of the copyright owner. Further reproduction prohibited without permission.

transitions. For two identical achiral (vibrational) transitions located on groups 1 and 2, the rotational strength $R^{\mp}$ for the symmetric |+> and antisymmetric |-> coupled states is given by [9,14]:

$$R \pm = \mp \ (\pi \nu_0/2)\, T_{12} .\mu_1 .\mu_2 \qquad (4\text{-}1)$$

where T_{12} is the distance vector between the center of masses of the two oscillators, μ_1 and μ_2 are their dipole moments, and ν_0 is the center wavenumbers of the coupled transitions. The coupled states may be written as

$$|+> = \{ 1/\sqrt{2}\} [1^0 2^1 + 1^1 2^0]$$
$$|-> = \{ 1/\sqrt{2}\} [1^0 2^1 - 1^1 2^0] \qquad (4\text{-}2)$$

Here, 1 and 2 denote the wave function on oscillators 1 and 2, and the superscripts 0 and 1 denote the ground and one photon excited states, respectively. The interaction between the dipoles, i.e., the splitting observed in the ir spectrum between the symmetric and antisymmetric coupled vibrational states, can be expressed by

$$\nu_{\pm} = \nu_0 + V_{12} \qquad (4\text{-}3)$$

Reproduced with permission of the copyright owner. Further reproduction prohibited without permission.

where V_{12} in $(esu \cdot cm)^2$ is assumed to be a standard dipole - dipole interaction [15]

$$V_{12} = \frac{\mu_1 \cdot \mu_2}{|T_{12}|^3} - \frac{3(\mu_1 \cdot T_{12})(\mu_2 \cdot T_{12})}{|T_{12}|^5} \qquad (4\text{-}4)$$

The magnitude of the dipole transition moments, μ_1 and μ_2 are obtained from the observed spectra. The approximation (for Lorentzian peaks) [16] was used:

$$\mu = \int \frac{\varepsilon}{\nu} d\nu = 0.92 \times 10^{-38} \frac{\varepsilon_{max} \cdot \omega}{\nu} \qquad (4\text{-}5)$$

where ω denotes the half - width at half - heights of the observed band. Furthermore, the ir intensities of the |+> and |-> states are given by

$$D^{\pm} = |\mu|^2 \pm \mu_1 \cdot \mu_2 \qquad (4\text{-}6)$$

The dipolar coupling energies V_{ij} between interacting groups (such as amide I vibrations (C=O) of peptides) may provide a handle to the origin of the observed VCD as well. The V_{ij} elements depend on the distance and the orientation between these interacting groups.

Reproduced with permission of the copyright owner. Further reproduction prohibited without permission.

Since VCD is a technique which monitors short distance interaction, its conformational sensitivity is particularly pronounced and useful in the studies of small peptides.

According the exciton formalism [17], large rotational strengths are created for perpendicular geometry between the interacting groups. Such a geometry, however, produces the smallest coupling energy and splitting of the exciton components. On the other hand, a parallel or antiparallel geometry between the interacting groups will produce maximum splitting, but minimal rotational strengths. Thus, one may conclude that large VCD intensities are associated with the intermediate values of V_{ij} of the distance between the two interacting groups does not change much between the conforms.

The mixing between two interacting group coordinates depends on dipole coupling energy, V_{ij}. Large and small V_{ij} values may prevent the formation of couplet; a large term because of near parallel geometry, and a small term for lack of coupling. The near parallel geometry will produce a large coupling energy, but little optical activity. In practice, the observed splitting is generally

Reproduced with permission of the copyright owner. Further reproduction prohibited without permission.

less than the bandwidth of the vibrational transitions, and therefore only a distorted band is observed in the absorption spectra, instead of distinct peaks due to the transitions into the |+> and |-> states. However, the generation of transition pairs having rotational strengths of approximately equal intensity but opposite sign in VCD is a characteristic feature of coupled oscillators. Therefore, the corresponding VCD spectra, show distinct positive - negative (or negative - positive) band shapes.

4.1.2- Previous VCD studied Ala_3 in aqueous solution.

In 1988, Diem's group reported the VCD spectra of L-Alanyl-L- Alanine (Ala_2) in aqueous solutions in the 1250 -1750 cm^{-1} region [18], and demonstrated that the chiral perturbation of the

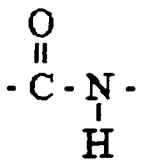

linkage is so small that virtually no VCD intensity is observed in the amide I' vibration.

Reproduced with permission of the copyright owner. Further reproduction prohibited without permission.

Unlike alanyl dipeptides, [3] the VCD spectrum of $(L\text{-}Ala)_3$ in a neutral D_2O solution displays a distinct negative - positive intensity pattern in the amide I' region [18].

This pattern was interpreted as an evidence of a stable conformer, at least on the time scale of 10^{-14} - 10^{-15} second, thus, indicating the existence of a preferred solution conformation stabilized by zwitterionic attractions.

In order to characterize the potential stabilizing factor for Ala_3 in water, other experiments were carried out. These experiments showed no couplet for either $(L\text{-}Ala)_3$ in a basic D_2O solution, or N-acetyl-L-alanyl-N'-methyl amide (AAMA, Figure 4-1) in a neutral D_2O solution, all of which contain the central

However, $L\text{-}Ala_3$ in basic solution, and AAMA lack the zwitterionic feature of Ala_3 in neutral media. The conclusion made was that without the zwitterionic interaction no stable solution conformer exists for a peptide with two amide linkages. Therefore, no VCD was observed. In the Results and Discussion section below, we present results that confirms this original interpretation. Furthermore, we demonstrate that the solution

Reproduced with permission of the copyright owner. Further reproduction prohibited without permission.

conformation of (L-Ala_n) (n=3-6) depend on n and the ionic strength of the media, and to a larger extent to the temperature.

Reproduced with permission of the copyright owner. Further reproduction prohibited without permission.

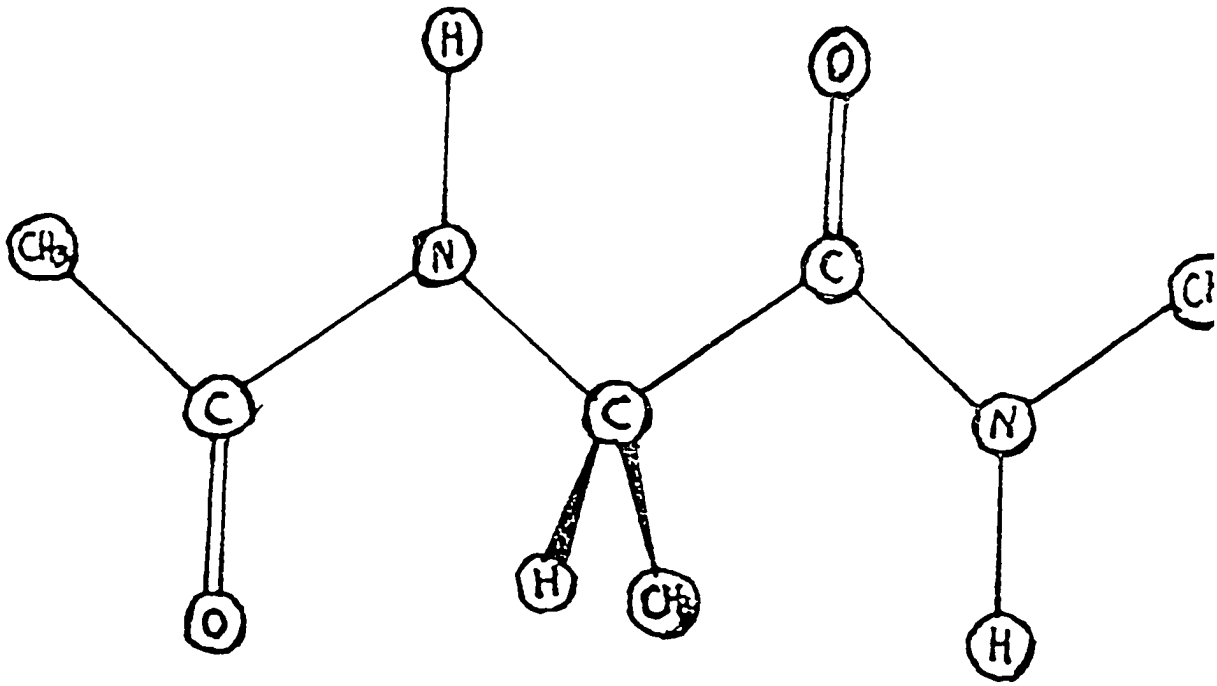

Figure 4-1: *Structure of N-acetyl-L-alanyl-N'-methyl amide AAMA. Adapted from ref. [2]*

Reproduced with permission of the copyright owner. Further reproduction prohibited without permission.

4.2-Methods and Materials

The oligomers $(L\text{-}Ala)_3$, $(L\text{-}Ala)_4$, $(L\text{-}Ala)_5$ and $(L\text{-}Ala)_6$ were obtained commercially and used without further purification. The Raman data of these peptides were compared to those of purified peptides, and found to agree exactly. For VCD measurements, the peptides were lyophilized from D_2O to exchange labile protons, and subsequently dissolved in D_2O to concentrations of *ca.* 50 mg/mL for the trimer (~ 0.2 M). The solubility of the oligomers decreases significantly as the chain length increases; consequently, the tetra-, penta- and hexamer spectra were acquired at much lower concentrations. Small amounts of ammonium deuteroxide were added to the larger oligomers to stabilize the solutions. Enantiomeric samples were available for the tri-, tera- and pentamers. VCD data on these D-alanine oligomers were used to construct exact VCD baselines. For the hexamer, the baseline of the pentamer was used.

VCD and infrared absorption spectra were obtained using the dispersive VCD spectrometer VC1. Samples were contained between CaF_2 plates separated by 25 μm spacers. For the

Reproduced with permission of the copyright owner. Further reproduction prohibited without permission.

evaluation of the dependence of the VCD spectra on the chain length, the data were normalized such that the area under the carboxylate antisymmetric stretching (1597 cm^{-1}) peak was scaled to the same intensity as in $(L\text{-}Ala)_3$ (vide infra).

The sample cells were temperature controlled by circulating water through a cell holder in close thermal contact with the cell. The VCD measurements as a function of temperature between 10 and 80 °C are quite difficult to carry out. At low temperature, the danger of condensation of atmospheric water exists, in spite of the dry air purge of the instrument sample chamber. At elevated temperatures, particularly at 80 °C , the cells tend to leak, and vaporization of the solvent can lead to crystallization of the peptides. To ascertain that the samples were still properly dissolved, we have implemented the following procedure: all VCD spectra of a given sample were collected consecutively at 10, 25, 40, 60 and 80 °C. Subsequently, the sample was cooled back to 10 °C. Data were accepted only if the original and final spectra at 10 °C agreed.

Reproduced with permission of the copyright owner. Further reproduction prohibited without permission.

For most peptides in this study, the extreme values (10 and 80 °C) are reported, along with an intermediate value. In the case of $(L\text{-}Ala)_3$, spectra at 80 °C could not be obtained reliably since the signals were found to be very small. The data for the $(L\text{-}Ala)_6$ are experimentally the most uncertain, since the solubility of the hexamer is very low, even in basic solution (ammonium hydroxide-d_5).

Ionic strengths dependence for $(L\text{-}Ala)_3$ was measured by adding a small volume of concentrated solution of NaCl in D_2O to a stock solution of $(L\text{-}Ala)_3$ in D_2O such that the final salt concentration was approximately 0.03M, 0.06 M or 0.1 M. The spectra were recorded at 25 °C. Since both the carboxylate stretching mode, and the amide I' manifold appear to be changing in intensity, these spectra are represented scaled such that the overall absorption between 1550 and 1750 cm^{-1} is constant.

Reproduced with permission of the copyright owner. Further reproduction prohibited without permission.

4.3- Results

The dispersive and the FTIR spectra of $(L\text{-}Ala)_3$ in the range 1550 - 1750 cm^{-1} are shown in Figure 4-2. In this region there are two distinct peaks, one at 1595 cm^{-1}, the carboxylate ($-CO_2^-$) antisymmetric stretching mode and the other at 1654 cm^{-1}. This latter band is the amide I' (the prime denotes vibrations of the deutrated peptide linkage) absorption peak of the $(L - Ala)_3$, which is split into two components- as seen from the Figure 4-2. The splitting is due to the symmetric and antisymmetric combination modes of the two carbonyl (C=O) groups of the trialanine. This was shown previously [18]. The VCD spectrum of $(L\text{-}Ala)_3$ in D_2O in the range 1550 - 1750 cm^{-1} is shown in Figure 4-3. The spectrum shows a negative peak at 1598 cm^{-1} corresponding to the carboxylate absorption peak at 1595 cm^{-1}, and a negative - positive couplet (proceeding from lower to

Reproduced with permission of the copyright owner. Further reproduction prohibited without permission.

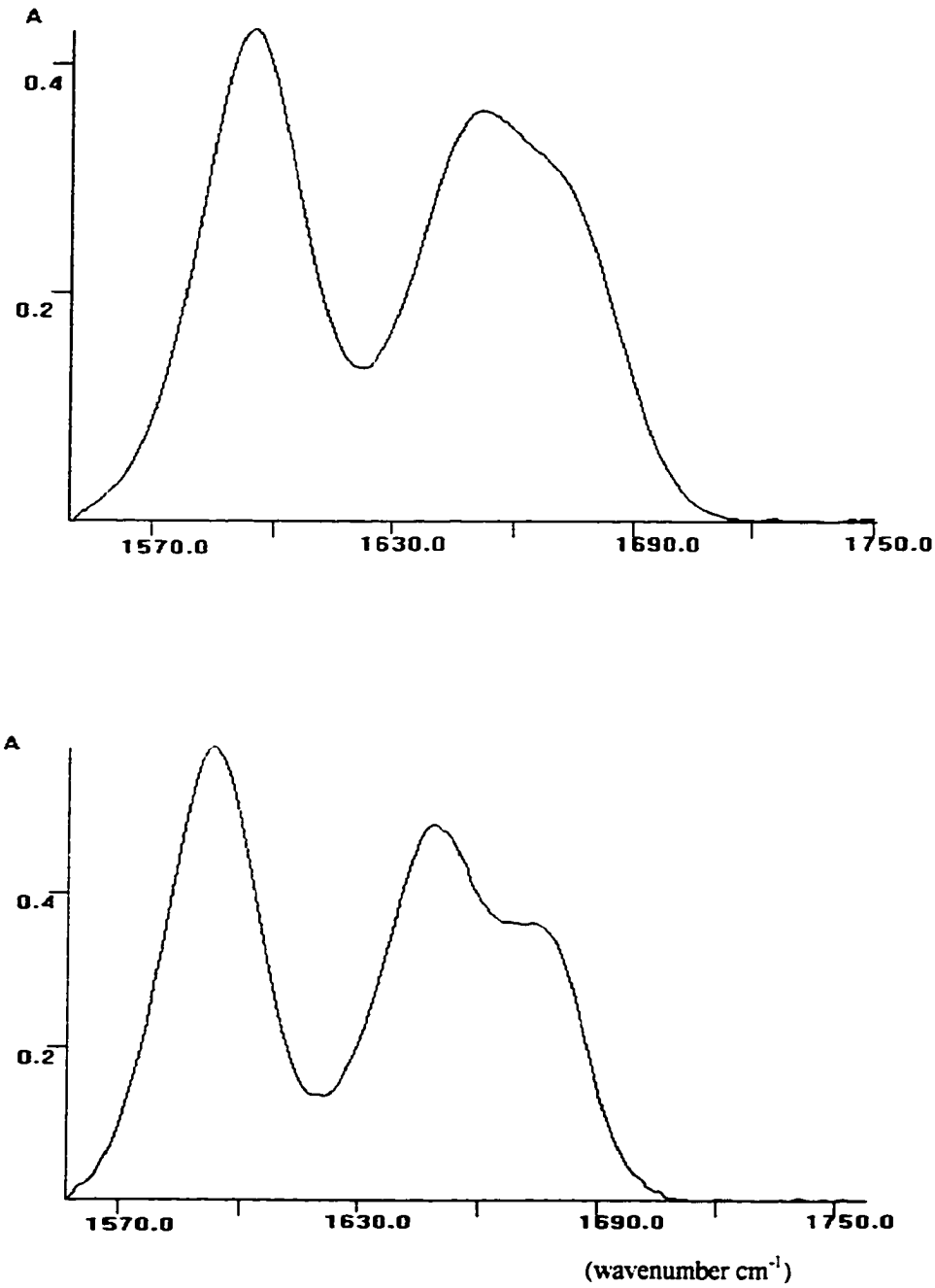

Figure 4-2: *infrared spectrum of 0.5 M L-Ala$_3$ in D$_2$O from the dispersive (above) and FTIR instrument (bottom).*

Reproduced with permission of the copyright owner. Further reproduction prohibited without permission.

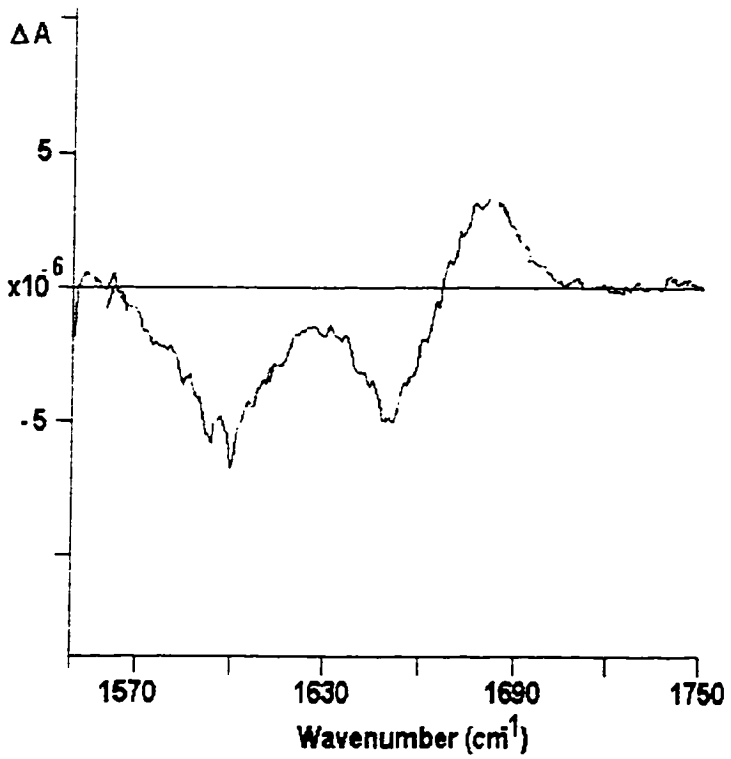

Figure 4-3: *The VCD spectrum of 0.5 M L-Ala$_3$ in D_2O.*

Reproduced with permission of the copyright owner. Further reproduction prohibited without permission.

higher wavenumber) with a zero - crossing at 1666 cm^{-1} corresponding the amide I' absorption peak at 1654 cm^{-1}.

This couplet was previously interpreted to be due to exciton interaction between two C=O groups of $(L\text{-}Ala)_3$ [18]. In order for such an interaction to be observed in VCD, we assume that $(L\text{-}Ala)_3$ exists in a solution conformation stabilized by a zwitterionic interaction, and that the molecule exists in one (or more) solution conformations that are stable on the vibrational time - scale, and that exhibit non - zero VCD intensities. This condition can be fulfilled by occurrence of a distribution of many slightly different conformations with similar VCD features, or the predominance of one or a few structures that will dominate the VCD spectra. In order to distinguish these cases, and to give more evidence for the stabilization due to the zwitterionic interaction, temperature and ionic strength dependent VCD spectra are required.

Reproduced with permission of the copyright owner. Further reproduction prohibited without permission.

4.31- Chain lengths dependence of the observed VCD signals

The infrared absorption and the VCD spectra of $(L\text{-}Ala)_4$ and $(L\text{-}Ala)_5$ in aqueous solution in the amide I' vibrational region are shown in Figure 4-4. All spectra, $(L\text{-}Ala)_n$, n=3, 4, 5 are normalized such that the intensity under the carboxylate antisymmetric stretching mode at ca. 1597 cm^{-1} is constant. Since each of the peptides has just one carboxylate antisymmetric stretching mode, and an increasing number of amide I' modes, this scaling gives a direct measure of the intensity increase as the oligomer chain length increases. Both the tetramer and the pentamer show two absorption peaks in the infrared spectra: the carboxylate antisymmetric and the amide I'. The lower frequency amide I' absorption maxima occurs at 1648 cm^{-1}. The negative - positive peak is observed with a zero-crossing shifted toward lower wavenumber (1654 cm^{-1}), Figure 4-4. The shift , as well as changes in the $\Delta A/A$ ratio of the signals, indicate that there is a significant conformational changes between the trimer and the larger analogues. These spectra are characterized by an increase

Reproduced with permission of the copyright owner. Further reproduction prohibited without permission.

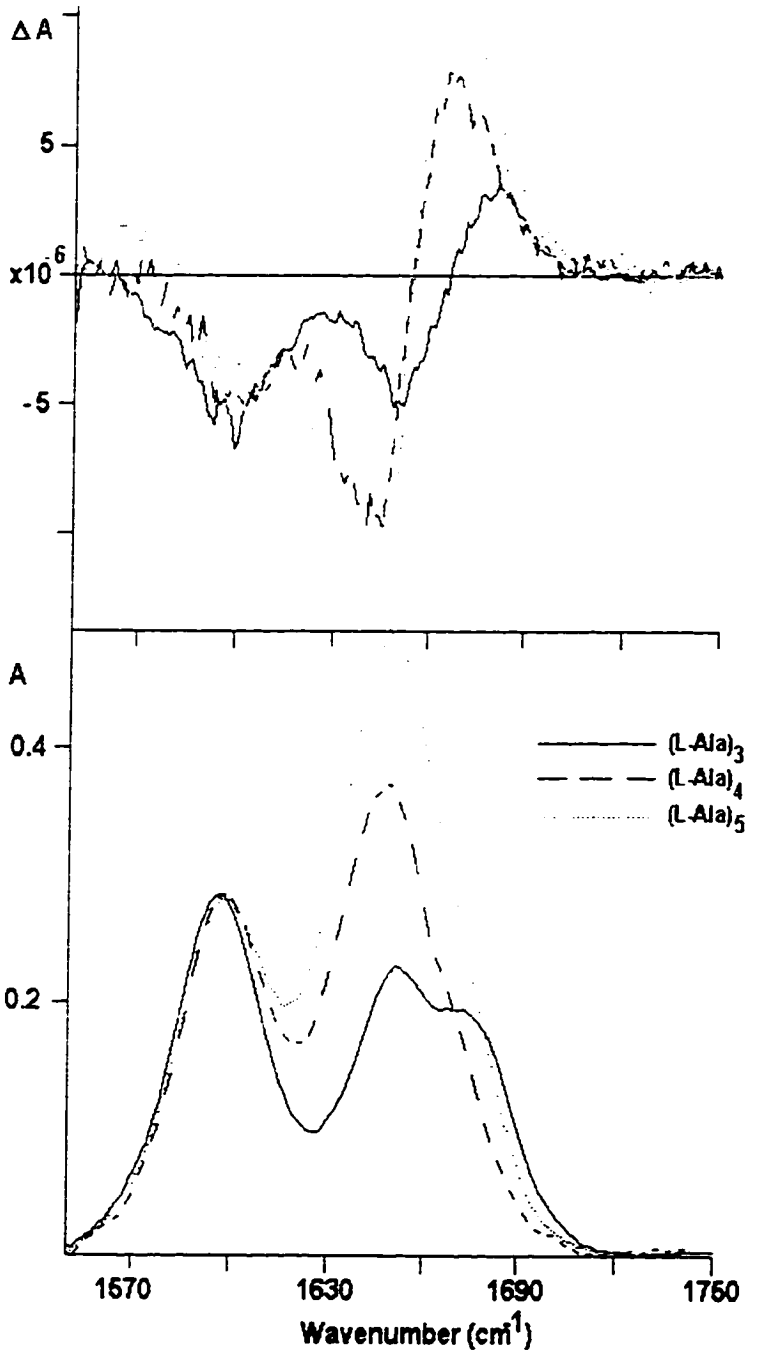

Figure 4-4: *Ir and VCD spectra of 0.5 M L-* Ala_n *, n=3,4,5.*

Reproduced with permission of the copyright owner. Further reproduction prohibited without permission.

of the ratio of intensities of the amide I' peak (1648 cm^{-1}) to the carboxylate antisymmetric stretching peak (1598 cm^{-1}) and an increase of the VCD amplitude, as n increases. The spectral parameters observed for these oligomers are summarized in Tables I - III.

The observed absorption spectra do not exhibit resolved amide I' components as in the case of $(L\text{-}Ala)_3$, but show a broad absorption envelope. Compared to $(L\text{-}Ala)_3$, there is a drastic increase in the VCD intensity, a sharpening of the VCD features, and a shift toward lower wavenumbers of the VCD zero - crossing. These observed results indicate a different solution structure for the trimer and the higher oligomers although the overall spectra appear similar at first glance.

Figure 4-5 shows a comparison of the $(L\text{-}Ala)_5$ and $(L\text{-}Ala)_6$ in the same spectral region. The spectral data are summarized in Tables III and IV. Between the penta- and the hexamer, there is an enormous increase in VCD intensity, coupled with a drastic decrease in the VCD band width and a shift toward lower wavenumber by 20 cm^{-1} of both the amide I absorption

Reproduced with permission of the copyright owner. Further reproduction prohibited without permission.

maximum and the zero crossing of the VCD spectrum. The frequency shift of the amide I peak is also manifested in the absorption spectra; however, the overall absorption band shapes and intensities are quite similar for the penta- and hexamers.

Reproduced with permission of the copyright owner. Further reproduction prohibited without permission.

Table I. Observed VCD and Absorption Frequency and Intensity Parameters for $(L\text{-}Ala)_3$ at 25 °C

Mode	Infrared		VCD	
	Frequency	Intensity	Frequency	Intensity
	cm^{-1}	absorbance units	cm^{-1}	10^{-6} absorbance units
ν_{carbox}	1597	0.57	1593	-6.8
	1652	0.46	1653	-6.5
$\nu_{amide\ I}$			1666	0.0
	1671	0.38	1673	+4.8

Table II. Observed VCD and Absorption Frequency and Intensity Parameters for $(L\text{-}Ala)_4$ at 25 °C

Mode	Infrared		VCD	
	Frequency	Intensity	Frequency	Intensity
	cm^{-1}	absorbance units	cm^{-1}	10^{-6} absorbance units
ν_{carbox}	1598	0.19	1604	-6.8
			1638	-6.5
$\nu_{amide\ I}$	1650	0.287	1658	0.0
			1668	+4.8

Reproduced with permission of the copyright owner. Further reproduction prohibited without permission.

Table III. Observed VCD and Absorption Frequency and Intensity Parameters for $(L\text{-}Ala)_5$ at 25 °C

Mode	Infrared		VCD	
	Frequency	Intensity	Frequency	Intensity
	cm^{-1}	absorbance units	cm^{-1}	10^{-6} absorbance units
ν_{carbox}	1597	0.57	1593	-6.8
			1653	-6.5
$\nu_{amide\ I}$	1652	0.46	1666	0.0
			1673	+4.8

Table IV. Observed VCD and Absorption Frequency and Intensity Parameters for $(L\text{-}Ala)_6$ at 10 °C

Mode	Infrared		VCD	
	Frequency	Intensity	Frequency	Intensity
	cm^{-1}	absorbance units	cm^{-1}	10^{-5} absorbance units
ν_{carbox}	1600	0.57	1600	-5.8
			1625	-22.0
$\nu_{amide\ I}$	1633	0.94	1633	0.0
			1668	+25.5

Reproduced with permission of the copyright owner. Further reproduction prohibited without permission.

Table V. Temperature Dependence of the VCD Amplitude of $(L\text{-}Ala)_4$ and $(L\text{-}Ala)_5$[a]

	$(L\text{-}Ala)_4$	$(L\text{-}Ala)_5$
10 °C	1.9×10^{-5}	2.5×10^{-5}
60 °C	1.2×10^{-5}	2.2×10^{-5}
80 °C	0.8×10^{-5}	1.9×10^{-5}

a) determined as the difference $\Delta A(1666\ cm^{-1}) - \Delta A(1642\ cm^{-1})$

Reproduced with permission of the copyright owner. Further reproduction prohibited without permission.

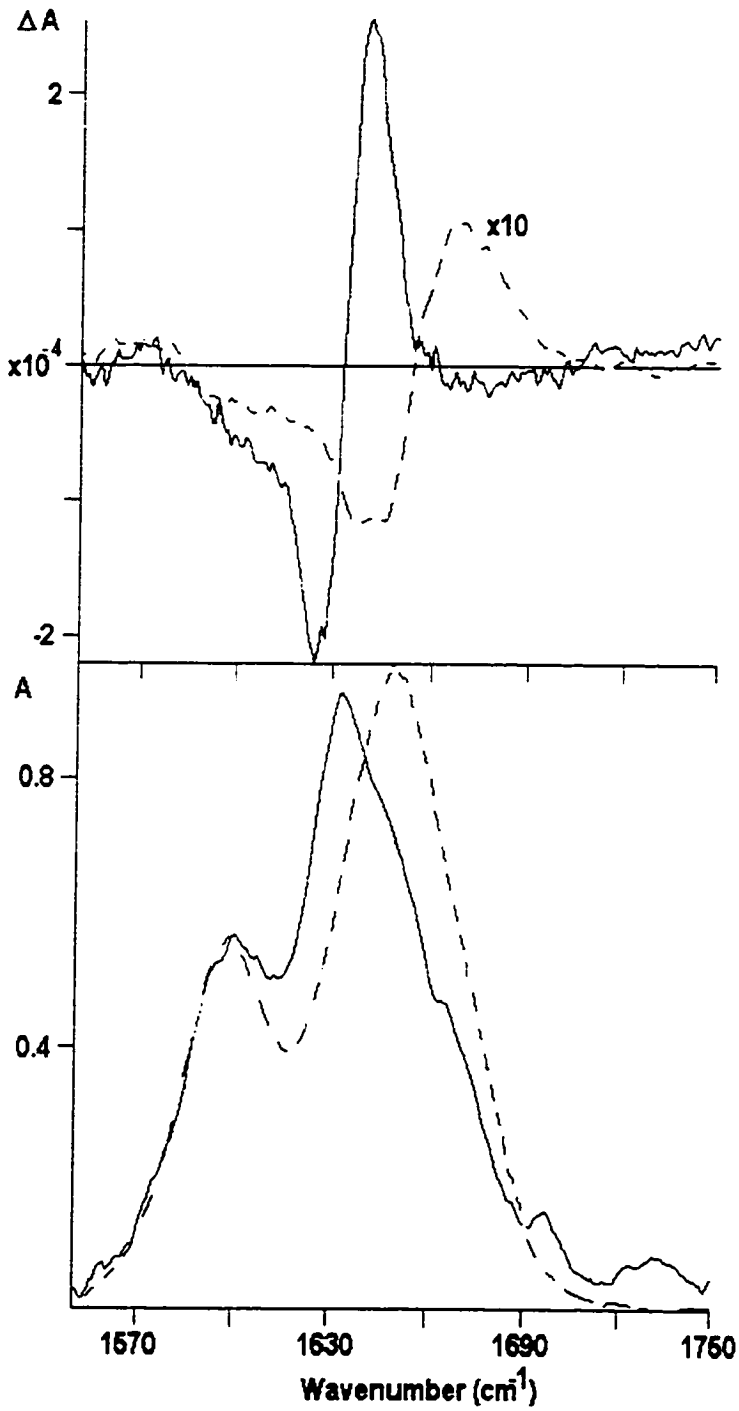

Figure 4-5: Comparison of the $(L\text{-}Ala)_5$ and $(L\text{-}Ala)_6$ infrared (bottom) and VCD (top) spectra

Reproduced with permission of the copyright owner. Further reproduction prohibited without permission.

4.3.2- Temperature dependence of absorption and VCD spectra.

The temperature dependence of the VCD spectra for (L-Ala)$_3$, (L-Ala)$_4$, (L-Ala)$_5$ and (L-Ala)$_6$ are shown in Figures 4-6, 4-7, 4-8 and 4-9. In all cases, the absorption spectra show relatively small changes. However, the amplitude of the VCD spectra for all oligomers decreases significantly between 10 and 80 °C. The decrease is most pronounced in the hexamer. The VCD intensities as function of temperature are summarized in Table V. The spectra of the tetra- and pentamer show a similar temperature dependence, characterized by a decrease in VCD intensity of about 50 % between 10 °C and 80 °C. In the case of (L-Ala)$_3$, the VCD at 80 °C could not be observed, presumably because the signal disappeared. Between 10 and 60 °C, however, a similar decrease in VCD intensity as in the tetra- and pentamer was observed.

The hexamer shows a much more drastic change, both in amplitude and frequency shifts. We believe that in this molecule, there is a drastic change in solution conformation between the

Reproduced with permission of the copyright owner. Further reproduction prohibited without permission.

two temperatures reported, whereas in the smaller oligomers the reduction of VCD amplitude is due to the decrease in stability of the conformation responsible for the dominant VCD effect. This will be elaborated upon in the Discussion Section below.

Reproduced with permission of the copyright owner. Further reproduction prohibited without permission.

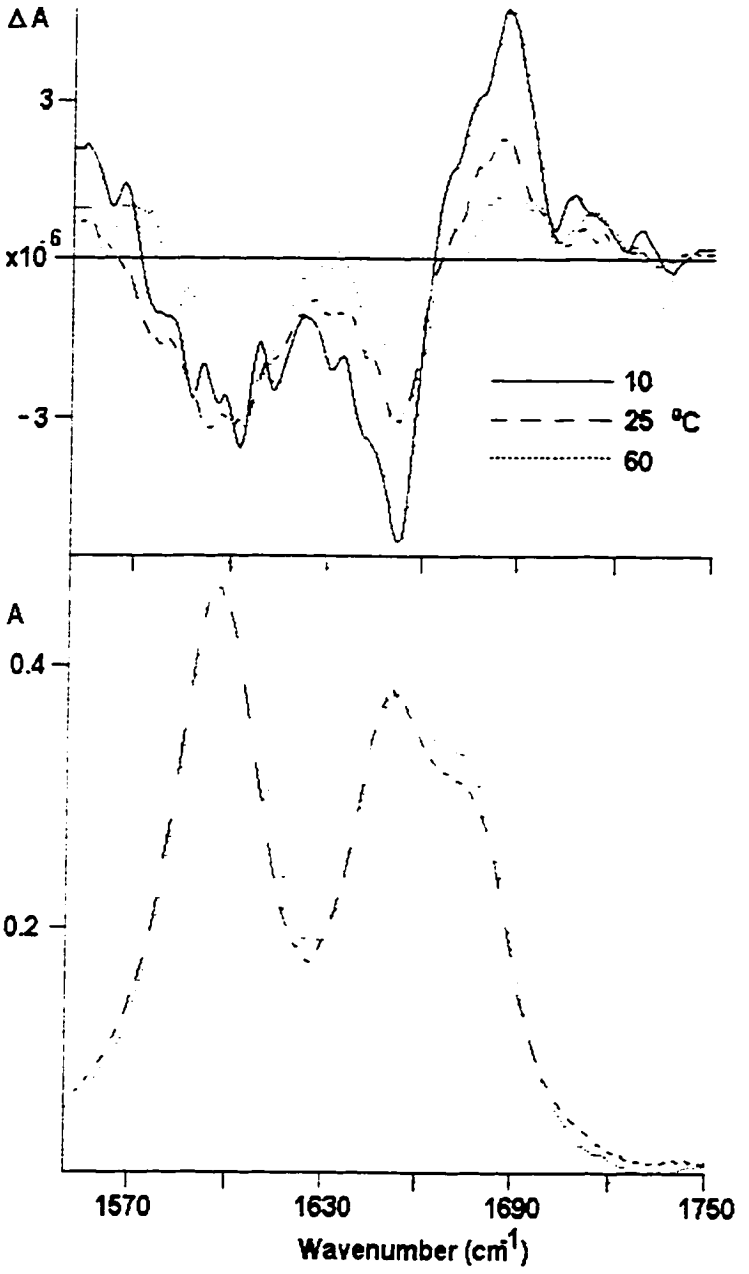

Figure 4-6: Temperature effect on the VCD spectra of L-Ala$_3$, 10, 25,60 °C.

Reproduced with permission of the copyright owner. Further reproduction prohibited without permission.

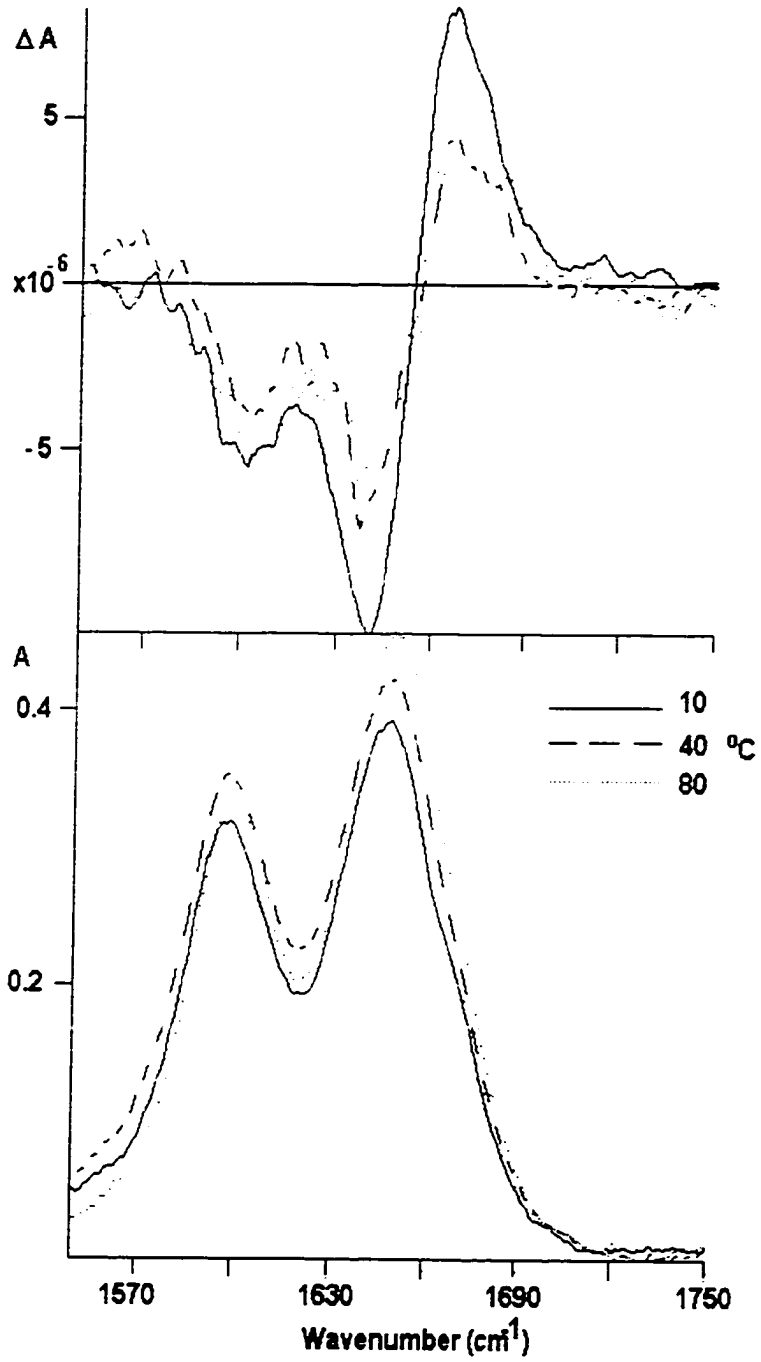

Figure 4-7: Temperature effect on the VCD spectra of L-Ala$_4$, 10, 40, 80℃

Reproduced with permission of the copyright owner. Further reproduction prohibited without permission.

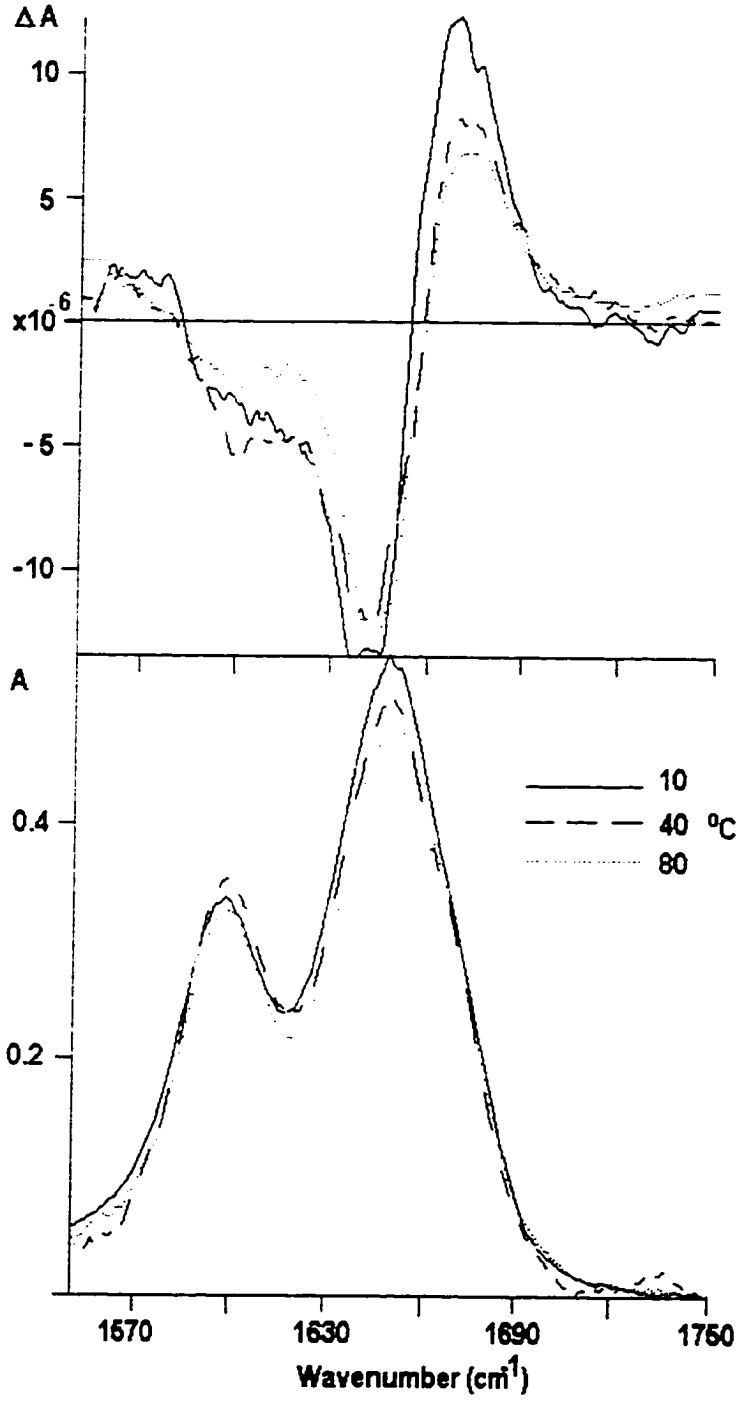

Figure 4-8: *Temperature effect on the VCD spectra of L-Ala$_5$, 10, 40, 80℃*

Reproduced with permission of the copyright owner. Further reproduction prohibited without permission.

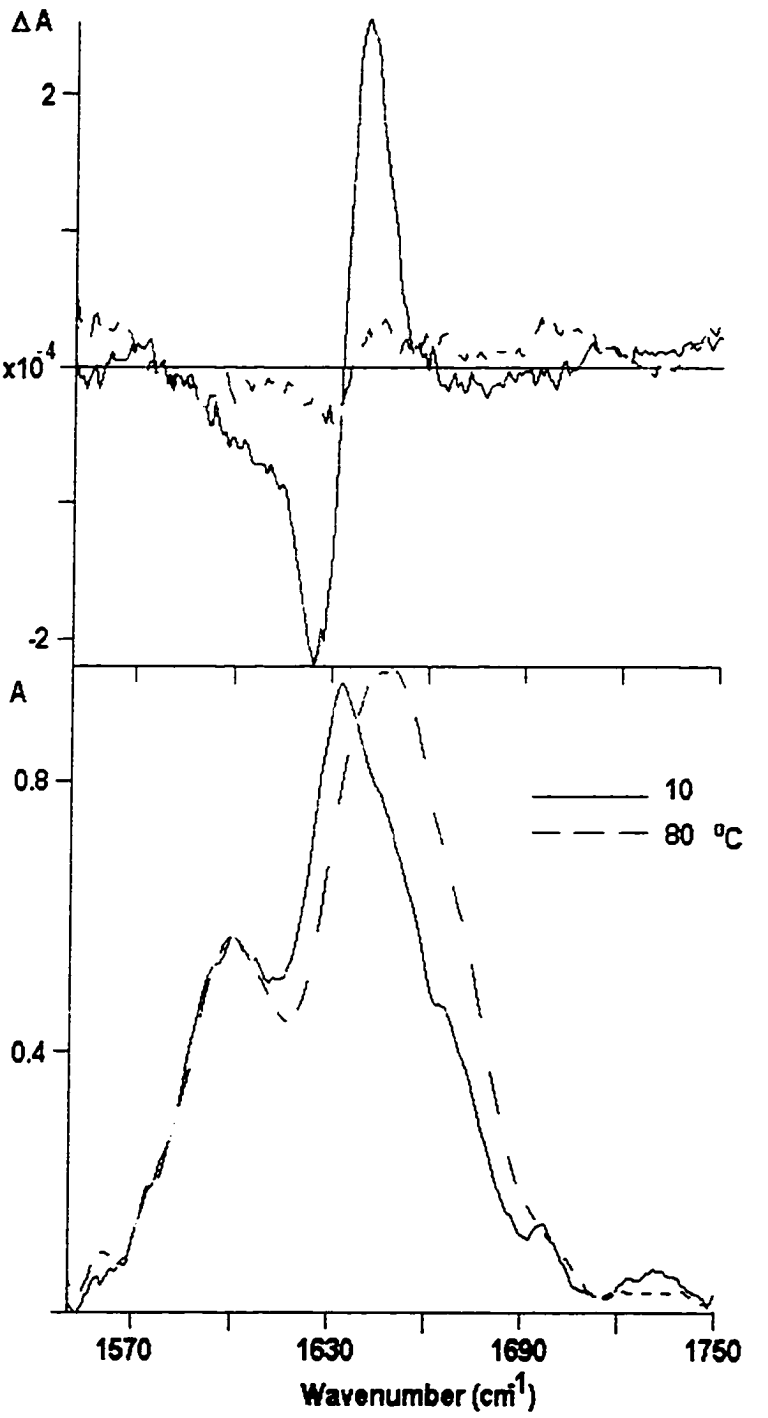

Figure 4-9: Temperature effect on the VCD spectra of L-Ala$_6$, 10, 40, 80℃

Reproduced with permission of the copyright owner. Further reproduction prohibited without permission.

4.3.3- Ionic strength dependence of VCD spectra

4.3.3.1- Low concentration:

VCD and ir absorption spectra of the trialanine in 0.03M, 0.06M NaCl in D_2O are shown in Figure 4-10. The 0.03M concentration of salt, as shown from the Figure 4-10 has no significant effect on the carboxylate absorption peak. However, the amide I' absorption intensity has decreased by 0.086 abs. units with respect to the trialanine in D_2O, and the resolution of this peak (amide I' symmetric and antisymmetric combination mode) has somewhat increased. The ratio of the intensity of these two combination modes (symmetric and antisymmetric) also slightly change with an increase in the intensity of the symmetric mode.

The effect of 0.06 M on the ir absorption spectrum of the (L-Ala)$_3$ is similar to that of 0.03M. However, a shift in the amide I' peak by 7 cm^{-1} towards higher wavenumber and a slightly decrease in the intensity of the carboxylate and amide I' peaks in 0.06M NaCl is observed from the absorption spectrum.

Reproduced with permission of the copyright owner. Further reproduction prohibited without permission.

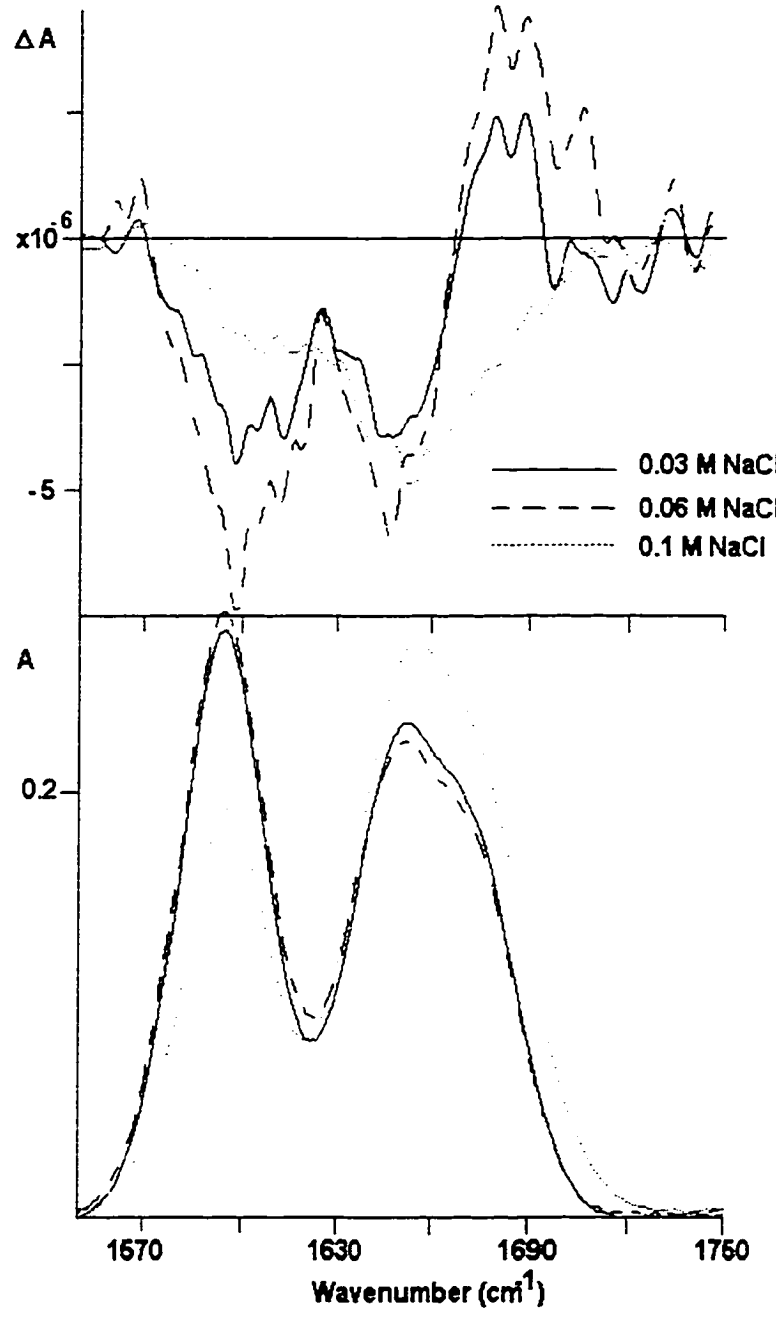

Figure 4-10: *Effect of 0.03 and 0.06M (low concentration) and 0.1M (high concentration) NaCl on the ir and VCD specra of L-Ala$_3$ in D_2O*

Reproduced with permission of the copyright owner. Further reproduction prohibited without permission.

The effect of 0.03 and 0.06M NaCl on the VCD spectrum is very small; there is no change in the carboxylate negative peak for 0.03M concentration with respect to (L- Ala)$_3$ in D_2O. However, for both concentrations there is a shift (5cm^{-1}) in the zero - crossing of the negative - positive couplet to a higher wavenumber. An increase in the negative intensity of the carboxylate peak and the negative - positive couplet in 0.06M concentration with respect to 0.03 M is observed.

4.3.3.2- High concentration

VCD and ir absorption spectra of the (L-Ala)$_3$ in 0.1 M NaCl are also shown in Figure 4-10. From these absorption spectra we see that as a result of addition of 0.1M NaCl to trialanine in D_2O, there is a slight shift in the carboxylate absorption peak (2 cm^{-1}) to a higher wavenumber with respect to the trialanine absorption peak in D_2O.

Furthermore, we observe a drastic change in the intensity ratio of the carboxylate *vs* the amide I' peaks. Furthermore, the amide I' peaks are shifted by ca. 12 cm^{-1} to a higher wavenumber with respect to the trialanine in D_2O. The splitting of the symmetric

Reproduced with permission of the copyright owner. Further reproduction prohibited without permission.

and antisymmetric vibrations of the C=O has almost disappeared in the ir spectra, and shows a little shoulder in FTIR spectrum; i.e. the ratio of the symmetric to antisymmetric mode has increased significantly with a decrease in the symmetric mode and an increase in the antisymmetric part. An enormous change in the VCD is observed as a result of adding 0.1M NaCl. First of all, the carboxylate negative peak at ca. 1607cm^{-1} has decreased significantly. Second, the VCD couplet in the amide I' has disappeared entirely. Instead, a large negative VCD peak at ca 1654 cm^{-1} is observed. This negative peak, has also showed broadening with respect to the trialanine in D_2O and in 0.03 and 0.06M NaCl as well. Its broadened such that it covers the entire wavenumber range of the negative - positive couplet of the trialanine in D_2O.

Table VI - VIII summarizes the effect of the salt (low concentration and the high concentration) on the $(L\text{-}Ala)_3$ spectrum.

Reproduced with permission of the copyright owner. Further reproduction prohibited without permission.

Table VI. Observed VCD and Absorption Frequency and Intensity Parameters for $(L\text{-}Ala)_3$ in 0.03M salt at 25 °C

Mode	Infrared		VCD	
	Frequency	Intensity	Frequency	Intensity
	cm^{-1}	absorbance units	cm^{-1}	absorbance units
ν_{carbox}	1596	0.43	1599	-1.42×10^{-6}
	1652	0.36	1647	-1.29×10^{-6}
$\nu_{amide\ I}$			1673	0.0
	1671	0.31	1685	4.7×10^{-7}

Table VII. Observed VCD and Absorption Frequency and Intensity Parameters for $(L\text{-}Ala)_3$ in 0.06M salt at 25 °C

Mode	Infrared		VCD	
	Frequency	Intensity	Frequency	Intensity
	cm^{-1}	absorbance units	cm^{-1}	absorbance units
ν_{carbox}	1594	0.329	1598	-1.35×10^{-6}
	1652	0.26	1648	-1.13×10^{-6}
$\nu_{amide\ I}$			1669	0.0
	1671	0.22	1684	2.5×10^{-7}

Reproduced with permission of the copyright owner. Further reproduction prohibited without permission.

Table VIII. Observed VCD and Absorption Frequency and Intensity Parameters for $(L\text{-}Ala)_3$ in 0.1M salt at 25 °C

Mode	Infrared		VCD	
	Frequency	Intensity	Frequency	Intensity
	cm^{-1}	absorbance units	cm^{-1}	absorbance units
ν_{carbox}	1594	0.25	1607	-9.3×10^{-7}
$\nu_{amide\ I}$	1656	0.35	1654	-1.98×10^{-6}

Reproduced with permission of the copyright owner. Further reproduction prohibited without permission.

4.4-Discussion

4.4.1- $(Ala)_3$

The results presented above demonstrate that peptides as small as $(L\text{-}Ala)_3$ may exhibit a preferred solution conformation that is detectable on the VCD time scale. In the case of the trimer, the interactions stabilizing this solution structure can be lessened by a number of factors such that the VCD spectra are weakened or lost. It was shown previously that varying the pH to the limits at which zwitterions are no longer possible will cause the loss of VCD signals in the amide I region. Also it was shown that a dipeptide without charged end groups, such as acetyl-L-Ala-$N^{'}$-methyl-amide, does not show a bisignate VCD spectrum either [section 4.1.2, chapter 4].

In this study, we show that changes in temperature and ionic strength similarly change the stability of the interactions that give rise to a solution structure. Figure 4-6 demonstrates that at 10 °C, the amplitude of the VCD signal is nearly twice that at 25 or 60 °C. The loss of signal is understandable in terms of the wider

Reproduced with permission of the copyright owner. Further reproduction prohibited without permission.

distribution of conformers at elevated temperatures, and a general destabilization of the most predominant structures.

The results for the ionic strength shown above are illustrated in two parts: low concentration and the high concentration. The reason for that is that at lower concentration (0.03 - 0.06 M NaCl) there are no significant effects on the spectra, whereas the higher concentration (0.1M NaCl) showed significant changes in the results. This means that the distortion of the stable secondary structure of the trialanine in the vibrational time scale increases proportionally with the concentration of the salt.

At the lower concentration of the salt (0.03 and 0.06M) the effect is a small structural change of the trialanine similar to one observed for increased temperature. This could be deduced from the slight changes in the ratio of the antisymmetric to symmetric vibrations of the amide I', and the small shift of the zero-crossing of the amide I' negative-positive couplet in VCD spectrum. However the existence of the couplet indicates that at this level of the salt concentration there still are stable secondary structures for trialanine in aqueous solution at the vibrational time scale, and

Reproduced with permission of the copyright owner. Further reproduction prohibited without permission.

these concentrations, i.e., 0.03M and 0.06 M have not effected the zwitterionic interaction of the peptide. The stabilization of the peptide, in fact is somewhat increased as a result of adding 0.06M salt; this could be due to an increase of the ionic strength and a decrease of the dielectric constant of the solution as a result of adding the salt of concentration up to 0.06M.

The effect of the higher concentration, 0.1M NaCl, on the secondary structure of the trialanine in aqueous solution on the other hand, is more significant than the lower concentration of the salt. The C=O force constant has decreased due to attraction of Na^+ to the carbonyl oxygen; this is indicated by the shift of the amide I' absorption peak to the higher wavenumber.

Disappearance of the negative - positive couplet of the amide I' VCD band shows that increasing the concentration of the salt has effected the stability of the trialanine in aqueous solution. This is due to the distortion of the zwitterionic interaction which is the main factor for the existence of the trialanine stable structure in D_2O [18]. Adding high concentration of salt has increased the

Reproduced with permission of the copyright owner. Further reproduction prohibited without permission.

ionic strength of the solution [22]. The ionic strength μ is given by the expression:

$$\mu = 1/2\ \Sigma_i\ M_i\ Z_i^2 \qquad (4\text{-}7)$$

where M is the molarity and Z the charge of the ion. Increasing the ionic strength decreases the " sphere of influence" of each charged side on the peptide. Thus the higher the ionic strength, the smaller are the interactions between charged groups, namely - NH_3^+ and $-CO_2^-$, and distortion of the zwitterionic interaction and therefore, lack of the stable solution structure for the trialanine.

A decrease of the carboxylate peak with respect to the amide I' peak intensity is observed in 0.1M NaCl; this decrease could be due to the binding of the sodium ion at the oxygens of the $-CO_2^-$ group. This C=O group, however, can contribute to the amide I' absorption peak by increasing the intensity. This increase is similar to the increase of the intensity in going from trimer to tetremer which has three C=O groups, whereas the tetramer has two of them. This interpretation, however, need more experimental evidence in order to be supported.

Reproduced with permission of the copyright owner. Further reproduction prohibited without permission.

Overall, there is no stable structure for the $(L\text{-}Ala)_3$ in D_2O as a result of adding 0.1M NaCl, and we can conclude and support the idea of the existence of a stable structure for the trialanine in aqueous solution is due to the zwitterionic interaction.

4.4.2- $(L\text{-}Ala)_4$ and $(L\text{-}Ala)_5$

Both the VCD and the absorption spectra exhibit a distinct spectral change between the trimer and the tetramer. Whereas the trimer exhibits two partially resolved amide I' modes at 1652 and 1674 cm^{-1}, and a corresponding negative - positive, near conservative VCD couplet with a zero crossing at 1667 cm^{-1}, the tetramer and pentamer exhibit lower frequency amide I' absorption maxima (1648 cm^{-1}, and a negative/positive couplet of larger amplitude, with a zero crossing shifted toward lower wavenumber (1654 cm^{-1}). The shift, as well as changes in the $\Delta A/A$ ratio of the signals, indicate that there is a significant conformational change between the trimer and the larger analogues.

Reproduced with permission of the copyright owner. Further reproduction prohibited without permission.

4.4.2.1- Previous ROA Results of $(Ala)_n$ in aqueous solution.

Ford et.al., have suggested on the basis of their ROA data that the di- tri- tetra- and pentapeptides in neutral, acidic, and basic solutions all have similar backbone conformations. The same peptide $(L\text{-}Ala)_3$ which was proposed by Diem et.al., [18] to be stable in solution due to the zwitterionic interaction did not exhibit ROA data that support the conclusion from the VCD results, since the ROA results [19] in neutral H_2O and 1N NaOH basic solution similar. Based on these results they concluded that the backbone conformations are basically the same. The Raman spectrum of the trialanine in D_2O showed two bands at 1650 cm^{-1} and 1672 cm^{-1} corresponding to the couplet in VCD results which was observed by Lee et.al.

Two different conclusions concerning the solution conformation of Ala_3 were resulted by VCD and ROA. These two methods of observation of optical activity provide different information of molecular chirality, therefore, different conclusions were reached. However, Keiderling et.al., [20] explained this different

Reproduced with permission of the copyright owner. Further reproduction prohibited without permission.

sensitivity of VCD and ROA using two model compounds, (S) -1-amino-2-propanol and (S) -2- amino -1- propanol Figure 4-11.

Their work showed that the slight difference in the environment of the asymmetric center for these two components leads to their having quite distinct VCD and ROA spectra which in turn exemplify the basic physical differences in the two methods. The VCD and ir absorption spectra for these two compounds are shown in Figure 4-12. There is a surprising level of differences in the ir absorption spectra for these two isomeric compounds. The ir intensities of (1) are similar for most of the vibrational bands in this mid-ir region, whereas for (2), the intense band at ~1050 cm^{-1} (C-O stretching mode) dominates the ir spectrum. However, the ir spectra of the two compounds do show comparable " group frequencies " , for example, the NH_2 scissoring mode at ~ 1600 cm^{-1}, the asymmetric CH_3 deformation (mixed with O-H bending mode) at ~1450 cm^{-1}, the NH_2 wagging mode mixed with CH_2 rocking at ~840 cm^{-1}.

Reproduced with permission of the copyright owner. Further reproduction prohibited without permission.

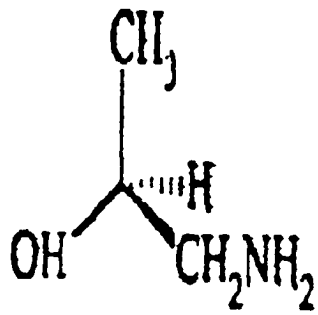

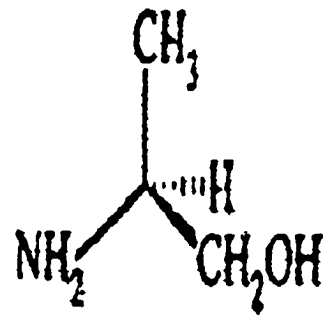

Figure 4-11: *(S) -1-amino-2-propanol and (S) -2- amino -1- propanol. Adapted from ref. [20]*

Reproduced with permission of the copyright owner. Further reproduction prohibited without permission.

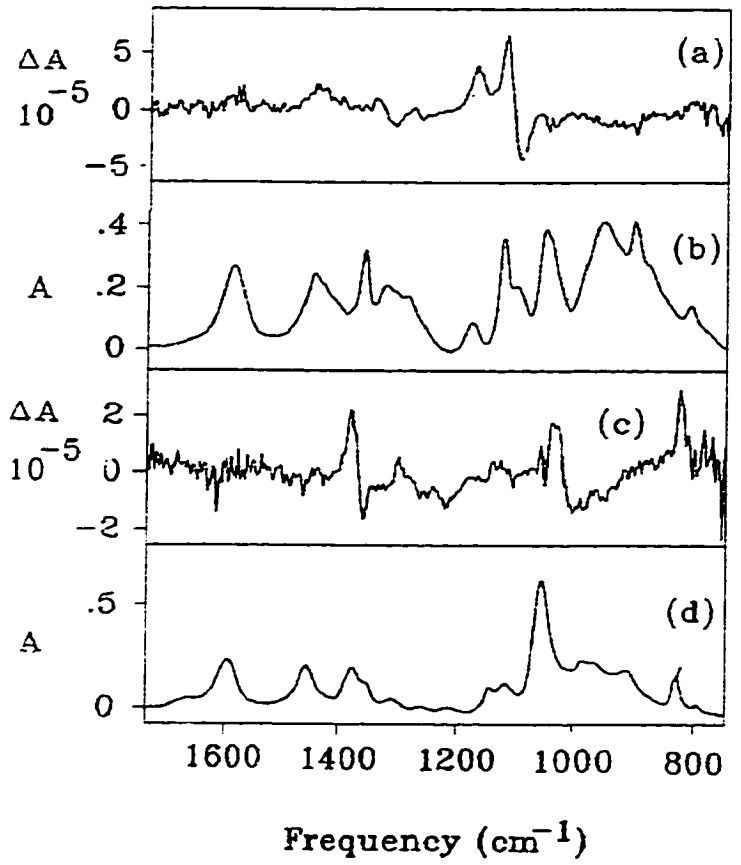

Figure 4-12: *The VCD and ir absorption spectra for (S) -1-amino-2-propanol and (S) -2-amino -1- propanol. Adapted from ref. [20]*

Reproduced with permission of the copyright owner. Further reproduction prohibited without permission.

The VCD spectra of the two aminopropanols are also very distinctive in terms of both sign patterns and VCD intensities. The overall VCD intensity for (1) is about 2 times stronger than for (2). As shown in Figure 4-12, the more intense VCD signals for the two aminopropanols come from quite different vibrational motions. The most intense VCD bands for neat (1) at ~1130 cm^{-1} can be assigned to a C-C stretching mode mixed with CH_2 twisting and C-N stretching. As for (2), the most intense VCD bands are found at ~ 1380 cm^{-1} , assigned to the symmetric CH_3 deformation mode mixed with the O-H bending mode.

This indicates that the dominant VCD arises from coupling of the transition dipoles and not from the local environments of the oscillators. Figure 4-13 shows the Raman and ROA spectra of the same compounds. In contrast, the Raman spectra, while still distinguishable, are much more similar as far as relative intensities are concerned. In both Raman spectra, the most intense Raman bands are those corresponding to NH_2 waggnig mode (mixed with CH_2 rocking) at ~ 840 $cm^{-1}$and the asymmetric methyl deformation (mixed with the O-H bending) at 1450 cm^{-1}.

Reproduced with permission of the copyright owner. Further reproduction prohibited without permission.

In the 1100 - 1400 cm^{-1} region, where the vibrational frequencies of the two compounds do differ, the overall patterns of Raman intensities still remain comparable. The ROA results for the two compounds, are also strikingly similar, with the exception of the C-C-C stretching modes.

The differences in VCD spectra and the similarities in ROA spectra for the two aminopropanols clearly show that VCD and ROA provide complementary information with respect to the molecular chirality.

If the arrangement of substitutents about the central carbon is altered, the VCD signals from O-H bending, CH_3 deformation, NH_2 scissoring motions and other motions change as well. By contrast, only the carbon framework modes (~1100 cm^{-1}) have a significant difference in ROA for (1) and (2), while for other vibrational motions the ROA spectra remain roughly the same. Therefore, the ROA signals seen for the O-H bending, CH_3 deformation and NH_2 wagging imply an independence from the detailed positioning of the -OH and -NH_2 groups on the carbon backbone. The ROA spectra can therefore be attributed to the

Reproduced with permission of the copyright owner. Further reproduction prohibited without permission.

local characteristics of each functional group; whereas VCD is sensitive of the overall change in molecular chirality. Coupling of different groups, through space, leads to the dominant VCD interaction. Consequently, VCD can, in some sense, be said to reflect primarily the conformation and ROA the configuration of the molecules. Due to the different information contents offered by VCD and ROA, they can be considered as complementary techniques in terms of their preferential sensitivities towards these different aspects of molecular chirality.

A similar conclusion was reached by Barron [21] in a study of the ROA of model DNA. Whereas the VCD polyneocleotides showed exquisite sensitivity towards the conformation, the ROA spectra couldn't distinguish uniquely even the B- and Z- form of DNA.

However, it now appears that there is sufficient evidence to postulate that there is a distinct solution conformation in $(L\text{-}Ala)_3$ at neutral pH, and that the larger homologues do exist in a different conformation. The failure to detect such conformational changes *via* ROA may result from the different molecular

Reproduced with permission of the copyright owner. Further reproduction prohibited without permission.

properties that are sampled by VCD and ROA. Literature evidence substantiates this latter claim: the ROA and VCD spectra of polynucleic acids in the (right-handed) B-form and the (left-handed) Z-form differ strongly in the VCD spectra in both the phosphate stretching region (950 - 1200 cm^{-1}) as well as the base breathing and carbonyl stretching vibrations [20]. In fact, the VCD spectra in these regions actually switch sign between the left-handed and the right-handed forms. However, the ROA spectra did not show such clear spectral variations; on the other hand, the Raman and ROA spectra appear to be more specific to distinguish different sequences of base pairs. Keiderling also reported the relationship between VCD and ROA spectra of

Reproduced with permission of the copyright owner. Further reproduction prohibited without permission.

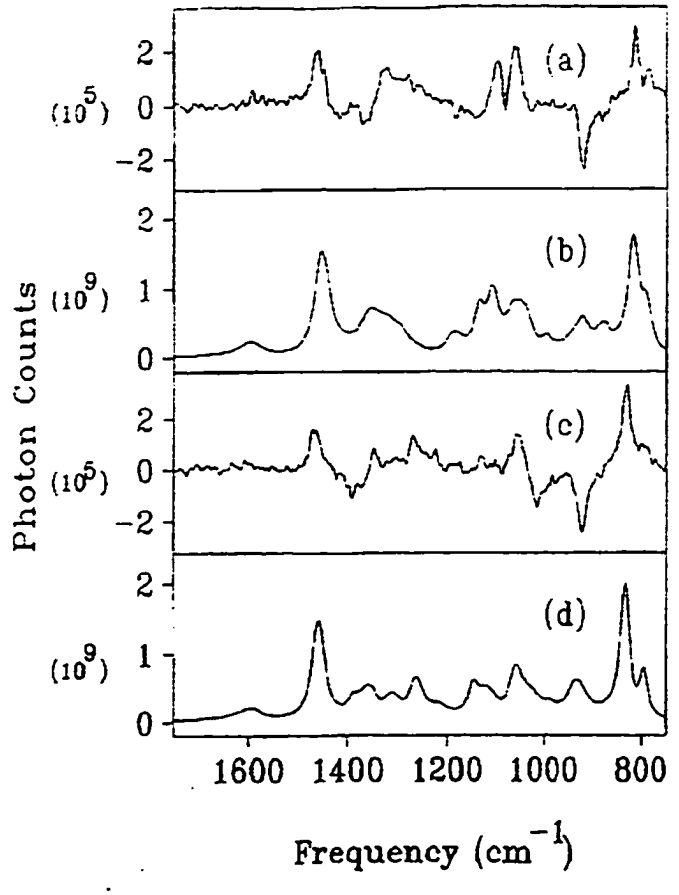

Figure 4-13: *The ROA and Raman spectra for(S) -1-amino-2-propanol and (S) -2-amino-1-propanol . adapted from ref. [20].*

Reproduced with permission of the copyright owner. Further reproduction prohibited without permission.

similar amino-propoanols [section 4.1.3, chapter-4] and found that the ROA is more sensitive to configurational changes in a molecule (such as moving an alcohol for an amine group) whereas VCD monitors the overall conformation of a molecule in a more sensitive way. In the past, the conformational sensitivity of VCD was modeled in terms of simple dipolar coupling models, although the limitations of such models are evident and have been pointed out in the literature [17].

Thus, we are confident that the spectral changes observed between the trimer on one hand, and the tetra- and pentameters on the other, are due to conformational changes that depend on the chain lengths of the peptides. This claim is further substantiated by the fact that early CD measurements on a series of protected $(Ala)_n$ with n=3 to 9, exhibited an easily recognizable signal at n=9 of a sheet structure; and that the shorter sequences, such as $(L\text{-}Ala)_4$, show weak signals that differ from those of the longer peptides.

Due to the lower solubility of the tetra- and pentamer, VCD studies as a function of the solvent ionic strength could not be

Reproduced with permission of the copyright owner. Further reproduction prohibited without permission.

carried out. At the peptide concentrations necessary for the observation of VCD, precipitation of the peptides occurred. The formation of a solid precipitate, in general, produces very large artifacts that are often bisignate and mimic VCD features, but are thought to arise from the Christianson effect.

4.4.3- (L-Ala)$_6$

Compared to the tetra- and pentamer, the hexamer shows significantly changed spectral patterns as well. The changes from the trimer to the tetra- and pentamer are similar in magnitude and direction than the changes from the tetra- and pentamer to the hexamer: the VCD spectra become narrower and more pronounced, and the zero-crossing is shifted toward lower wavenumber.

Upon heating, both the infrared absorption and the VCD spectra of the hexamer revert back to those of the pentamer at room temperature. Thus, it appears that the room temperature conformation of the hexamer is quite different from that of the pentamer, but that at elevated temperature, the conformation of the hexamer approaches that of the pentamer at room

Reproduced with permission of the copyright owner. Further reproduction prohibited without permission.

temperature. All conformations reported here exhibit negative-positive couplets (from lower to higher wavenumber). This sign pattern has previously been associated with poly-L-proline I and II secondary structures, and a left-handed extended helix. Based on simple exciton-type calculations, we find that extended (left-handed) helix ($\Phi = -110°$, $\Psi = 120°$) fits the observed data best for tetra-and pentamer, whereas the trimer was reproduced best by a structure with $\Phi = 120°$, $\Psi = -25°$. While the latter structure would require a very strong stabilizing interaction, it is clear that the larger homologues fall into the broad class of structures in the upper left corner of the Ramachandran plot, and may close to flat or slightly left-handed helical structures.

4.5- Conclusions

It appears from our data that VCD is, indeed, sensitive to slight structural changes in peptides brought on by changes in chain length, temperature and ionic strength variations. ROA, on the other hand, is not able to perceive the subtle conformational changes. Although the salt concentration dependence of the VCD spectra could not be extended to the longer chain peptides, it

Reproduced with permission of the copyright owner. Further reproduction prohibited without permission.

appears that secondary structures can be severely affected at 0.1 M NaCl concentration. Increased temperature has, generally, a smaller effect, with slight loss of VCD intensity - and solution structure - at elevated temperatures. An exception to this observation was the hexamer $(L\text{-}Ala)_6$, for which distinct melting was observed.

Reproduced with permission of the copyright owner. Further reproduction prohibited without permission.

References:

1- H. J. Dyson & P. E. Wright (1991) " *Defining solution conformation of small linear peptides*", Ann. Rev. Biophys. Biophys. Chem., 20, 519.

S. C. Yasui & T. A. Keiderling (1986) *J. Am. Chem. Soc.* 108, 5576.

2- G. M. Roberts, O. Lee, J. Calienni & Diem, M. (1988) *J. Am. Chem. Soc.* 110, 1749.

O. Lee (1992), Ph.D. theses, CUNY.

3- G. M. Paterlini, T. B. Freedman & L. Nafie (1986) *Biopolymers* 25, 1751.

4- S. C. Yasui & T. A. Keiderling (1986) *Biopolymers* 25, 5.

5- S. C. Yasui & T. A. Keiderling, G. M. Bonora & C. Toniolo (1986) *Biopolymers* 25, 79.

6- S. C. Yasui & T. A. Keiderling, F. Formaggio, G. M. Bonora & C. Toniolo (1986) *J. Am. Chem. Soc.* 108, 4988.

7- S. C. Yasui, & T. A. Keiderling & R. Katakai (1987) *Biopolymers*, 26,1407.

Reproduced with permission of the copyright owner. Further reproduction prohibited without permission.

8- S. C. Yasui & T. A. Keiderling & M. Sisido (1987) *Macromolecules* 20, 2403.

9- G. Holzwarth & I. Chabay (1972) *J. Chem. Phys.* 49, 1632.

10- C. W. Deutsche & A. Moscowitz (1968) *J. Chem. Phys.* 49, 3257.

11- C. W. Deutsche & A. Moscowitz (1970) *J. Chem. Phys.* 53, 2630.

12- L. D. Barron (1978) *in Advances in Infrared Raman Spectroscopy*, Vol. 4, R. J. H. Clark & R. E. Hester, Eds., Heyden, London, p. 271.

13- J. Snir, R. A. Frankel & J. A. Schellman (1975) *Biopolymers* 1, 173.

14- I. Tinoco (1963) *Radiation Res.* 20, 133.

15- W. Kauzmann (1957) *Quantum Chemistry: An Introduction*, *Academic Press*, New York, Vol. 19.

16- T. R. Faulkner (1976) Ph.D. thesis, University of Minnesota. I.Tinoco (1963) *Radiation Research*, 20, 133.

17- O. Lee, G. M. Roberts, and M. Diem, (1989) *Biopolymers*, 28, 1759.

Reproduced with permission of the copyright owner. Further reproduction prohibited without permission.

18- J. Ford, Z. Q. Wen, L. Hecht, and L. D. Barron, (1994) *Biopolymers*, 34, 303.

19- C. N. Tam, P. Bour and T. A. Keiderling, (1996) *J. Am. Chem. Soc.*, 110, 2070.

20- A. F. Bell, L. Hecht and L. D. Barron, (1997), *J. Am. Chem. Soc.*, 140, 3780.

21- G. Zubay (1988), Biochemistry, 101-102, Macmillan, New York.

Reproduced with permission of the copyright owner. Further reproduction prohibited without permission.

Appendix I

A1- Alignment procedure

To align the optics for the VCD instrument, we need to use He-Ne laser. Before everything we need to make sure that the laser beam is parallel. This is done as followes: Mount a rail rod on an optical bench, then mount the laser on the rail. Mount a pinhole close to the laser, it has to be exactly at the same line with the laser beam, make sure that the laser beam goes through the pinhole. After that, move the pinhole far away from the laser, and make the laser beam goes through the pinhole again. Move the pinhole back and forth on the rail rod and make sure that the laser beam goes through the pinhole at each point.

After obtaining a parallel laser beam, take it very carefully to align the VCD (VC1, VC2, or VC3) instrument.

Here, we use VC1 as an example to demonstrate the alignment technique; the VC2 and VC3 will be aligned using similar procedure.

Reproduced with permission of the copyright owner. Further reproduction prohibited without permission.

A.1.1- Backward alignment

Take the detector out and replace it with the laser. Make the beam hitting on the center of the lens (L) (see Figure A-1) and goes through and hits the center of the mirror (M_1). Align this mirror so that it hits the flat mirror (M_2), which is at 45^0 from the mirror (M_1). The beam reflects from M_2 and comes parallel in to the exit slit of the monochromator; it has to hit the center of the slit. (if the height is not appropriate, adjust it by adjusting the laser height without changing the angle of the beam). The beam has to come parallel out of the entrance slit of the monochromator. In this stage, if the beam is not parallel, we should not try to move the laser, instead adjust with the two mirrors until the beam comes out of the monochrometer parallel. This parallel beam, which comes out of the monochrometer has to hit the center of the mirror (M_3). To be sure whether the beam hits the center of the mirror or not, measure the diameter of the mirror; cut a piece of a paper and make a mark from the edge of the paper to a point at the half diameter of the mirror. Take this paper and hold it so that its edge comes to the edge of the mirror. Make the light beam hits the mark on the paper. The beam has to reflect 45^o and hits the

Reproduced with permission of the copyright owner. Further reproduction prohibited without permission.

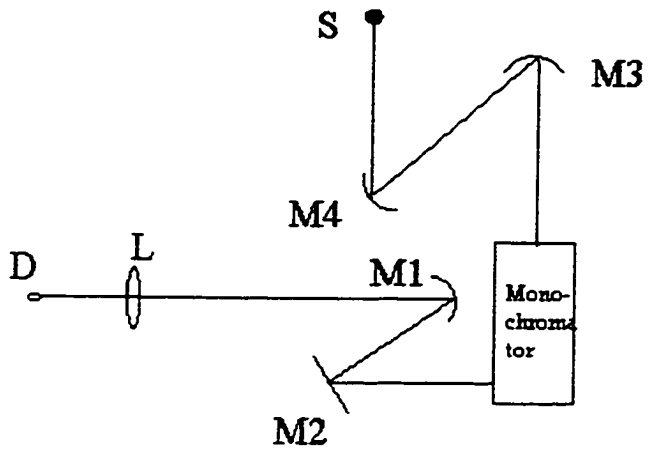

Figure A-1: Optical layout for the VCI.

A.1.2- Front alignment

In this case we take the source (S) out and replace it with the laser. The procedure for the front alignment is same as the background alignment. The laser has to hit the center of the mirror (M4) and reflects at 45° and hits the other mirror (M3), from which it reflects parallel to the center of the entrance slit, and comes out of the center of the exit slit and hits the flat mirror (M2) where reflects at 45° angle and hits M1 from which it reflects parallel through the center of the wire grid polarizer, PEM (see the alignment of the PEM) and the

Reproduced with permission of the copyright owner. Further reproduction prohibited without permission.

sample cell to the center of the lens (L) and parallel to the detector (D).

A.1.3- Alignment of the photoelastic modulator

One of the most important aspects of the VCD instrumentation is the proper alignment of the photoelastic modulator (PEM). Any misalignment of the PEM will produce enormous artifact. Therefore one has to carefully align the PEM in order to obtain good results. The procedure for the alignment of the PEM is basically same as any other alignment of the instrument. The He-Ne laser is used; the laser will be mounted such that the light hits the center of the PEM crystal (ZnSe) and the reflected light has to hit back to the laser in order to obtain a good alignment for the PEM.

Reproduced with permission of the copyright owner. Further reproduction prohibited without permission.

Bibliography

Chapter 1

1. P. R. Griffiths and J. A. de Haseth (1986) " *Fourier transform infrared spectroscopy*", John Wiley & Sons Inc., New York.

2. J. Chamberlain (1979), *"The Principles of interferometric spectroscopy"*, John Wiley & Sons Inc., New York.

3. Erwin Kreyszing (1967) *"Advanced Engineering mathematics"* John Wiley & Sons, Inc., New York.

4. C. Ray Wylie, L. C. Barrett (1995) " *Advanced Engineering Mathematics*", McGraw-Hill, Inc., New York.

5. R.W. Ditchburn (1961), *Light*, Dover publications, Inc., New York

6. M. J. Smith, C. J. Manning, R. A. Palmer and J. L. Chao (1988), *Appl. Spectrosc.* 42, 546.

7. R. A. Palmer (1993) *Spectroscopy*, 8, 26.

8. M. L. Meade (1983) " *Lock-in amplifiers: Principles and applications*" Short Run Press Ltd., Exeter, London.

Reproduced with permission of the copyright owner. Further reproduction prohibited without permission.

Chapter 2

1- W. Cooper (1981), " *Introduction to Pascal for Scientists*", JOHN WILEY & SONS, New York.

2- E. O. Brigham (1988) "*The fast Fourier transform and its applications*" , Prentice Hall, Englewood Cliffs, New Jersey.

3- N. Morrison (1994) " *Introduction to Fourier analysis*" JOHN WILEY & SONS, New York

4- J. W. Cooley, P. A. Lewis and P. D. Welch (1967) "*IEEE transactions on Audio and electroacoustics*" Au-15(2), 79.

5- P. C. Kelly and G. Horlick (1973) , *Analytical Chemistry*, 45(3), 518.

6- G. Horlick (1972), *Analytical Chemistry*, 44(6), 943.

7- P. R. Griffiths and J. A. de Haseth (1986) " *Fourier transform infrared spectroscopy*", JOHN WILEY & SONS, New York.

8- L. Glasser (1987), *J. of chem. Education*, 64(12), A306.

9- D. Morgan (1994), *Practical DSP modeling, techniques, and programming in C*", JOHN WILEY & SONS, New York.

Reproduced with permission of the copyright owner. Further reproduction prohibited without permission.

10- C. Ray Wylie, L. C. Barrett (1995) " *Advanced Engineering Mathematics* ", McGraw-Hill, Inc., New York.

11- J. K. Kauppinen, D. J. Moffatt (1981), *Appl. Spectrosc.*

12- P. R. Griffiths (1975), *Appl. Spectrosc.*, 29, 11.

13- J. Chamberlain (1979), " *The Principles of interferometric spectroscopy* ", JOHN WILEY & SONS , New York.

14- A. C. McCoy and J. A. de Haseth (1988), *Applied Spectrosc.*, 42, 336.

15- L. A. Nafie (1988), " *Polarization modulation FTIR spectroscopy* " , JOHN WILEY & SONS , New York.

Chapter 3

1- L. A. Nafie, L. C. Cheng and P. J. Stephens (1975) *J. Amer. Chem. Soc.* , 97, 3842.

2- G. Holzwarth, E. C. Hsu, H. S. Mosher, T.R. Faulkner and A. Moscowitz (1974) *J. Amer. Chem. Soc.*, 96, 251.

3- N. J. Greenfield and G.D. Fasman (1969) *Biochemistry*, 8, 4108.

4- F. M. Pohl and T.M. Jovin (1972) *J. Mol. Biol.*, 67, 375.

Reproduced with permission of the copyright owner. Further reproduction prohibited without permission.

5- T. A. keiderling (1990), *"Practical Fourier transform infrared spectroscopy: Industrial and laboratory chemical analysis"*, J. R. Ferraro, & K. Krishnan, Eds., Academic Press, NY, pp. 203-284.

6- M. Diem, G. M. Roberts, O. Lee and A. Barlow (1988) *Appl. Spectrosc.*, 42,

7- L. A. Nafie, M. Diem and D.W. Vidrine (1979) *J. Amer. Chem. Soc.*, 101, 496.

8- P. R. Griffiths and J. A. de Haseth (1986) *" Fourier transform infrared spectroscopy"*, JOHN WILEY & SONS.

9- P. Malon and T. A. Keiderling (1988) *Appl. Spectrosc.*, 42, 32.

10- O. Lee (1992), Ph.D. theses, CUNY.

11- E. D. Lipp and L. A. Nafie (1984) *Appl. Spectrosc.*, 38, 20.

12- N. Ragunathan, N. S. Lee, T. B. Freedman, L. A. Nafie, C. Tripp, and H. Buijs (1990) *Appl. Spectrosc.*, 44, 5.

13- P. L. Polavarapu, (1985), *" Fourier transform Infrared vibrational circular dichroism"*, Academic press, New York.

Reproduced with permission of the copyright owner. Further reproduction prohibited without permission.

14- C. Marcott, A. E. Dorey, and I. Noda (1993) *Appl. Spectrosc.*, 47, 1324.

15- B. Wang and T. A. Keiderling (1995) *Appl. Spectrosc.*, 49, 1347.

16- C. J. Manning and R. A. Palmer (1991) *Rev. Sci. instrum.* 62(5), 1219.

17- J. Connes and P. Connes (1966) *J. Opt. Soc. Am.*, 56, 896.

18- L. A. Nafie and M. Diem (1979) *Appl. Spectrosc.*, 33.130.

19- C. Wylie, L. C. Barrett (1995) " *Advanced Engineering Mathematics*", McGraw-Hill, Inc., New York.

Chapter 4

1- H. J. Dyson & P. E. Wright (1991) " *Defining solution conformation of small linear peptides*", Ann. Rev. Biophys. Biophys. Chem., 20, 519.

S. C. Yasui & T. A. Keiderling (1986) *J. Am. Chem. Soc.* 108, 5576.

2- G. M. Roberts, O. Lee, J. Calienni & Diem, M. (1988) *J. Am. Chem. Soc.* 110, 1749.

Reproduced with permission of the copyright owner. Further reproduction prohibited without permission.

O. Lee (1992), Ph.D. theses, CUNY.

3- G. M. Paterlini, T. B. Freedman & L. Nafie (1986) *Biopolymers* 25, 1751.

4- S. C. Yasui & T. A. Keiderling (1986) *Biopolymers* 25, 5.

5- S. C. Yasui & T. A. Keiderling, G. M. Bonora & C. Toniolo (1986) *Biopolymers* 25, 79.

6- S. C. Yasui & T. A. Keiderling, F. Formaggio, G. M. Bonora & C. Toniolo (1986) *J. Am. Chem. Soc.* 108, 4988.

7- S. C. Yasui, & T. A. Keiderling & R. Katakai (1987) *Biopolymers*, 26,1407.

8- S. C. Yasui & T. A. Keiderling & M. Sisido (1987) *Macromolecules* 20, 2403.

9- G. Holzwarth & I. Chabay (1972) *J. Chem. Phys.* 49, 1632.

10- C. W. Deutsche & A. Moscowitz (1968) *J. Chem. Phys.* 49, 3257.

11- C. W. Deutsche & A. Moscowitz (1970) *J. Chem. Phys.* 53, 2630.

Reproduced with permission of the copyright owner. Further reproduction prohibited without permission.

12- L. D. Barron (1978) *in Advances in Infrared Raman Spectroscopy*, Vol. 4, R. J. H. Clark & R. E. Hester, Eds., Heyden, London, p. 271.

13- J. Snir, R. A. Frankel & J. A. Schellman (1975) *Biopolymers* 1, 173.

14- I. Tinoco (1963) *Radiation Res.* 20, 133.

15- W. Kauzmann (1957) *Quantum Chemistry: An Introduction*, *Academic Press*, New York, Vol. 19.

16- T. R. Faulkner (1976) Ph.D. thesis, University of Minnesota. I.Tinoco (1963) *Radiation Research*, 20, 133.

17- O. Lee, G. M. Roberts, and M. Diem, (1989) *Biopolymers*, 28, 1759.

18- J. Ford, Z. Q. Wen, L. Hecht, and L. D. Barron, (1994) *Biopolymers*, 34, 303.

19- C. N. Tam, P. Bour and T. A. Keiderling, (1996) *J. Am. Chem. Soc.*, 110, 2070.

20- A. F. Bell, L. Hecht and L. D. Barron, (1997), *J. Am. Chem. Soc.*, 140, 3780.

Reproduced with permission of the copyright owner. Further reproduction prohibited without permission.

21- G. Zubay (1988), Biochemistry, 101-102, Macmillan, New York.

Reproduced with permission of the copyright owner. Further reproduction prohibited without permission.

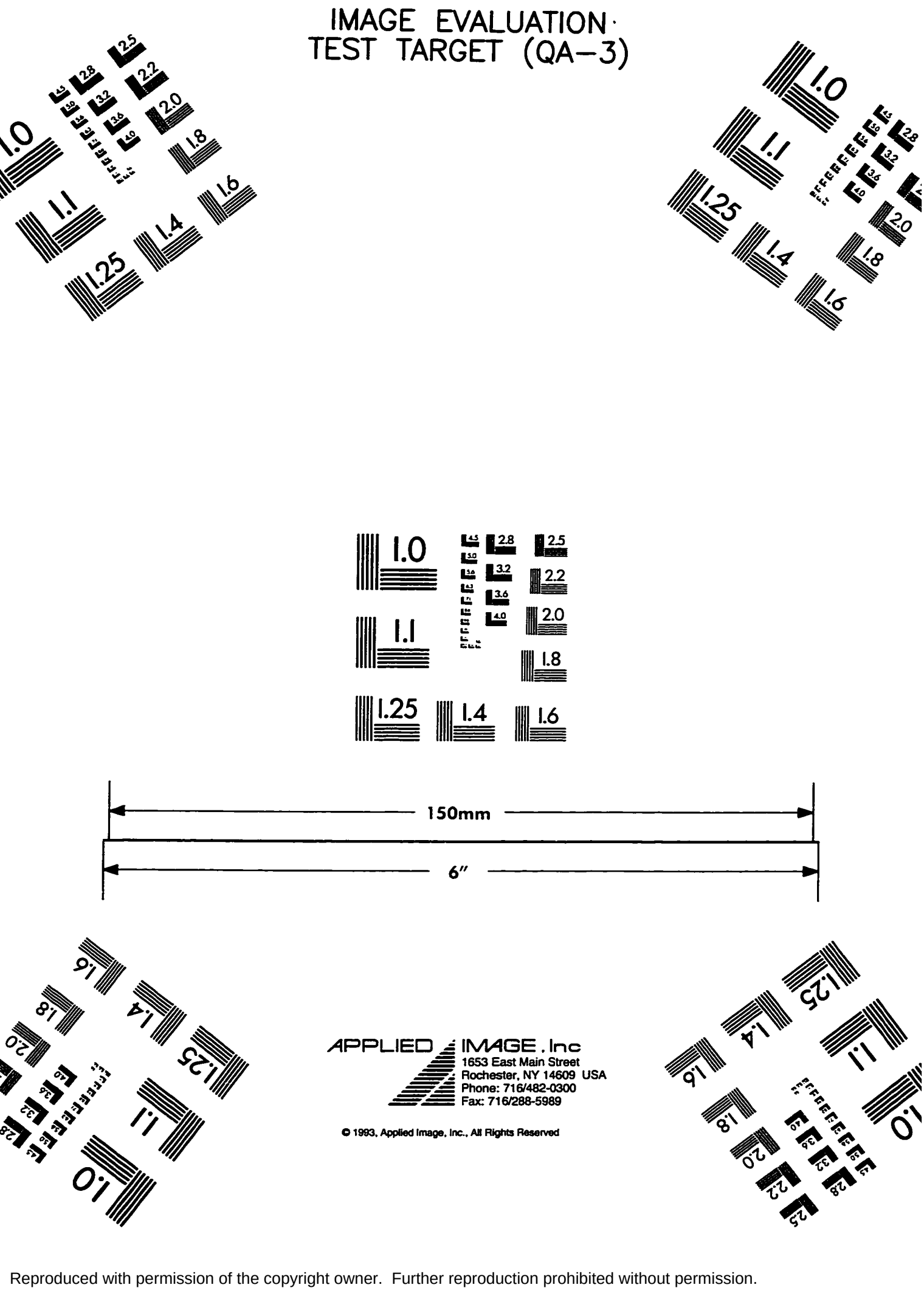

Reproduced with permission of the copyright owner. Further reproduction prohibited without permission.